THE UNIVERSITY OF QUEENSLAND

AUSTRALIA

Direct Numerical Simulation of Coupled Fluid-Particle Flow in Hydraulic Fractures

Duo Wang

B. Eng. (Civil Engineering)

M. Sc. (Civil Engineering)

A thesis submitted for the degree of Doctor of Philosophy at

The University of Queensland in 2018

School of Mechanical and Mining Engineering

Abstract

In this thesis, proppant transport and the conductivity of proppant-packed hydraulic fractures are studied via the implementation of a numerical approach which couples the lattice Boltzmann method (LBM) to the discrete element method (DEM).

Recent growth in the production of oil and gas from shales, and to lesser extent gas from coal seams, can be attributed to the successful application of hydraulic fracturing. However, contemporary numerical models of fluid injection and proppant transport are based on empirical approximations of the suspension as a continuous medium and, in some cases, experimental data. Assumptions related to Stokes drag on particles and a lumped suspension viscosity are not valid under practical conditions, while experiments provide limited information that can be used in predictions. To provide reliable predictions and further improve operation efficiency, an accurate modelling approach has become increasingly important.

In this research, a particle-scale computational model is implemented to provide fundamental new insights on proppant injection by exploring the relationship between fluid and proppant properties, fracture network geometries, and evolving deformable fracture boundaries. This represents a direct numerical simulation (DNS) approach for problems at the small to intermediate scale. In the developed model, a two-relaxation-time (TRT) collision operator is applied to improve the accuracy and stability of the LBM modelling. The particulate proppant phase is modelled by the DEM. For the two-phase fluid-particle system, the LBM and DEM are coupled via an improved partially saturated method (PSM) to provide two-way hydrodynamic coupling.

This project starts with the testing and improvement of the coupled LBM-DEM framework. Validations are presented through a range of flow configurations, including sphere packs, duct flows, and settling spheres, with good accuracy and convergence observed. Results also show that the improved model exhibits reasonable viscosity-independence, which has been reported to be one of the main concerns of many LBM applications. In the case of fluid flow past a single sphere, the fluctuation of error in drag coefficient can be restricted within 1 % when changing the LBM relaxation parameter, τ, from 0.53 to 1.0. This feature of the improved LBM-DEM framework allows for more flexibility in choosing the simulation parameters, which simultaneously improves the applicability of the numerical approach.

The developed model is then applied to aspects of hydraulic fracturing modelling, focusing on the numerical rheometry of dense particle suspensions, which is often characterised by semi-empirical models. In this project, the developed model aims at capturing the shear-dependent behaviour of the suspensions by computing the effective suspension viscosity and the hydrodynamic and mechanical reactions from the suspensions. The results are validated and compared to the semi-empirical expressions for the effective viscosity observed in particle suspensions. This study also demonstrates the impact of solid volume fraction on shear-dependent behaviour of the suspensions.

To provide practical predictions to the industry, the influence of proppant embedment on fracture conductivity is then investigated. The investigation starts with the replication of a numerical model in

which the Hertz elastic contact theory is applied to characterise the interaction between the fracture surface and proppant. A fracture permeability diameter is generated to find the optimal proppant concentration under various confining stresses, at which the maximum fracture permeability can be reached. In order to ensure the accuracy and veracity of the research, an elastoplastic model is developed, in which the finite element modelling is utilised to generated the fracture geometry after proppant embedment. The resultant fracture permeability diagram is then used to predict the well production using a set of theoretical solutions, highlighting the significant impact of proppant injection during hydraulic fracturing.

This project demonstrates the potential of the improved LBM-DEM model in providing fundamental new insights on the shear-dependent behaviour of suspensions and enhancement of well productivity by proppant injection. As potential extensions to the current model, future developments including non-Newtonian fluids, upscaling modelling, and random proppant distribution across the fracture surface are expected.

Declaration by author

This thesis is composed of my original work, and contains no material previously published or written by another person except where due reference has been made in the text. I have clearly stated the contribution by others to jointly-authored works that I have included in my thesis.

I have clearly stated the contribution of others to my thesis as a whole, including statistical assistance, survey design, data analysis, significant technical procedures, professional editorial advice, financial support and any other original research work used or reported in my thesis. The content of my thesis is the result of work I have carried out since the commencement of my higher degree by research candidature and does not include a substantial part of work that has been submitted to qualify for the award of any other degree or diploma in any university or other tertiary institution. I have clearly stated which parts of my thesis, if any, have been submitted to qualify for another award.

I acknowledge that an electronic copy of my thesis must be lodged with the University Library and, subject to the policy and procedures of The University of Queensland, the thesis be made available for research and study in accordance with the Copyright Act 1968 unless a period of embargo has been approved by the Dean of the Graduate School.

I acknowledge that copyright of all material contained in my thesis resides with the copyright holder(s) of that material. Where appropriate I have obtained copyright permission from the copyright holder to reproduce material in this thesis and have sought permission from co-authors for any jointly authored works included in the thesis.

Publications included in this thesis

1. [1] **D. Wang**, C. R. Leonardi, and S. M. Aminossadati, Improved coupling of time integration and hydrodynamic interaction in particle suspensions using the lattice Boltzmann and discrete element methods, *Computers & Mathematics with Applications*, 75, 7, 2018.

Other publications during candidature

Conference abstracts and presentations

1. **D. Wang**, C. R. Leonardi, and S. M. Aminossadati, Towards direct numerical simulation of proppant transport in coal seam gas reservoirs, *The 2nd Australasian Conference on Computational Mechanics*, Brisbane, Australia, 30 November-1 December, 2015.

2. **D. Wang**, C. R. Leonardi, and S. M. Aminossadati, Characterisation of proppant transport in hydraulic fractures using the coupled lattice Boltzmann method and discrete element method, *Thirteenth International Conference for Mesoscopic Methods in Engineering and Science*, Hamburg, Germany, 18-22 July, 2016.

3. **D. Wang**, C. R. Leonardi, and S. M. Aminossadati, An improvement on the coupling of particle suspensions using the coupled lattice Boltzmann and discrete element methods with immersed moving boundaries, *V International Conference on Particle-Based Methods*, Hannover, Germany, 26-28 September, 2017.

Conference publications

1. [2] C. R. Leonardi, W. Regulski, J. W. S. McCullough, **D. Wang**, T. R.Mitchell, B. D. Jones, and J. R. Williams, Characterising the behaviour of hydraulic fracturing fluids via direct numerical simulation, *SPE Asia Pacific Oil & Gas Conference and Exhibition, Society of Petroleum Engineers*, Perth, Australia, 25-27 October, 2016.

2. C. R. Leonardi, J. W. S. McCullough, **D. Wang**, and S. M. Aminossadati, Evaluation of the temperature-dependent rheology of non-Brownian particle suspensions via direct numerical simulation, *21st Australasian Fluid Mechanics Conference*, Adelaide, Australia, 10-13 December, 2018.

3. Z. You, **D. Wang**, C. R. Leonardi, R. Johnson Jr. and P. Bedrikovetsky, Influence of Elastoplastic Embedment on CSG Production Enhancement Using Graded Particle Injection, *APPEA 2019 Conference and Exhibition*, Brisbane, Australia, 27-30 May, 2019.

Contributions by others to the thesis

- Dr Christopher Leonardi - Initial conception of research, refinement of project design, revision of written content in capacity as the Principal Advisor.
- A/prof Saiied Aminossadati - Revision of written content in capacity as the Associate Advisor.
- The MIT Geonumerics Group - Developing the original research code, the GeonumericsEngine. This was further developed and utilised in the work presented in Chapters 3 and 4.
- Dr Bruce Jones - The conception and design, and interpretation of the BGK results of particle suspensions modelling, which are presented in Chapter 4.
- Dr Lukasz Llaniewski - Developing the open-source research code, the TCLB. This was further developed and utilised in the work presented in Chapters 5.

Statement of parts of the thesis submitted to qualify for the award of another degree

No works submitted towards another degree have been included in this thesis.

Research involving human or animal subjects

No animal or human subjects were involved in this research.

Acknowledgments

First of all, I would like to appreciate the generous guidance, great patience, and sincere friendship from my principle supervisor Dr. Christopher Leonardi throughout the research. You have really set up an example of what a research people should be like to me with your actions and words. I would also like to acknowledge my associated supervisors Dr Saiied Aminossadati for his support and attention that he have dedicated to me. I also deeply appreciate the friendship among my officemates, particularly Mr Jon McCullough and Mr Travis Mitchell for their selfless help to my research. From institutions around the world I would also like to acknowledge the Geonumeric Group from Massachusetts Institute of Technology and Dr Lukasz Laniewski from Warsaw University of Technology for their contributions to the development of the research codes, the GeonumericsEngine and TCLB, respectively. These codes were further developed and utilised in the work presented in this thesis. I am also grateful to Dr Phillip Seil, Prof Li-Shi Luo and Dr David Noble for answering my many questions.

My PhD program is funded by the School of Mechanical and Mining Engineering. Thanks to the financial support, I could live a happy life in Brisbane and put my heart and soul into my research.

Last but certainly not least, you will never walk alone. There are so many people I want to thank for their support and company. Mum and Dad, thank you for your unconditional support and comprehension to let me live my own life. Many thanks to all my adorable colleagues, i.e. Mr Tianhang Bai, Mr Chunshan Zheng and Mr Ben Yang. There is one more person I must not forget. Prof Yuntian Feng, I would not be who I am today without your supervision. Thank you for bringing me the opportunity to pursue further study and being my referee.

Financial support

This research was supported by The University of Queensland International Scholarship (UQI) and the Research Higher Degree Living Allowance Scholarship from School of mechanical and Mining Engineering.

Keywords

hydraulic fracturing, proppant transport, particle suspensions, proppant embedment, direct numerical simulation, lattice Boltzmann Method, discrete element method, partially saturated cell method

Australian and New Zealand Standard Research Classifications (ANZSRC)

ANZSRC code: 091307, Numerical Modelling and Mechanical Characterisation, 40%
ANZSRC code: 091405, Mining Engineering, 10%
ANZSRC code: 091406, Petroleum and Reservoir Engineering, 40%
ANZSRC code: 010302, Numerical Solution of Differential and Integral Equations, 10%

Fields of Research (FoR) Classification

FoR code: 0913, Mechanical Engineering, 40%
FoR code: 0914, Resources Engineering and Extractive Metallurgy, 50%
FoR code: 0103, Numerical and Computational Mathematics, 10%

Contents

List Of Figures

List Of Tables

List Of Abbreviations and Symbols

Abbreviations	
BGK	Bhatnagar-Gross-Krook
CFD	Computational Fluid Dynamics
CFL	Courant-Friedrichs-Levy
CSG	Coal Seam Gas
DEM	Discrete Element Method
DNS	Direct Numerical Simulation
FEM	Finite Element Method
IBM	Immersed Boundary Method
LBE	Lattice Boltzmann Equation
LBM	Lattice Boltzmann Method
LGA	Lattice Gas Automata
MEM	Momentum Exchange Method
MRT	Multiple-Relaxation-Time
PSM	Partially Saturated Method
SD	Stokesian Dynamics
SPH	Smoothed Particle Hydrodynamics
TRT	Two-Relaxation-Time

Symbols	
b	summation index of the modified solid weighting function
c	lattice speed
c_f	fracture compressibility
c_s	lattice speed of sound
E	Young's modulus
$\mathbf{e_i}$	particle distribution function velocities
F	suspension friction coefficient
F^{hydro}	hydrodynamic contribution to suspension friction coefficient
F^{mech}	mechanical contribution to suspension friction coefficient
f_i	density distribution functions

f_i^{eq}	equilibrium density distribution functions
f_i^{+}	post-collision density distribution functions
$\mathbf{G}$	body force
I	suspension viscous number
K_f	fracture permeability
k_n	discrete element normal contact stiffness
$\mathbf{M}$	MRT transformation matrix
$\mathbf{S}$	MRT diagonal collision matrix
p	fluid pressure
p_{in}	proppant injection pressure
p_{fr}	reservoir pressure
PI	well productivity index
r_e	radius of drainage area
r_{st}	radius of stimulated area
$\mathbf{u}$	fuid velocity
$\mathbf{x}$	lattice coordinates
β	PSN solid weighting funciton
Δt	time step
Δx	lattice spacing
δ	discrete element contact overlap
γ	lattice cell solid coverage ratio
λ_e, λ_e	TRT even and odd relaxation rates
Λ	TRT magic parameter
μ	dynamic viscosity
ν	kinetic viscosity
ρ	fluid density
ρ_p	normalised particle concentration
τ	LBM relaxation parameter
σ_d	dimensionless remote confining stress
ϕ	solid volume fraction
Ω_i	LBM collision operator
Ω_i^m	PSM collision operator

Chapter 1

Introduction

Since its emergence in the 1940's, hydraulic fracturing has become one of the most popular and successful techniques for the stimulation of unconventional gas reservoirs. The hydraulic fracturing process is recognised as a multi-phase, multi-scale, and multi-physics industrial problem and reliable prediction of the efficacy of a fracturing treatment is difficult. The influence of several factors including the properties of the injected fluid and proppant, the effect of branching fractures and proppant-fracture interaction are still not fully understood. Due to the complexity of underground formations, it is difficult to fully capture all the mechanisms of proppant injection in fracture networks with experiments. Consequently, an effective and accurate numerical approach has become increasingly important to the unconventional oil and gas industry for the purpose of understanding and predicting the hydraulic fracturing process. However, many of the current conventional fluid dynamics (CFD) models are based on coarse assumptions and empirical approximations, including treating the particle suspension as a continuous medium. In light of these shortcomings, the lattice Boltzmann method (LBM) and the discrete element method (DEM), which have displayed tremendous potential in the detailed characterisation of fluid and proppant flow in fractures, are applied to this work. By coupling the LBM to the DEM through an improved partially saturated method (PSM), the direct numerical simulation (DNS) of small to intermediate scale fracture flow scenarios can be undertaken.

1.1 Hydraulic Fracturing

The first hydraulic fracturing (commonly referred to as *fracking* treatment is recognised to have been performed on a gas well in the United States in 1947. Since then, hydraulic fracturing has become a common treatment to stimulate oil and gas reservoirs. As shown in Fig. 1.1, a complete hydraulic fracturing operation involves the high-pressure injection of an engineered particle suspension, comprised of the base fluid and high-strength particles referred to as proppant, into a wellbore. This induces artificial fractures in the reservoir in the vicinity of the well to help improve the formation permeability. After the fractures are formed, the base fluid is removed and the proppant remains in the fractures to keep the aperture open, thus improving gas productivity. In addition, development of hydraulic fracturing has resulted in improved interactions between natural and induced fractures such as those found in coal seams in order to improve the overall productivity.

The design of the suspending fluid is one of the most significant components in a hydraulic fracturing

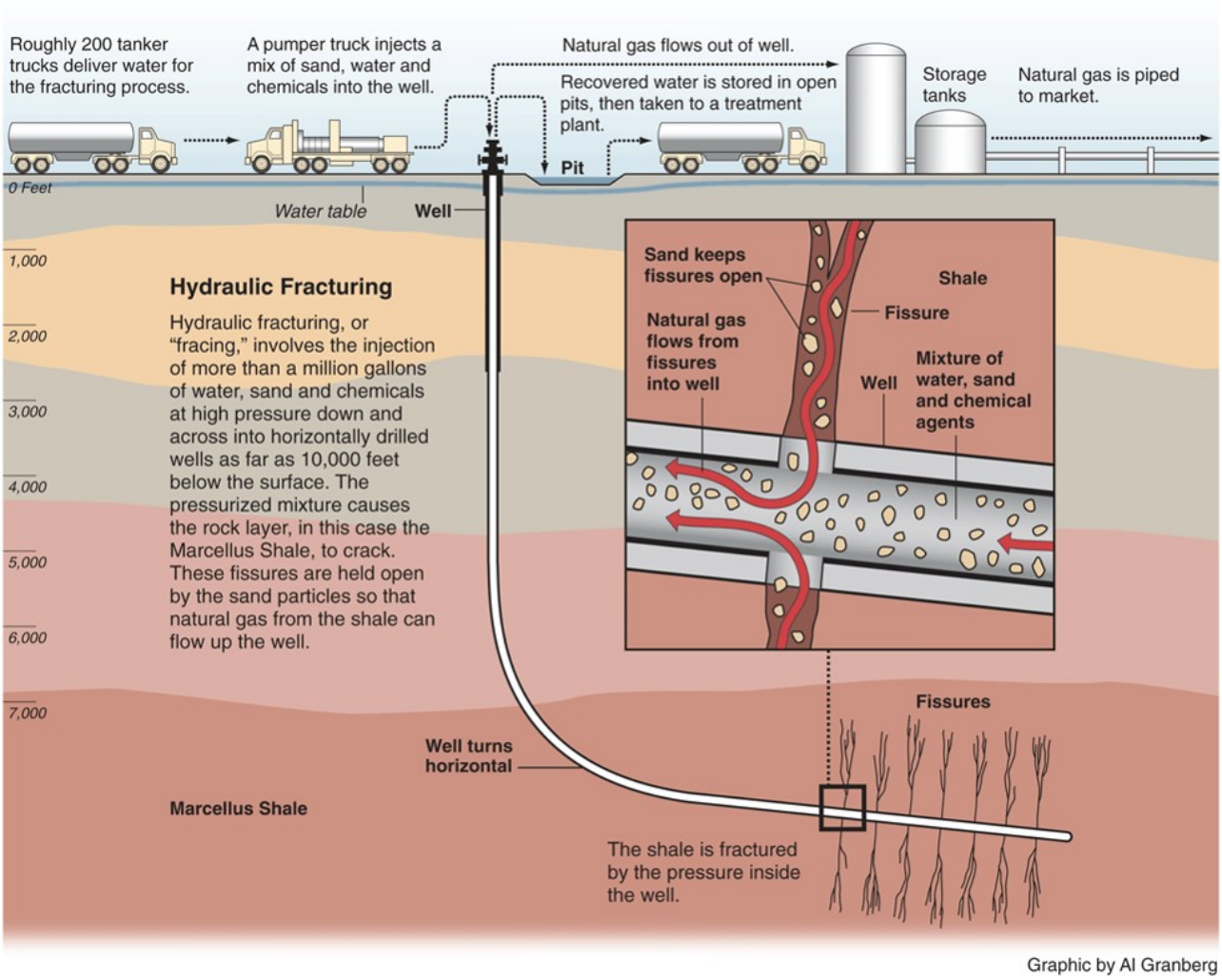

Figure 1.1: A schemtic diagram of a hydraulic fracturing operation. Graph: Al Granberg

treatment. The fluid should have the ability to generate artificial fractures as well as transport the proppant over long distances in the formation. A common composition of fracking fluids comprises $85-95\%$ of carrying fluid, $3-14\%$ of proppant, and approximately 1% of chemical additives which enhance the carrying abilities of the base fluid. Fluid viscosity and density are two factors that can affect the fracture generation and proppant transport. Low-viscosity fluids are commonly injected at high rates with low proppant concentration to generate narrow fractures. To minimise the impact of tip screen-out (i.e. the bridging of the injected particles in the fracture), the injection rates have to be sufficiently high for proppant transport. Fluids with high viscosity are injected at low rates to carry highly concentrated proppant to generate wider fractures. Various density categories of fracking fluids including water-based fluids, oil-based fluids and foam fluids have been widely applied in practice, depending on the formation properties. In general, water-based fluids are appropriate for a large number of unconventional gas reservoirs, while foam fluids can be used to assist with fracking low-pressure zones. After the treatment, a proportion of the fracking fluid is flowed back to the well, either to be recycled for further treatments or to be disposed of. The rest remains in the formation, having been lost due to fluid leak-off.

One important factor in hydraulic fracturing is proppant embedment, which affects the long-term permeability of the induced fractures and the productivity of the reservoir. An appropriate proppant concentration must be selected to ensure the optimal conductivity of the fracture, noting that excessive proppant may cause fracture blockage. In addition, an ideal proppant should have sufficient mechanical strength to withstand the closure

stress of the reservoir in order to keep the fractures open. Rapid developments in materials engineering have expanded the range of available proppant from commonly-used sand and ceramics to polymer coated particles [5] with higher strength. Traceable proppant has also been applied to the industry [6]. The size distribution of the proppant is also of great importance to proppant selection. Large proppant particles are typically placed in the large fractures near the wellbore, while small proppant particles are transported to more remote locations to keep small fractures open. However, in some cases large proppant particles can settle near the opening of the small fractures which causes channel blockage and reduces fracture conductivity. In order to avoid such issue, Khanna et al. [7] suggested a *graded proppant injection* technique, in which the proppant is sequentially injected with increasing size and decreasing concentration [8].

Originally targeted at enhancing the permeability of low-permeability formations such as coal seams and shales, the hydraulic fracturing technology has been extended to be applied to some high-permeability reservoirs whose permeabilities can reach up to 2 Darcys [9, 10]. During the second half of the 20th century, hydraulic fracturing was utilised in 70% of the gas reservoir exploitation in North America [9]. According to the statistics provided by the Commonwealth Scientific and Industrial Research Organisation (CSIRO), hydraulic fracturing has been widely applied to the coal seam gas (CSG) wells in Australia and the number of well completions can be counted in millions around the world.

1.2 Literature Review on Modelling Methods

As the power of computational hardware has grown, numerical modelling has played an increasingly important role in the understanding and prediction of the hydraulic fracturing process. However, it still remains a challenge for engineers and researchers to develop a comprehensive framework to accurately and effectively simulate the hydraulic fracturing process. Even in the most basic description, the modelling of hydraulic fracturing comprises three complicated aspects, namely the deformation of the fracture surface due to the injected fluid, the rheology of the fluid and proppant within the stimulated zone, and the fluid-driven fracture propagation [11]. Individually, numerical models have been developed and validated for each of these aspects [12]. For example, in the context of fracture propagation modelling, the first significant contribution (known as known as the PKN model) emerged in the 1950's [13, 14]. Based on the same state of 2D plane strain, the KGD model [15, 16] was developed almost at the same time. Both PKN and KGD models are still sometimes put into practice, while in most cases pseudo-3D (P3D) models are chosen for their efficiency and low computational cost [11]. It is worth mentioning that all the fracture propagation models mentioned above have already taken the fluid loss into consideration, whether approximately or through further extensions. This issue of fluid leak-off is further discussed in the following section.

1.2.1 Proppant Transport and Settlement

During a hydraulic fracturing treatment, the injected fluid and proppant particles play a significant role in keeping the induced fractures open, thus enhancing the well performance. As a result, the trajectory of the proppant and its settlement behaviour are major factors in a successful operation [17]. Both experimental analysis and numerical simulations have been performed to predict the transport and settlement of proppant, as it is the key to the conductivity of the artificial fractures after hydraulic fracturing, thus determining the productivity of the stimulated reservoir [18]. The transport and settling of proppant in fractures are usually resolved by dealing

with fluid flow of the slurry (i.e. the mixed continuum of the fluid and proppant) instead of solving equations individually for the two components [11].

The movement of the mixed continuum is governed by a convection equation expressed as,

$$\frac{\partial (aw)}{\partial t} + \bigtriangledown \cdot (awv_p) = 0, \tag{1.1}$$

where a is the proppant concentration, w is the fracture width and v_p is the velocity vector of the proppant.

In the research by Mobbs and Hammond [19], a parameter termed the buoyancy number was introduced to model the proppant transport with gravity-driven vertical movement. The buoyancy number was defined as the ratio of the typical convection velocity to the mean axial flow velocity. Larger buoyancy number indicated stronger convection mechanism. The simulation results of the non-uniformly distributed proppant across the fracture width were compared with those from a special case where the proppant were uniformly distributed. In the latter case, all the proppant were assumed to migrate rapidly to the centreline of the fracture, thus forming a close-packed flow. Consequently, slightly stronger transport rate and greatly enlarged settling rate were witnessed in the sheet flow. On the contrary, good vertical motions were observed in the homogeneous slurry comprising of fluid and proppant. In the recent work by Dontsov and Pierce [20], the newly developed model was able to track the generation and the growth of the plug-in process of the proppant in the fracture tip region, including the tip screen-out. The results also showed that the proppant tends to form a rigid assembly, whose size was dependent on the particle concentration, near the centre during transport. However, as the gravitational movement of the proppant induced asymmetry, this model was unable to capture this feature as it was based on the assumption of uniform pressure over the entire height of the fracture.

Generally, the settling velocity of the proppant is governed by Stokes law,

$$v_{p,st} = \frac{(\rho_p - \rho)\, g d_p}{18\mu}, \tag{1.2}$$

where ρ_p and ρ are, respectively, the particle density and fluid density, g is the acceleration due to gravity, d_p is the diameter of the particle, and μ is the dynamic viscosity of the fluid.

As an improvement, the viscosity term is replaced by the viscosity of the slurry, instead of using the viscosity of the base fluid. This modified viscosity is given by,

$$\mu_{slurry} = \mu_0 \left(1 - a/a_*\right)^B, \tag{1.3}$$

where μ_0 is the effective viscosity of the fluid, a^* is the saturated concentration of the proppant, B is a negative coefficient which is usually chosen between -3 to -1 in accordance with experimental data [21]. It can be observed that the computational viscosity increases with the rise in proppant concentration. However, one problem with this model is that as the concentration reaches some limit, the slurry would begin to act more like a solid than a fluid, which would be inappropriate [11].

Gadde et al. [22] proposed several modifications for the modelling of proppant settling in ungelled fracturing fluids, accounting for factors comprising of inertial effects, proppant concentration, fracture width and turbulence. In their study, the rheology of the mixture was controlled by the fluid viscosity and proppant concentration. Meanwhile, higher fluid velocities took the turbulence effects into consideration. In addition, the inertial effects were induced by the increase in the relative velocities between the fluid and the particles. Regarding the results and conclusions, smaller fracture widths, higher proppant concentration, and smaller particle sizes resulted in smaller settling velocities, while the turbulence effects cause higher settling velocities.

Asadi et al. [18] conducted experiments using a High Pressure Simulator (HPS) to study the settling of proppant under both static and dynamic conditions. In this study, the power law model was applied for the fluid flow. It was observed that the proppant settling velocity is nonlinearly dependent on the fluid shear rate. Meanwhile, the settling rate depended on the type of fluid used. The settling rate increased with the rise in shear rate of borate-crosslinked guar gel, while it decreased in linear guar gel as the shear rate increased. The study by Liu and Sharma [23] investigated various factors which could affect the proppant settling velocity. The most dominant factor was found to be the proppant size which led to the wall effects. The effect of fracture walls as well as their roughness was reported to be more significant for more viscous fluids. When the size of the particle became more comparable with the fracture width, severe reduction was observed in the settling rate due to an increase of the wall effects. As an ideal approach to validating the numerical results, such experimental research on proppant transport and settling could provide better instructional guidelines in the selections of the fracturing fluid and proppant properties.

1.2.2 Fracking Fluid Modelling

Besides the mechanical behaviour of the fractured formation and proppant transport, another significant part of the hydraulic fracturing process is the characterisation of the flow comprising the fracturing fluid and proppant through the porous media. Several aspects of the base fluid have been demonstrated to affect the hydraulic fracturing process such as the viscosity, pH, and the concentration of the solvent [24]. With the inclusion of moving particles, conventional simulation techniques based on finite element and finite volume solutions of the Navier-Stokes equations with moving boundaries, face a number of challenges. Continuously generating the newly adapted mesh according to the changing geometry brings extensive computational cost, especially in three dimensions [25].

During the hydraulic fracturing process, the flow regime can be divided into three categories, namely flow in a single fracture, flow in the porous medium, and fluid leak-off which denotes the fluid loss from the induced fractures to the natural formation [12]. Conventionally, the fluid flow within a single fracture is described by Poiseuille flow, considering that the fracture width is small compared to the fracture length [26].

The governing equation of the fluid flow is given by,

$$q = -\frac{w^3}{\mu}\frac{\partial p}{\partial x}, \tag{1.4}$$

where q is the flow rate and p is the fluid pressure, w and μ remain the fracture width and dynamic viscosity of the fluid, respectively.

Under the assumption that the fluid is incompressible, the fluid flow satisfies the local volume conservation law, which is expressed as,

$$\frac{\partial w}{\partial t} + \frac{\partial q}{\partial x} = 0, \tag{1.5}$$

Substituting Eq. (1.4) into Eq. (1.5) results in the Reynolds equation,

$$\frac{\partial w}{\partial t} + g = \frac{1}{\mu}\frac{\partial}{\partial x}\left(w^3\frac{\partial p}{\partial x}\right). \tag{1.6}$$

The above equations were numerically tested by Bunger et al. [27] and Adachi and Detournay [26]. Both studies were conducted in the 2D fracture propagation case under plane strain conditions, in which the moving

meshes and tip behaviours were taken into consideration. Having proposed semi-analytical asymptotic solutions to the problem as the final remarks, the numerical simulations yielded first-order accuracy.

A modified version of Eq. (1.6) in the case of 2D fluid flow in a planar fracture under elastic medium conditions was derived by Adachi et al. [11]. The modified equation is written as,

$$\frac{\partial w}{\partial t} = \bigtriangledown \left[\frac{w^3}{12\mu} \left(\bigtriangledown p - pg \right) \right] + \delta \left(x,y \right) Q, \tag{1.7}$$

where $\delta \left(x,y \right)$ is the Dirac delta function, while Q denotes the source injection rate.

Expanding the fluid flow scale from a single fracture to a porous medium, the governing equation of the fluid flow is given by Darcy's law, which is written as,

$$u = - \left(\frac{k}{\mu} \right) \left(\bigtriangledown p - pg \right), \tag{1.8}$$

where u is the Darcy velocity and k is the permeability of the formation. However, this equation is based on the assumption that the porous matrix is isotropic, which is not usually true. To make it more applicable and practical, the pressure p should be replaced by $\tilde{p}$ which is calculated from the harmonic average equation. Meanwhile, the scalar permeability, k, should be modified to a tensor quantity [28]. Consequently, Eq. (1.8) is modified as,

$$u = -k \cdot \frac{\bigtriangledown \tilde{p}}{\mu}. \tag{1.9}$$

Combining the conservation of mass and Darcy's law results in the conventional linear diffusion equation, which is written as,

$$\frac{\bigtriangledown^2 \tilde{p}}{\mu} = \frac{\varphi}{k} \frac{\partial p}{\partial t}, \tag{1.10}$$

where φ is the matrix porosity.

Generally, the conventional numerical simulations are based on the assumption that the fracture is sufficiently long and is saturated with fracking fluid. Hence the following boundary conditions are satisfied at the injection point,

$$q \left(0,t \right) = Q/2H, \tag{1.11a}$$

and,

$$p \left(0,t \right) = p_f, \tag{1.11b}$$

where H is the average reservoir layer height where the fracture is located.

At the tip of the fracture, the boundary conditions are described as,

$$w \left(x,t \right) = q \left(x,t \right) = 0. \tag{1.12}$$

Before the injection of the fracturing fluid, the pressure distribution within the reservoir is assumed to be constant, which is,

$$p \left(x,0 \right) = p_\infty, 0 < x < \infty. \tag{1.13}$$

In many of the numerical simulations, it is also assumed that a zero flux condition is satisfied around the surface of the fracture, which is expressed by the terms in Eq. (1.7),

$$\frac{w^3}{12\mu}\vec{n}\cdot(\bigtriangledown p - pg) = 0, \tag{1.14}$$

where $\vec{n}$ represents the outward normal vector to the fracture perimeter. However, this boundary condition is not applicable to a comprehensive numerical simulation where the fluid leak-off is taken into consideration.

1.2.3 Fluid Leak-Off in Hydraulic Fracturing

During a hydraulic fracturing treatment, the fracturing fluid flows to produce artificial fractures, while some of the fluid leaks into the natural formation through the fracture face due to the net fracture pressure. Such fluid loss is termed the fluid leak-off, which has drawn great attention from researchers and engineers as it could be a dominant factor affecting the fracture geometry and the efficiency of the hydraulic fracturing treatment. If not adequately controlled, the leak-off fluid could exceed 70% of the injected fluid volume. In some high-permeability reservoirs with more natural fractures, this fraction could even reach 90% [11, 29]. Hence it is important to involve the fluid leak-off in hydraulic fracturing simulations.

The first attempt was taken by Carter, who proposed the well-known Carter model in the 1950's [30]. In its most simplified form, the Carter model can be calculated as,

$$g_L(x,t) = \frac{C_L}{\sqrt{t - t(x)}}, \tag{1.15}$$

where g_L is the leak-off rate, C_L is termed the leak-off coefficient, $t(x)$ stands for the time at which the fracture reaches the position, x, and t is the total operation time.

Taking the fluid leak-off term into consideration, the conservation law which is expressed by Eq. (1.5) is modified as,

$$\frac{\partial w}{\partial t} + \frac{\partial q}{\partial t} + \frac{C_L}{\sqrt{t - t(x)}} = 0. \tag{1.16}$$

Theoretically, this model can be classified into three regimes. First, when fracturing fluid flows past the fracture face, the deposition of the dense particles would form a so-called filter cake, which is a thin layer with low permeability. Second, the filtrate process in which the fluid penetrates the filter cake, which is also defined as the growth of an invaded zone. Third, the fluid flows into the reservoir zone, which is also termed the uninvaded zone [10, 31–34].

Based on the 1D diffusion process, the classical time-dependent Carter model has its limitations due to the assumptions involved, which are listed as,

- the flow of the leak-off fluid is linear and orthogonal to the fracture face,
- the width of the fracture and the pressure therein are uniform,
- the properties of the fluid and formation are constant.

Although having been used as the standard model in many cases [27, 35, 36], an extensive number of extensions have been made to overcome the drawbacks of the Carter model. As an example, the exploration of pressure-dependent leak-off [34, 37–39] which incorporates the change in pressure drop across the three zones mentioned

before is a good supplement to the original model. In addition, Hagoort et al. [40] observed the existence of an obvious leak-off component along the direction of the fracture, which could be decreased by larger injection rates. Hence the 2D model [41] and 3D model [42, 43] were proposed to account for non-orthogonal leak-off mechanisms. In the 3D leak-off model by Dean and Schimit [44], great progress was made to allow the porosity of the formation to change according to the fluid pressure during the fracking process. This flexible model was able to characterise the increased leak-off effect due to enhanced porosity and permeability.

In the recent research of Yarushina [10], the compaction and decompaction of the formation including the pore compressibility and porosity-dependent permeability were first taken into consideration, thus generating a more comprehensive model for pressure-dependent leak-off. Regarding the aspect of fluid properties, the non-Newtonian extensions which are mostly based on the power-law fluid model with a moving boundary between the invaded zone and reservoir region have been developed [34, 45]. In another study by Mikhailov et al. [46], the fracking fluid used was modelled as shear-thinning fluid, while the leak-off fluid was assumed to be Newtonian. However, Yi and Peden [34] emphasised that such an assumption would result in erroneous leak-off and proper composition should be chosen for the leak-off fluid to ensure a reasonable leak-off prediction. Research has shown that the volume of the leak-off fluid could be controlled by increasing the viscosity of the fracturing fluid [29, 46], thus improving the efficiency of the hydraulic fracturing treatment. However, another consideration of the high friction resistance of both the equipment and the formation should be taken at the same time (i.e. increased pumping power requirements), which would restrain the viscosity at a certain range [29].

1.2.4 Non-Newtonian Modelling of Fracking Fluids

In the case of a Newtonian fluid, the constitutive relationship between the shear stress, τ_s, and strain rate, $\dot{\gamma}$, is expressed as,

$$\tau_s = \mu \dot{\gamma}, \tag{1.17}$$

where μ is the fluid viscosity.

In many industrial applications such as hydraulic fracturing, the complex particle suspensions show non-Newtonian behaviour [47]. Meanwhile, as introduced in Section 1.1, common fracking fluids contain supplementary chemical additives, which also contributes to the shear-dependent viscosity of the overall fracking fluid [28]. Consequently, it is convenient to treat the fracking fluids as a Non-Newtonian fluid in some cases. In order to provide more reliable and more practical information for the industry, the extensions for non-Newtonian fluids have drawn attention during the last two decades, the majority of which focuses on power law fluids.

In the case of a power law fluid, the viscosity is a function of the local strain rate, which is calculated as,

$$\mu = \mu_0 \left(\dot{\gamma}\right)^{n-1}, \tag{1.18}$$

where μ_0 is the consistency constant and n denotes the power law index. The cases in which $n < 1$ correspond to shear-thinning fluids, while in the cases of $n > 1$ the fluid shows shear-thickening behaviour. With $n = 1$, a Newtonian fluid is recovered.

To model the power law fracking fluids in a 2D planar fracture, Adachi et al. [11] modified Eq. (1.7) as follows,

$$\frac{\partial w}{\partial t} = \bigtriangledown \left[D\left(w,p\right) \left(\bigtriangledown p - pg \right) \right] + \delta \left(x,y\right) Q, \tag{1.19}$$

in which,

$$D\left(w,p\right) = N^{'} w^{(2n+1)/n} \left| \left(\bigtriangledown p - pg \right) \right|^{(1-n)/n}, \tag{1.20}$$

$$N^{'} = \left(\frac{n}{2n-1} \right) \left(\frac{1}{2^{n+1} K^{'}} \right)^{1/n}, \tag{1.21}$$

and,

$$\left| \left(\bigtriangledown p - pg \right) \right| = \sqrt{\left(\frac{\partial p}{\partial x} - \rho g_x \right)^2 + \left(\frac{\partial p}{\partial x} - \rho g_y \right)^2}. \tag{1.22}$$

where $K^{'}$ is the consistency parameter, and g_x and g_y are, respectively, horizontal and vertical components of the gravity vector. It is worth mentioning that if one takes $n = 1$ and $K^{'} = \mu$, Newtonian fluid flow can be recovered.

Considering the fluid leak-off term as an additive to Eq. (1.19), the Non-Newtonian modelling of the power law fracking fluids is expressed as,

$$\frac{\partial w}{\partial t} = \bigtriangledown \left[D\left(w,p\right) \left(\bigtriangledown p - pg \right) \right] + \delta \left(x,y\right) Q - \frac{C_L}{\sqrt{t - t\left(x\right)}} - 2 S_0 \delta \left[t - t\left(x,y\right) \right], \tag{1.23}$$

where S_0 represents the initial rapid leak-off volume before the filter cake is formed around the perimeter of the fracture.

For the purpose of modelling the fluid leak-off mechanism, Torok and Advani [48] implemented a model where the reservoir was originally saturated with Newtonian fluid before the injection of the Non-Newtonian fracking fluid. During the process of hydraulic fracturing operation, the reservoir fluid was pushed in a piston-like manner. Consequently, the fluid in the reservoir could be divided into two regions. One was the natural reservoir fluid and the other was the marching fracking fluid. This model required additional continuity boundary conditions of both pressure and velocity at the interface of the two fluids at $x = a(t)$, which is written as,

$$p_1 \left[a\left(t\right), t \right] = p_2 \left[a\left(t\right), t \right], \tag{1.24}$$

and,

$$\left[-\frac{k}{\mu} \frac{\partial p_1}{\partial x} \right]^{n/1} = -\frac{k}{\mu_r} \frac{\partial p_2}{\partial x}, \tag{1.25}$$

where μ_r is the viscosity of the original reservoir fluid.

The position of the interface is tracked by,

$$\left[-\frac{k}{\mu} \frac{\partial p_1}{\partial x} \right]_{x=a(t)}^{1/n} = \phi \frac{da}{dt}. \tag{1.26}$$

However, for a comprehensive numerical simulation, these non-linear integral boundary condition equations must be solved numerically, which is non-trivial.

To compute the power law fluid velocity in the fracture, Darcy's law should be modified by introducing the power law exponent, n, which is written as,

$$u = -\frac{1}{2\mu_0}\left(\frac{n\phi}{1+3n}\right)^n \left(\frac{8k}{\phi}\right)^{(n+1)/2} (\bigtriangledown p - pg), \tag{1.27}$$

while the pressure distribution inside the fracture is calculated as,

$$\bigtriangledown^2 p \left(\frac{\partial p}{\partial x}\right)^{(1-n)/n} = n\phi \left(\frac{\mu}{k}\right)^{1/n} \frac{\partial p}{\partial t}. \tag{1.28}$$

Again, Newtonian fluid flow can be recovered when $n = 1$.

1.3 Project Scope and Research Significance

The rheology of fracking fluids has a significant influence on the performance of a hydraulic fracturing treatment. Meanwhile, the modelling of the hydraulic fracturing process is a multi-phase problem which is affected by various factors, including the natural formation properties, the injection rate, the fluid type, the proppant properties, and the interactions between the fluid and proppant. All of these factors should be appropriately considered for a high-fidelity simulation, which brings considerable computational difficulties. In addition, the Non-Newtonian modelling approaches focus on the global behaviour of the fracking fluid and treat the fluid and particles as a continuum. Therefore, the non-Newtonian models are not able to accurately capture the hydrodynamic interactions between fluid and particles, and the interactions between particles. In light of the rapid growth of hydraulic fracturing and its complexities, an efficient and accurate numerical approach is required to understand the interaction of fluids and particles in hydraulic fractures.

Therefore, the aim of this research is to use a direct numerical simulation strategy to investigate the hydrodynamic interaction of proppant and fluid in hydraulic fractures at the particle scale.

To support the aim of this research, the following objectives have been listed as:

- Implement and validate a computational model for fluid-particle coupling and compare the results with the existing models (which have known problems);
- Verify and improve the implemented model to overcome the existing computational issues of the approach (i.e. the viscosity-dependence and time stepping);
- Apply the improved computational model to a particle-scale shear box to characterise the shear-dependent rheology of particle suspensions, at varying solid volume fraction and shear rate;
- Apply the improved computational model to a small-scale model of a fracture, and use it to investigate the permeability of the fracture under the influence of proppant embedment;
- Use the fracture permeability results to predict the performance of hydraulic fracturing in well productivity enhancement using a semi-analytical solution from the literature.

The successful completion of this project will provide new fundamental insights on the behaviour of hydraulic fracturing fluids. The modelling of the fluid and proppant injection in the fracture network can provide particle-scale knowledge of hydraulic fracturing as well as the utilisation of the natural fractures. The

outcomes of this research will assist with the selection of fluid and proppant properties as well as an optimal distribution of proppant in fractures, leading to a more accurate and more reliable modelling of hydraulic fracturing. Consequently, these theories and predictions could be modified or improved to better serve the industry, contributing to optimal hydraulic fracturing treatment planning, considering both the cost and the benefit.

The need for the research and development of predictive tools which are capable of both informing the public debate and guiding operations has been made clear by governments and universities around the world. By addressing this urgent need, this project will help demonstrate that natural gas production can be undertaken in a safe and sustainable fashion, address public concerns related to the industry, and maximise its economic benefit.

1.4 Modelling Approach to This Project

During the last two decades, simulations of the hydraulic fracturing process and the search for an alternative approach of the conventional computational fluid dynamics (CFD) have attracted considerable interest from researchers. Having emerged as a powerful approach to simulate the behaviour of fluid flows, the lattice Boltzmann method (LBM) [49–51], which was originally proposed in the 1980's, is now applied to a range of problems, including hydrodynamics, thermal and multiphase flows, flows in porous media and characterisations of turbulences [52]. As an improvement of the general lattice gas automata (LGA), the LBM uses density distribution functions as the primary variable. Instead of treating the fluid as a continuous medium, the LBM uses a regular grid to discretise the fluid domain. Hence, the fluid is modelled as a group of particles which are only allowed to move to their adjacent lattice nodes or stay at rest. Furthermore, the fluid flow is simulated by tracking the evolution of the fluid particle distributions. By updating the density distribution functions and thus calculating the macroscopic properties of the fluid with each time step, macroscopic flow regimes can be simulated. This straightforward and explicit time-stepping approach shows great advantages over the conventional CFD technique, including high space-time resolution, good flexibility for parallel computations, and robustness when dealing with complex geometries [53].

In many LBM based multi-phase simulations, the interactions between suspended particles are either ignored or to some extent treated in a simplified pattern. However, to obtain more accuracy in many practical problems, such interactions must be taken into consideration. To resolve the fluid-particle system, the discrete element method (DEM) [54] has been employed to model the behaviour of the solid particles. Originally aimed at solving geotechnical applications, the DEM treats the granular system as an assembly of rigid elements, usually with simple geometric entities such as spheres. Governed by Newton's second law, the dynamic interactions of the discrete elements are characterized by their overlap and contact force. Normally the discrete system is solved by an explicit central difference time integration scheme, which is somewhat consistent with the LBM [53]. This explicit nature in both methods provides the opportunity for a coupled LBM-DEM solution procedure to resolve the fluid-particle system.

Firstly proposed by Cook et al. [55], the LBM-DEM approach has displayed tremendous potential in the detailed characterisation of fluid and proppant flow in fractures. Fig. 1.2 illustrates the straightforward mapping of multiple spheres to a regular LBM grid, which reveals one of the advantages of the coupled LBM-DEM. As an extension, the partially saturated method (PSM) [56] has been introduced into the LBM-DEM framework to model the interactions between the fluid and moving particles, which is applied to the current research.

The direct numerical simulations of small to intermediate scale fracture flow scenarios have already validated the framework in abundant 2D models [25, 55, 57–59]. While the LBM was originally developed mainly for laminar flows, as the Reynolds number increases, the fluid exhibits turbulent behaviour. To tackle this issue, Yu et al. [60] incorporated a turbulence model which is based on Large Eddy Simulation (LES) [61] into the LBM-DEM framework by adding a viscosity term which is calculated from the sub-grid turbulence model. Later the LBM-DEM framework was also extented to 3D applications [53, 62–65].

In this project, the modelling of the complex, consolidated particle suspensions will employ the DEM to represent the particles and the LBM to represent the base fluid in the suspensions. Hydrodynamic coupling between the LBM and DEM will be undertaken using a form of immersed boundary, known as the partially saturated method (PSM). Direct numerical simulation (DNS) of small-scale flow configurations can be used to determine the influence of fracture geometry and fluid and particle properties on proppant injection.

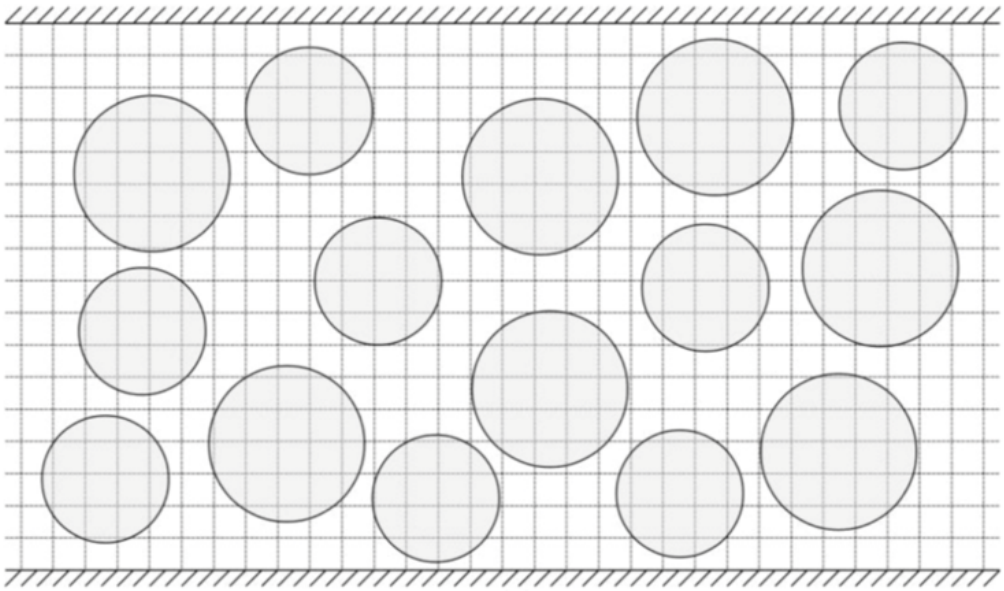

Figure 1.2: The straightforward mapping of spherical discrete elements to the LBM grid.

Within the scope of industrial applications, especially in hydraulic fracturing treatments, the fluid flows usually show non-Newtonian behaviours when polymers and or colloids are contained [47]. To fulfil this practical requirement, extensions to the LBM framework for non-Newtonian fluid flows are well developed [52, 66–70].. in which a power-law model is applied. Further improvements and modifications have been made to address the limitations of the power law model, such as the truncated power law model [71]. Another popular non-Newtonian fluid model is the Bingham yield-stress model [72]. However, limited work has been published for the Bingham plastics within the scope of LBM simulations [73–76]. Nevertheless, the non-Newtonian extensions to LBM-DEM simulations have been widely applied to provide more accurate and practical results.

1.5 Thesis Layout

This thesis consists of six chapters. In addition to this introductory chapter, Chapter 2 presents a detailed description of the numerical framework applied to this project. The fundamental knowledge of both the LBM and DEM is introduced, such as the lattice geometries and relaxation process of the LBM and the contact laws

and basic formulation of the DEM. In Section 2.3, various fluid-solid boundary conditions are introduced and compared.

In Chapter 3, computational issues related to LBM-DEM coupling (e.g. viscosity-dependence and time stepping) are introduced and discussed. The performance of the implemented two-relaxation-time (TRT) PSM is firstly tested and compared with a published flow configuration. A modified PSM solid weighting function is then proposed to minimise the viscosity-dependence, followed by tests through a range of benchmark flow problems which have analytical solutions for validation. Comparisons are also made with the BGK collision operator, highlighting the improvement of the implemented TRT-PSM framework.

Chapter 4 and Chapter 5 present applications of the improved LBM-DEM framework proposed in Chapter 3 in hydraulic fracturing modelling. Numerical modelling of particle suspensions is demonstrated in Chapter 4. A flow rheometer is simulated to study the rheology of shear-dependent flow, for which experimental-based empirical solutions are available for comparison. In Chapter 5, analysis of propped fractures is presented, investigating the influence of proppant embedment on fracture conductivity and well performance with different proppant concentrations and varying confining stresses.

The outcomes of this research are summarised in Chapter 6, along with the potential directions of future work.

Chapter 2

Numerical Modelling of Particle Suspensions

In this research, the modelling of complex, consolidated particle suspensions will employ the lattice Boltzmann method (LBM) to represent the base fluid and the discrete element method (DEM) to represent the particles. Hydrodynamic coupling between the LBM and DEM will be undertaken using a partially saturated method (PSM). Current research on the numerical rheometry of fluids and granular suspensions will be extended to capture the rheology of both the suspensions and the base fluid.

2.1 The Lattice Boltzmann Method

The origin of the LBM can be traced to the lattice gas automata (LGA) which was proposed by Hardy et al. [77, 78] in the 1970's. In the original LGA model (i.e. the HPP model), a 2D square lattice was used, on which each fluid node had four discrete velocity components. The model was constructed as a simplified, molecular dynamic models in which space is discretised by a symmetric lattice, time is discretised by an explicit time-stepping scheme, and velocity is discretised by a limited number of lattice-dependent components. The fluid flow is then simulated through the stream-collide process which is mathematically expressed as,

$$n_i\left(\mathbf{x}+\mathbf{e_i}\Delta t, t+\Delta t\right) = n_i\left(\mathbf{x},t\right)+\Omega_i, \tag{2.1}$$

where $\mathbf{x}$ is the position of the node and Ω_i is the operator describing the collision process. The Boolean variable, $n_i\left(\mathbf{x},t\right)$, can be 0 or 1, representing the number of particle variables moving to the discrete velocity $\mathbf{e_i}$.

Understanding that the lattice symmetry of the HPP model was not sufficient to capture the hydrodynamic behaviour of the gas, Frisch et al. [79] proposed an improved model (i.e. the FHP model), in which a triangular lattice with hexagonal symmetry was utilised, allocating each lattice node with six velocity components. The work by Frisch et al. [79] also highlighted the importance of lattice symmetry to the recovery of the Navier-Stokes equations. Based on the FHP model, the continuous Navier-Stokes equations were recovered for the first time from the LGA model, which built a good foundation for the development of the LBM.

During the past few decades, the LBM [49–51] has emerged as a powerful numerical method for fluid modelling. In conventional computational fluid dynamics (CFD) the fluid domain is defined as a continuum, in which the macroscopic properties, such as velocity and pressure, are obtained by discretising and solving the Navier-Stokes equations. In the LBM, however, the fluid domain is discretised at the mesoscopic scale where

the primary variables are density (or particle) distribution functions, f_i, of the fluid nodes. By constructing simplified kinetic models which incorporate microscopic to mesoscopic processes, the LBM focuses on the average macroscopic behaviour of the fluid nodes in the system, so that the model exhibits the same macroscopic behaviours as the classical hydrodynamic models [80]. During each iteration of the LBM, two processes, namely the collision and streaming, are performed. Collision redistributes the distribution functions that arrive at each node and then streaming propagates the redistributed functions to their neighbour nodes. The macroscopic properties are then calculated from the moments of the distribution functions at a lattice node. In the macroscopic limit it has been shown that the lattice Boltzmann equation (LBE), which is the governing equation in the LBM, recovers the Navier-Stokes equations in the near-incompressible limit under the condition of low computational Mach number [50].

Compared to conventional CFD approaches, the LBM has a number of advantages. In most LBM applications, a regular orthogonal grid is implemented. Although irregular grids [81–85] are also available for modelling, they are not within the scope of the current work. In addition, the collision process only requires local nodal computations while the streaming process can be performed in a straightforward manner by index shifting operations. The above features make the LBM an ideal approach for parallel computations, particularly for large-scale simulations. Meanwhile, many of the boundary conditions are implemented also using local procedures, enabling the LBM to incorporate particles and complex boundaries, which is ideal for numerical modelling of particle suspensions in hydraulic fractures.

2.1.1 The Lattice Boltzmann Equation

As an extension to Eq. (2.1), the lattice Boltzmann equation (LBE) is expressed as,

$$f_i(\mathbf{x}+\mathbf{e_i}\Delta t, t+\Delta t) - f_i(\mathbf{x},t) = \Omega_i, \tag{2.2}$$

where f_i is the density distribution function which is a real variable representing the probable amount of fluid density moving in a discrete direction at each node at each timestep. Ω_i is the collision operator, which controls the rate of relaxation of the density distribution function towards its equilibrium in the ith lattice direction.

It is sometimes convenient to rewrite the LBE in a simplified version which highlights the streaming process,

$$fi(\mathbf{x}+\mathbf{e_i}\Delta t, t+\Delta t) = f_i^+(\mathbf{x},t), \tag{2.3}$$

in which $f_i^+(\mathbf{x},t)$ is the post-collision density distribution function which is calculated through the collision process,

$$f_i^+(\mathbf{x},t) = f_i(\mathbf{x},t) + \Omega_i, \tag{2.4}$$

Fig. 2.1 presents the discretisation of a simple fluid domain and the location of the density distribution functions. Following collision, the streaming process moves the f_i to each of the neighbouring nodes in the velocity directions. From a mathematical perspective, the ordering of the streaming and collision processes within each timestep is not important, as the streaming process only requires index shifting without any calculations, which can also be observed from Eq. (2.3).

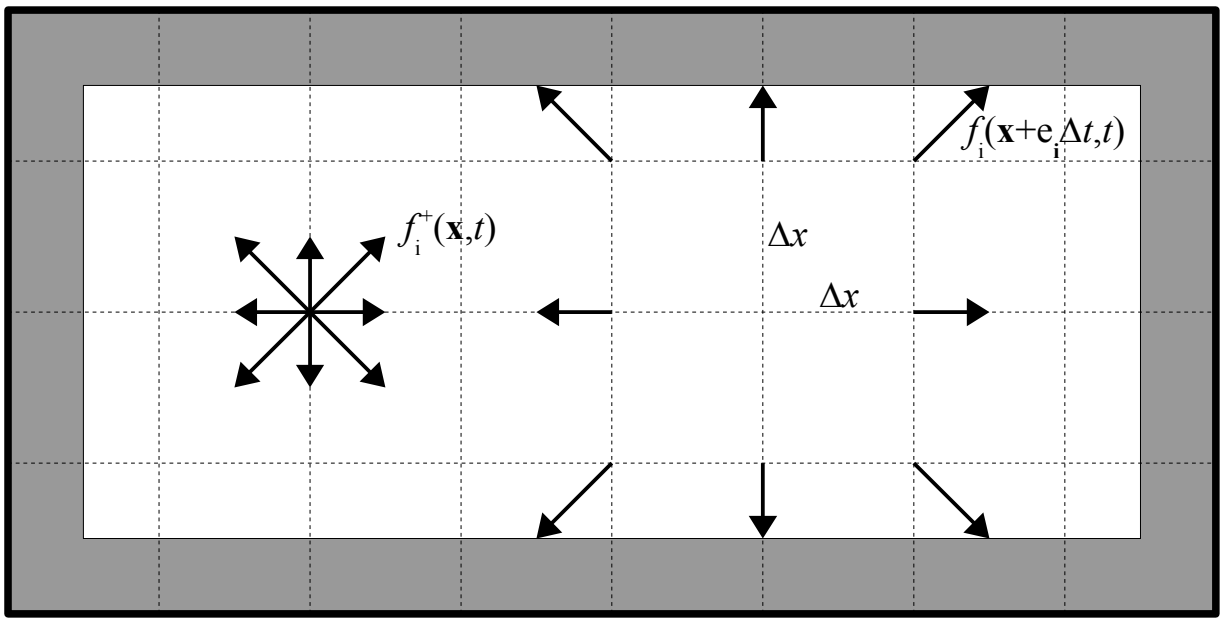

Figure 2.1: A schematic diagram of a discretised LBM domain showing (left) the density distribution functions after collision which are (right) then streamed to their respective neighbouring nodes [3].

The macroscopic properties of the fluid (i.e. the density, ρ, and velocity, u) are calculated as,

$$\rho = \sum_i f_i, \tag{2.5}$$

$$\rho \mathbf{u} = \sum_i f_i \mathbf{e_i}, \tag{2.6}$$

at each lattice node at each time step. The pressure, p, is calculated directly from the fluid density,

$$p = c_s^2 \rho, \tag{2.7}$$

where $c_s = c/\sqrt{3}$ is the fluid speed of sound and $c = \Delta x/\Delta t$ is the lattice speed.

It is worth pointing out here that that the link between the LBE and the Navier-Stokes equations is dependent on, amongst other things, the small velocity limit (i.e. the maximum macroscopic velocity, u_{max}, should be much less than the lattice speed, c). This can be interpreted in terms of the computational Mach number of a simulation,

$$Ma = \frac{u_{max}}{c_s}, \tag{2.8}$$

where it is required that $Ma << 1$ to ensure reasonable numerical accuracy and stability.

The kinematic viscosity of the fluid (in physical units), ν, is calculated as a function of the lattice spacing, Δx, the relaxation parameter, τ, and the timestep, Δt_{LBM},

$$\nu = \frac{1}{3}\left(\tau - \frac{1}{2}\right)\frac{\Delta x^2}{\Delta t_{LBM}}, \tag{2.9}$$

which can be rearranged for the calculation of the timestep,

$$\Delta t_{LBM} = \frac{1}{3}\left(\tau - \frac{1}{2}\right)\frac{\Delta x^2}{\nu}. \tag{2.10}$$

2.1.2 The Lattice Geometries

As stated in Section 2.1, for the LGA models, a minimum lattice symmetry is required to ensure isotropy of the velocity tensors and recovery of the Navier-Stokes equations from the kinetic model. The same geometry requirement also applies to the LBM. In general, the LBM geometry can be distinguished into 2D and 3D lattices.

2D

Various options are available for spatial discretisation in two dimensions, including hexagonal lattices (D2Q6, D2Q7) and orthogonal lattices (D2Q5, D2Q8, D2Q9).

As shown in Fig. 2.2(a), the difference between the D2Q6 and D2Q7 lattices is the null velocity, $\mathbf{e_0}$, in the latter, which represents a rest density distribution function at each node. In the hexagonal D2Q7 lattice, the discrete velocity vectors are expressed as,

$$\mathbf{e_i}\begin{cases} 0 & (i=0) \\ \mathbf{e}\left(\cos\left(\frac{\pi(i-1)}{3}\right), \sin\left(\frac{\pi(i-1)}{3}\right)\right) & (i=1,2,3,4,5,6) \end{cases}. \tag{2.11}$$

In an identical manner, the D2Q9 lattice has an additional null velocity component compared to the D2Q8 lattice, which is shown in Fig. 2.2(b), and the vectors which describe these discrete velocities are,

$$\mathbf{e_i}\begin{cases} 0 & (i=0) \\ \mathbf{e}\left(\cos\left(\frac{\pi(i-1)}{2}\right), \sin\left(\frac{\pi(i-1)}{2}\right)\right) & (i=1,2,3,4) \\ \sqrt{2}\,\mathbf{e}\left(\cos\left(\frac{\pi(i-5)}{2}+\frac{\pi}{4}\right), \sin\left(\frac{\pi(i-5)}{2}+\frac{\pi}{4}\right)\right) & (i=5,6,7,8) \end{cases}. \tag{2.12}$$

It has been shown that the D2Q9 lattice, in which the orthogonal grid is used, has revealed significantly better accuracy over the D2Q6 and D2Q7 lattices [86].

3D

To simulate fluid flows in three dimensions, Fig. 2.3 illustrates the D3Q15 (Fig. 2.3(a)) and D3Q27 (Fig. 2.3(b)) models which also incorporate the null velocity, $\mathbf{e_0}$, in the discrete velocity set.

The discrete velocity set $\mathbf{e_i}$ can be written as,

$$\mathbf{e_i}\begin{cases} (0,0,0) & (i=0) \\ \mathbf{e}(\pm1,0,0), \mathbf{e}(0,\pm1,0), \mathbf{e}(0,0,\pm1) & (i=1,...,6) \\ \mathbf{e}(\pm1,\pm1,\pm1) & (i=7,...,14) \end{cases}, \tag{2.13}$$

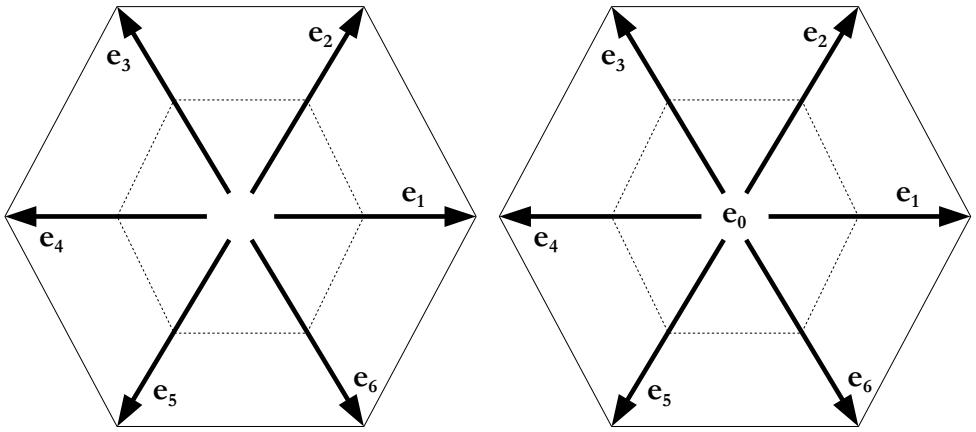

(a) D2Q6 and D2Q7

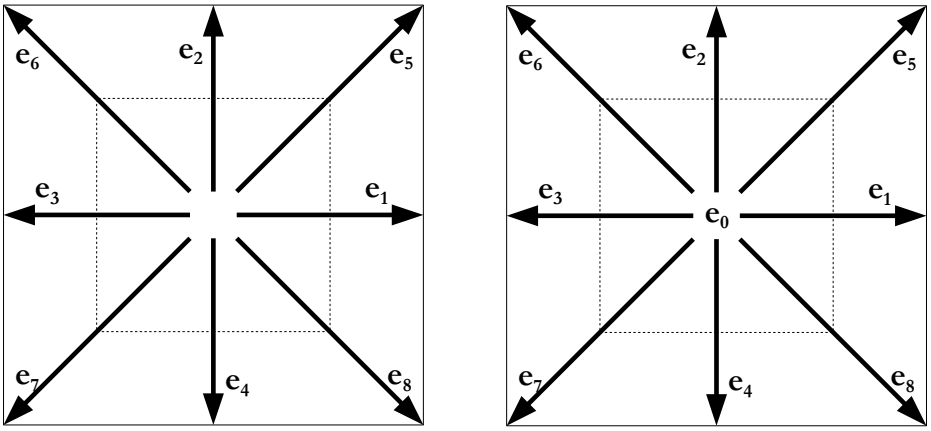

(b) D2Q8 and D2Q9

Figure 2.2: LBM domain discretisations in 2D: (a) D2Q6 (left) D2Q7 (right) and (b) D2Q8 (left) D2Q9 (right).

for the D3Q15 model and,

$$\mathbf{e_i}\begin{cases} (0,0,0) & (i=0) \\ \mathbf{e}(\pm1,0,0),\mathbf{e}(0,\pm1,0),\mathbf{e}(0,0,\pm1) & (i=1,...,6) \\ \mathbf{e}(\pm1,\pm1,0),\mathbf{e}(\pm1,0,\pm1),\mathbf{e}(0,\pm1,\pm1) & (i=7,...,18) \\ \mathbf{e}(\pm1,\pm1,\pm1) & (i=19,...,26) \end{cases}, \tag{2.14}$$

for the D3Q27 model.

The lattice discretises the fluid domain into a regular Cartesian (or hexagonal) grid, with nodes spaced at a distance, Δx. The density distribution functions, f_i, exist at each node and, in the case of the D3Q27 lattice, propagate along 26 velocity directions (there is one rest density distribution function, f_0, with zero velocity). In general, the increase in the number of discrete velocities improves the accuracy of the LBM. However, it also comes with an increased computational cost. As a result, it is important to balance the accuracy and computational expense when choosing the lattice geometry.

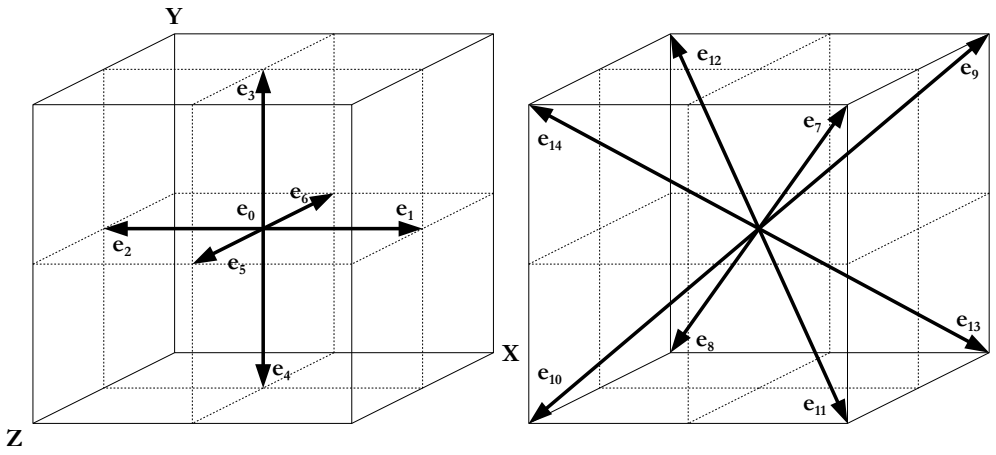

(a) D3Q15

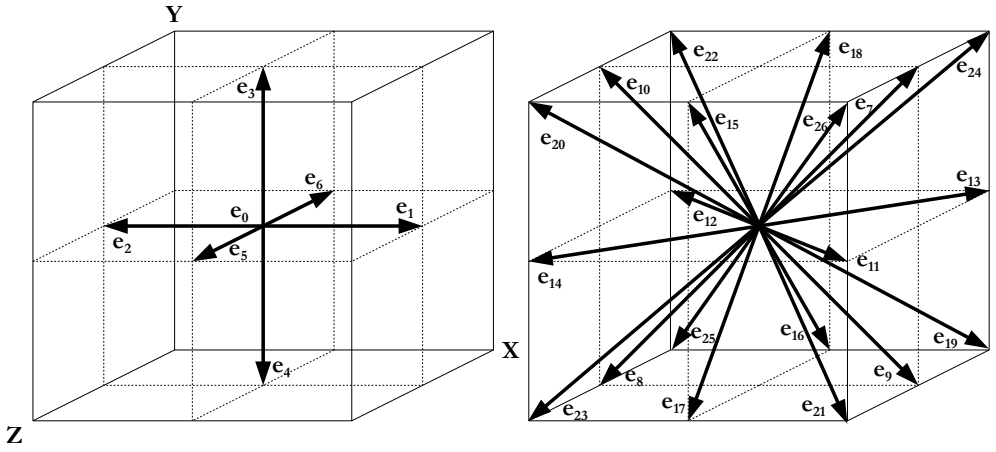

(b) D3Q27

Figure 2.3: LBM domain discretisations in 3D decomposed to their orthogonal and diagonal components: (a) D3Q15 and (b) D3Q27.

2.1.3 The Relaxation Process and Collision Operators

The relaxation (i.e. collision) process redistributes the density distribution functions that arrive at each node at each timestep. This process is local, which means that only the density distribution functions arriving at the particular node are taken into consideration. This feature highlights the parallel nature of the LBM, which makes it an ideal approach to solve large-scale problems. The collision operator, Ω_i, should satisfy the conservation laws at each node, which is expressed as,

$$\sum \Omega_i = 0, \tag{2.15}$$

for mass conservation and,

$$\sum \Omega_i e_i = 0, \tag{2.16}$$

for momentum conservation.

The most popular model used in the LBM is the Bhatnagar-Gross-Krook (BGK) model [87] with a single relaxation time approximation in the collision operator. However, when simulating fluid flow through porous media, the permeability, which should be an intrinsic property of the formation, becomes viscosity-dependent

[63]. Such instability is also reported in other works [88, 89]. This issue, and others, was addressed in part by dHumieres [90] via the development of the multiple-relaxation-time (MRT) model. In the MRT, a number of relaxation times are applied to moments of the density distribution functions, and a form of this model is applied in this research. The MRT model exhibits superior numerical stability and accuracy over the BGK model at the expense of greater computational cost. Nevertheless, it is still thought to be worthwhile especially when turbulence and non-Newtonian rheology emerge as important issues in the simulation [52]. In order to obtain improved accuracy and stability while maintaining reasonable computational expense, the two-relaxation-time (TRT) collision operator [91] was developed, which is applied to most of the simulations presented in this thesis.

The Single-Relaxation-Time Bhatnagar-Gross-Krook Model

To date, the BGK collision operator remains the most widely-used in the LBM, where it is defined as,

$$\Omega_i^{BGK} = -\frac{1}{\tau}\left[f_i(\mathbf{x},t) - f_i^{eq}(\mathbf{x},t)\right], \tag{2.17}$$

where τ is the relaxation parameter, which controls the rate at which f_i approaches its equilibrium value. The equilibrium density distribution functions, f_i^{eq}, are typically defined as a small velocity expansion of the Maxwell-Boltzmann equilibrium and expressed as,

$$f_i^{eq} = \omega_i \rho \left[1 + \frac{3}{c^2}(\mathbf{e_i}\cdot\mathbf{u}) + \frac{9}{2c^4}(\mathbf{e_i}\cdot\mathbf{u})^2 - \frac{3}{2c^2}(\mathbf{u}\cdot\mathbf{u})\right], \tag{2.18}$$

in which ω_i is the weighting factor. For the D2Q9 lattice,

$$\omega_0 \begin{cases} 4/9 & (i=0) \\ 1/9 & (i=1,2,3,4) \\ 1/36 & (i=5,6,7,8) \end{cases}. \tag{2.19}$$

For the lattices that are used in this work,

$$\omega_0 \begin{cases} 2/9 & (i=0) \\ 1/9 & (i=1,...,6) \\ 1/72 & (i=7,...,14) \end{cases}, \tag{2.20}$$

for the D3Q15 model, and,

$$\omega_0 \begin{cases} 8/27 & (i=0) \\ 2/27 & (i=1,...,6) \\ 1/54 & (i=7,...,18) \\ 1/216 & (i=19,...,26) \end{cases}, \tag{2.21}$$

for the D3Q27 model.

In the BGK model, it is assumed that the density distribution functions at each node relax at a single rate. However, this may cause instability in the cases where the momentum exchange and energy exchange during the relaxation process do not propagate at the same pace [92]. To overcome this issue, several modified BGK collision operators have been proposed such as the ellipsoidal statistical model [93].

The Multiple-Relaxation-Time Model

As discussed in Section 2.1.3, the hydrodynamic interaction of fluids and solids becomes viscosity-dependent when using a BGK-LBM formulation [4, 63]. The MRT collision operator [90] can help mitigate this problem, while also providing improved numerical stability and accuracy. In an MRT-LBM formulation, the density distribution functions, $|f_i(\mathbf{x},t)\rangle$, are transformed into moment space, $|m_i(\mathbf{x},t)\rangle$, relaxed towards equilibrium, and then transformed back to velocity space. The conversion from velocity to moment space can be written as,

$$|m_i(\mathbf{x},t)\rangle = \mathbf{M}\,|f_i(\mathbf{x},t)\rangle\,, \tag{2.22}$$

in which $\mathbf{M}$ is the transformation matrix. For the D3Q15 lattice which is used in Chapter 3, $\mathbf{M}$ is written as,

$$\mathbf{M} = \begin{bmatrix}
1 & 1 & 1 & 1 & 1 & 1 & 1 & 1 & 1 & 1 & 1 & 1 & 1 & 1 & 1 \\
-2 & -1 & -1 & -1 & -1 & -1 & -1 & 1 & 1 & 1 & 1 & 1 & 1 & 1 & 1 \\
16 & -4 & -4 & -4 & -4 & -4 & -4 & 1 & 1 & 1 & 1 & 1 & 1 & 1 & 1 \\
0 & 1 & -1 & 0 & 0 & 0 & 0 & 1 & -1 & 1 & -1 & 1 & -1 & 1 & -1 \\
0 & -4 & 4 & 0 & 0 & 0 & 0 & 1 & -1 & 1 & -1 & 1 & -1 & 1 & -1 \\
0 & 0 & 0 & 1 & -1 & 0 & 0 & 1 & -1 & 1 & -1 & -1 & 1 & -1 & 1 \\
0 & 0 & 0 & -4 & 4 & 0 & 0 & 1 & -1 & 1 & -1 & -1 & 1 & -1 & 1 \\
0 & 0 & 0 & 0 & 0 & 1 & -1 & 1 & -1 & -1 & 1 & 1 & -1 & -1 & 1 \\
0 & 0 & 0 & 0 & 0 & -4 & 4 & 1 & -1 & -1 & 1 & 1 & -1 & -1 & 1 \\
0 & 2 & 2 & -1 & -1 & -1 & -1 & 0 & 0 & 0 & 0 & 0 & 0 & 0 & 0 \\
0 & 0 & 0 & 1 & 1 & -1 & -1 & 0 & 0 & 0 & 0 & 0 & 0 & 0 & 0 \\
0 & 0 & 0 & 0 & 0 & 0 & 0 & 1 & 1 & 1 & 1 & -1 & -1 & -1 & -1 \\
0 & 0 & 0 & 0 & 0 & 0 & 0 & 1 & 1 & -1 & -1 & -1 & -1 & 1 & 1 \\
0 & 0 & 0 & 0 & 0 & 0 & 0 & 1 & 1 & -1 & -1 & 1 & 1 & -1 & -1 \\
0 & 0 & 0 & 0 & 0 & 0 & 0 & 1 & -1 & -1 & 1 & -1 & 1 & 1 & -1
\end{bmatrix}. \tag{2.23}$$

and $|m_i(\mathbf{x},t)\rangle$ is the vector of moments,

$$|m_i(\mathbf{x},t)\rangle = \{\rho, e, \varepsilon, j_x, q_x, j_y, q_y, j_z, q_z, p_{xx}, p_{ww}, p_{xy}, p_{yz}, p_{xz}, m_{xyz}\}\,. \tag{2.24}$$

In reference to Eq. (2.2), the MRT collision operator can be written as,

$$\Omega_i^{MRT} = -\mathbf{M}^{-1}\mathbf{S}\left[|m_i(\mathbf{x},t)\rangle - \left|m_i^{eq}(\mathbf{x},t)\right\rangle\right], \tag{2.25}$$

where $\left|m_i^{eq}(\mathbf{x},t)\right\rangle$ is the vector of equilibrium moments and $\mathbf{S}$ is a diagonal matrix of relaxation times. The components of $\mathbf{S}$ can be chosen in a number of different ways, and used to tune model performance against stability and accuracy criteria. For example, in the studies presented in Ref. [90] where the D3Q15 lattice was used, $\mathbf{S}$ was defined as,

$$\mathbf{S} = diag\,(0, s_1, s_2, 0, s_4, 0, s_4, 0, s_4, s_9, s_9, s_{11}, s_{11}, s_{11}, s_{14})\,, \tag{2.26}$$

in which the relaxation parameters were $s_1 = 1.6$, $s_2 = 1.2$, $s_4 = 1.6$ and $s_{14} = 1.6$. s_9 and s_{11} were related to the kinetic viscosity, ν, and were calculated as,

$$\nu = \frac{1}{3}\left(\frac{1}{s_9} - \frac{1}{2}\right) = \frac{1}{3}\left(\frac{1}{s_{11}} - \frac{1}{2}\right). \tag{2.27}$$

In another study published by Pan et al. [4] where a D3Q19 lattice was utilised, $\mathbf{S}$ was defined as,

$$\mathbf{S} = diag\left(0, s_e, s_\varepsilon, 0, s_q, 0, s_q, 0, s_q, s_\nu, s_\pi, s_\nu, s_\pi, s_\nu, s_\nu, s_\nu, s_m, s_m, s_m\right). \tag{2.28}$$

Two sets of relaxation parameters were listed and studied in Ref. [4], which were defined as,

$$s_\nu = \frac{1}{\tau} = \frac{2}{(6\nu+1)}, s_e = s_\varepsilon = s_\pi = s_m = s_q = 8\left(\frac{2-s_\nu}{8-s_\nu}\right), \tag{2.29a}$$

for Set A and,

$$s_e = s_\varepsilon = s_\pi = s_\nu = \frac{1}{\tau}, s_m = s_q = 8\left(\frac{2-s_\nu}{8-s_\nu}\right), \tag{2.29b}$$

for Set B. Detailed investigation and comparison of the two sets of relaxation parameters can be found in Ref. [4].

The Two-Relaxation-Time Model

In this work, a two-relaxation-time (TRT) version [91] of the MRT collision operator is employed, in which two separate eigenvalues, λ_e and λ_o, of the linearised collision operator are applied to the symmetric (even) and anti-symmetric (odd) components of $\left|m_i^{neq}(\mathbf{x},t)\right\rangle$. In this work, these are chosen as,

$$\lambda_e = s_\nu = \frac{1}{\tau}, \tag{2.30a}$$

and,

$$\lambda_o = s_m = 8\left(\frac{2-s_\nu}{8-s_\nu}\right), \tag{2.30b}$$

which results in the collision matrix being defined as,

$$\mathbf{S} = diag\left(0, s_\nu, s_\nu, 0, s_m, 0, s_m, 0, s_m, s_\nu, s_\nu, s_\nu, s_\nu, s_\nu, s_\nu, s_\nu, s_m, s_m, s_m\right). \tag{2.31}$$

The relationship between the relaxation rates in the TRT collision operator has been studied extensively [91, 94, 95] and linked by what is often referred to as the *magic parameter*,

$$\Lambda = \left(\frac{1}{s_\nu} - \frac{1}{2}\right)\left(\frac{1}{s_m} - \frac{1}{2}\right). \tag{2.32}$$

Several values of Λ, including $1/4$, $3/16$, $1/6$, and $1/12$, have been proposed and tested (see [91] and [95] for further details). Here Λ is chosen as $3/16$ to satisfy requirements on numerical stability and the accurate

reproduction of the no-slip boundary location for flow around particles [95]. This also ensures consistency with Eqs. (2.30a) and (2.30b).

To simplify the computation, one can decompose any pair of density distribution functions with opposite velocities (which is referred to as a *link*) into its symmetric (even) and anti-symmetric (odd) components, which is expressed as,

$$f_{even} = \frac{1}{2}\left(f_i + f_{-i}\right), f_{even}^{eq} = \frac{1}{2}\left(f_i^{eq} + f_{-i}^{eq}\right), \tag{2.33}$$

and,

$$f_{odd} = \frac{1}{2}\left(f_i - f_{-i}\right), f_{odd}^{eq} = \frac{1}{2}\left(f_i^{eq} - f_{-i}^{eq}\right), \tag{2.34}$$

where $-i$ denotes the opposite direction of i. For the rest density distribution function, $f_{0even} = f_0$ and $f_{0odd} = 0$. Hence, the TRT collision operator can be written as,

$$\Omega_i^{TRT} = -s_\nu\left(f_{even} - f_{even}^{eq}\right) - s_m\left(f_{odd} - f_{odd}^{eq}\right). \tag{2.35}$$

Without transforming the density distribution functions into the momentum space, the TRT collision operator costs similar computational expense to the BGK model, while maintaining an improved accuracy and numerical stability.

2.1.4 Forcing Terms in the LBM Formulation

In most of the studies presented in this thesis, the fluid is driven by the application of a body force, $\mathbf{G}$. To add the forcing term to the LBE, Buick and Greated [96] proposed four methods based on the principle of momentum increment rather than velocity modification.

In Method 1, the equilibrium density distribution functions are modified by adding the gravitational potential, $-\rho \bigtriangledown \phi$. It was stated that this method was only applicable when the density gradient was sufficiently small.

When applying a body force to the fluid, a momentum increment, $-\bigtriangledown(\rho\mathbf{u}) = \mathbf{G}$ is generated at each timestep. Hence, in Method 2 the resultant fluid momentum at the current timestep is calculated as the average of the values before and after collision,

$$\rho\mathbf{v} = \rho\mathbf{u} + \frac{1}{2}\mathbf{G}. \tag{2.36}$$

With the use of Method 2, the equilibrium density distribution functions are calculated using an *equilibrium velocity*, $\mathbf{u}^*$, which is calculated as,

$$\rho\mathbf{u}^* = \rho\mathbf{u} + \tau\mathbf{G}. \tag{2.37}$$

It is obvious that this method relaxes the density distribution functions towards the equilibrium that has included the momentum increment induced by the body force.

In Method 3, an additional forcing term is incorporated in the collision operator, which is then written as,

$$\Omega_i^{'} = \Omega_i + \frac{D}{bc^2}\mathbf{G}\cdot\mathbf{e_i}, \tag{2.38}$$

where D is the dimension of the case and b is the number of discrete velocities.

In Method 4, the equilibrium density distribution functions are again calculated using the *equilibrium velocity*, $\mathbf{u}^*$, but in a different form, which is written as,

$$\mathbf{u}^* = \mathbf{u} + \frac{\mathbf{G}}{2\rho}, \tag{2.39}$$

and the LBE is modified by adding an additional forcing term,

$$f_i(\mathbf{x} + \mathbf{e_i}\Delta t, t + \Delta t) - f_i(\mathbf{x}, t) = \Omega_i + \frac{2\tau - 1}{2\tau}\frac{D}{bc^2}\mathbf{G} \cdot \mathbf{e_i}. \tag{2.40}$$

It can be observed that Method 4 is a combination of Method 2 and Method 3 with the coefficients chosen to ensure the correct form of the Navier-Stokes equations in the continuum limit.

It should be noted that Buick and Greated proposed these methods for the purpose of considering gravity in the simulations. Similar to Eq. (2.8), it is required that $\mathbf{G}z << c_s^2$, in which z is the extent of the simulation in the direction of $\mathbf{G}$. In their study, Method 1 was found to be able to simulate Poiseuille flow. However, it performed less well than the other three with the presence of a density gradient, even when the gradient was considerably small. Within the compressibility limit, Methods 2, 3 and 4 exhibited good agreement with theory when the non-linear term of the Navier-Stokes equations was zero. When the non-linear term became non-zero, Method 4 was an optimal choice over the other two methods.

In another study, Strack and Cook [62] proposed a similar method to Method 3, in which an additional term is added to the post-collision operator, $f_i^+(\mathbf{x}, t)$. Here $f_i^{++}(\mathbf{x}, t)$ is used to represent the post-processed, post-collision operator where the forcing term is incorporated. Hence $f_i^{++}(\mathbf{x}, t)$ is calculated as,

$$f_i^{++}(\mathbf{x}, t) = f_i^+(\mathbf{x}, t) + A\mathbf{G}\mathbf{e_i}, \tag{2.41}$$

where A is a coefficient calculated as,

$$A = \frac{1}{Kc^2}, \tag{2.42}$$

in which $K = 6$ for the D2Q9 model and $K = 10$ for the D3Q15 model.

With the appearance of the forcing term, Eq. (2.3) is modified as,

$$fi(\mathbf{x} + \mathbf{e_i}\Delta t, t + \Delta t) = f_i^{++}(\mathbf{x}, t), \tag{2.43}$$

which describes the streaming process of the LBM.

2.1.5 Numerical Accuracy and Stability of the LBM

As stated in Section 2.1.1, to ensure reasonable numerical accuracy, it is required that $Ma << 1$. Studies [97] have shown that second order accuracy can be obtained in space and time by the LBM at low Mach numbers. This means that, when keeping the kinetic viscosity, ν (as shown in Eq. (2.9)) as a constant, the error decreases quadratically with Δx. On the other hand, the error will also decrease quadratically with Δt, if Δx remains a constant.

In the LBM, the H-theorem cannot be guaranteed during the simulation. Therefore, the LBM is not unconditionally stable. Qian et al. [98] presented detailed stability analyses for the D2Q9 and D3Q15 models. In their study, the mean flow velocity was required to be below a maximum value which was a function of several parameters including c_s, τ and wave number of perturbations, to obtain numerical stability.

2.2 The Discrete Element Method

The DEM was originally proposed by Cundall and Strack [54] to simulate the mechanical behaviour of discontinuous media such as rock. In its classical form, a discrete system is considered as an assembly of distinct elements which are treated as rigid bodies. The mechanical interaction of the discrete elements is characterised by their small overlap and resultant contact forces (i.e. soft contact model).

2.2.1 Introduction

For each discrete element, the governing equations for translational and rotational movements are written as,

$$m\ddot{\mathbf{x}} + C\dot{\mathbf{x}} = \mathbf{F}_c + \mathbf{F}_f + m\mathbf{g}, \tag{2.44}$$

$$J\ddot{\theta} = \mathbf{T}_c + \mathbf{T}_f, \tag{2.45}$$

respectively, where m and J are the mass and moment of inertia of the particle, and C is a viscous damping term. The terms $\mathbf{F}$ and $\mathbf{T}$ denote the forces and torques acting on the particle, respectively, for both hydrodynamic fluid-particle interactions, $[\cdot]_f$, and mechanical particle-particle interactions, $[\cdot]_c$. Other forces, such as those arising from electrostatic [99] and electromagnetic interactions [100], can be included in a similar manner.

During each timestep in the DEM, a global contact detection is carried out to generate a list of potential interactions for every particle. Each contact pair (see Fig. 2.4) is then checked for overlap and, if found to be in contact, locally resolved for normal and tangential forces according to the contact model and interaction law employed. Following the calculation and summation of all forces and torques present, the kinematic properties of the particles (i.e. acceleration, velocity, and location) are updated via Eqs. (2.44) and (2.45).

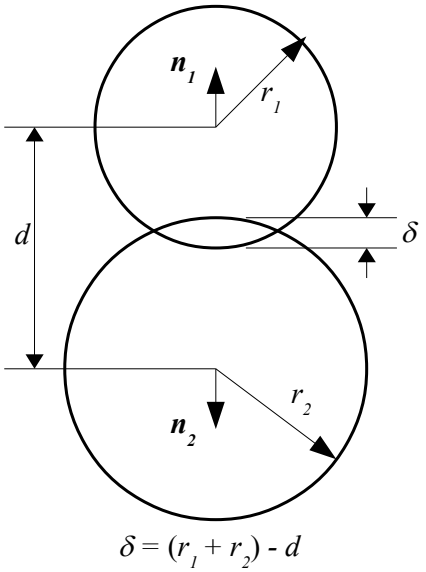

Figure 2.4: A contact pair of two circular elements in the DEM [3].

Critical to the implementation of the DEM is timestep selection. To ensure contact stability, Δt_{DEM} is typically required to be no greater than a critical value, Δt_{cr}, which is based on the Courant-Friedrichs-Levy

(CFL) condition [101] given that an explicit central difference integration scheme is employed to solve the dynamic DEM equations. For a dynamic DEM system where the linear contact model is applied, the critical timestep is expressed as,

$$\Delta t_{DEM} \leq \Delta t_{cr} = 2\lambda \sqrt{\frac{m}{k_n}} \left(\sqrt{1+\zeta^2} - \zeta \right), \tag{2.46}$$

where ζ is the critical damping coefficient and λ is a scaling parameter. On its own, the CFL constraint is often insufficient to maintain stability and so it is suggested that λ is selected within the range of 0.1 to 0.3 [25].

2.2.2 Contact Models and Interaction Laws

In its most simple form, the normal contact force, F_n between two particles can be described using a linear model,

$$F_n = k_n \delta, \tag{2.47}$$

where k_n is the normal contact stiffness and δ is the overlap of particle boundaries. For the elastic contact of spheres in 3D, a Hertz contact model can be used,

$$F_n = \frac{4E^* \sqrt{R^*}}{3} \delta^{2/3} = \frac{4E^*}{3R^*} a^3, \tag{2.48}$$

where E^* and R^* are the effective Young's modulus and effective radius, respectively, and a is defined as the contact radius,

$$a = \sqrt{R^* \delta}\,. \tag{2.49}$$

Further details of the Hertz model, along with a discussion of tangential force resolution, can be found in the work of Han and collaborators [102, 103].

2.3 The Characterisation of Fluid-Solid Boundary Conditions

Boundary conditions and initial conditions are essential for fluid modelling as they constrain the solution of the flow. Implementation of boundary conditions in the LBM is an important task owing to the fact that one has to translate given information from macroscopic variables to density distribution functions, f_i, which is the primary variable in the LBM.

2.3.1 The Bounce-Back Method

At the macroscopic scale, the interaction between fluid and particles should obey the *no-slip* boundary condition. In this situation, the fluid adjacent to the particle boundary has the same velocity as the boundary. For static particles and walls, this can be well-approximated in the LBM by using the simple bounce-back scheme (SBB), which is expressed as,

$$f_{-i}(\mathbf{x}, t+\Delta t) = f_i(\mathbf{x}, t), \tag{2.50}$$

where $-i$ denotes the opposite direction of i. Fig. 2.5 shows the schematic diagram of the bounce-back boundary condition in a 2D case. To ensure the *no-slip* effect, no tangential velocity exists along the fluid-solid interface.

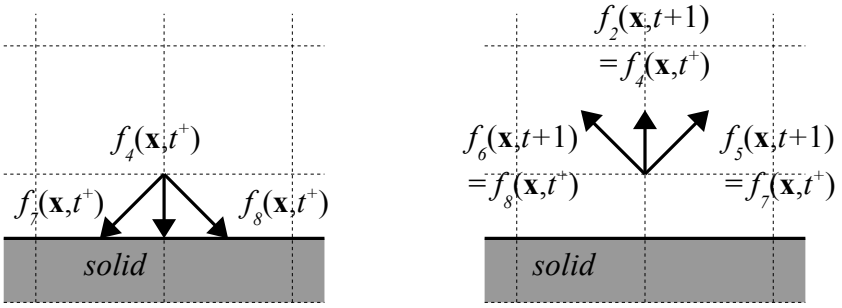

Figure 2.5: A schematic diagram of the bounce-back boundary condition at time t (left) and time $t+1$ (right). Remake from Fig. 2.4 in [3].

In some cases, the effective hydrodynamic boundary is located halfway between the solid boundary node and its most adjacent fluid node. More generally, however, the exact location of the boundary depends on the outline of the solid obstacle and the computational viscosity. The use of SBB can only achieve second order convergence when the hydrodynamic boundary is located exactly halfway between the fluid and solid nodes (e.g. flow between straight walls that are aligned with the underlying lattice). Otherwise the convergence of the scheme is only first order [53, 104].

2.3.2 The Modified Bounce-Back Methods

To characterise the boundary condition between the fluid and a moving particle, Ladd [105] proposed a modified bounce-back boundary condition, namely the link bounce-back method (shown in Fig. 2.6), to accommodate the movement of the particle. This method is based on the momentum exchange between the fluid and solid nodes. By assuming the fluid fills up the entire inner space of the particle, both nodes on the either side of the solid boundary are treated in the same manner, which simplified the computation.

For a given link between the fluid and solid nodes, the link bounce-back rule is governed by,

$$f_{-i}(\mathbf{x},t+\Delta t) = f_i(\mathbf{x},t) - \alpha_i \mathbf{e_i}\cdot\mathbf{v_b}, \tag{2.51}$$

where $\alpha_i = 6\omega_i\rho/c^2$. the velocity of the middle point of the link, $\mathbf{v_b}$, is calculated by,

$$\mathbf{v_b} = \mathbf{v_c} + \omega\times\mathbf{r_c}, \tag{2.52}$$

in which $\mathbf{v_c}$ and ω are, respectively, the translational and angular velocities of the moving particle, $\mathbf{r_c}$ is the distance from the centre of the particle to the middle of the link.

The hydrodynamic force and torque acting on the solid particle from the given link can be calculated by,

$$\mathbf{F_i} = 2\mathbf{e_i}\left[f_i(\mathbf{x},t) - \alpha_i\mathbf{e_i}\cdot\mathbf{v_b}\right]/\Delta t, \tag{2.53}$$

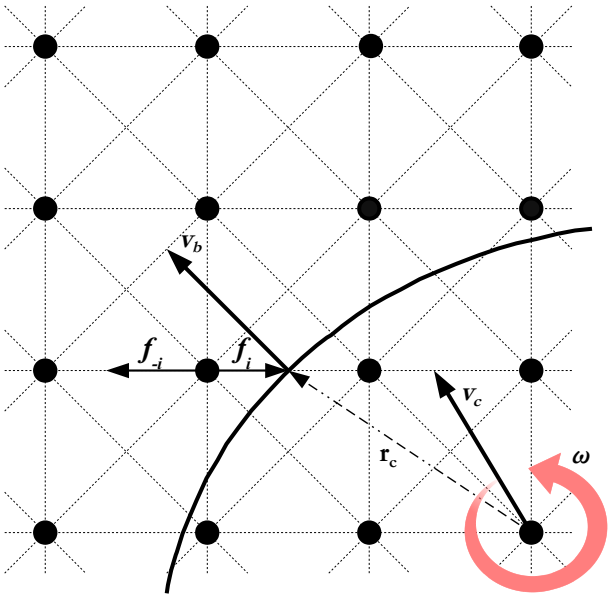

Figure 2.6: A schematic diagram of the link bounce-back boundary condition.

$$\mathbf{T_i} = \mathbf{r_c} \times \mathbf{F_i}. \tag{2.54}$$

Summing all the components of the hydrodynamic forces and torques from every link, the total hydrodynamic impact on the solid particle can be computed as,

$$\mathbf{F_t} = \sum_i \mathbf{F_i}, \tag{2.55}$$

$$\mathbf{T_t} = \sum_i \mathbf{T_i}. \tag{2.56}$$

However, the link bounce-back method has severe drawbacks which are mainly revealed in two aspects. First, mass transfer is allowed through the solid boundary which may have effects on the inertia, thus affecting the numerical accuracy [106]. Second, the movement of the particle would produce continuous phase change in the boundary nodes in an *on-off* pattern, which could induce severe oscillation to the resultant forces [107].

To more accurately describe solid boundaries on the underlying lattice, several other improved forms of fluid-solid boundary conditions have been developed. These include the linearly interpolated bounce-back scheme (LIBB), the quadratically interpolated bounce-back scheme [108] (QIBB), and multi-reflection [109] (MR) bounce-back. However, the interpolated schemes are more complicated to implement than SBB as they require information from more than one additional fluid node between the two neighbouring solid nodes. To reduce the number of the additional fluid nodes required in interpolated boundary conditions, Chun and Ladd [88] proposed an equilibrium interpolated (EI) scheme in which the interpolation is applied to the equilibrium distribution functions only. The EI scheme was found to be second-order accurate and viscosity-independent with only one additional fluid node needed.

Studies [4, 88, 110] have shown that, of the boundary implementations discussed here, the MR scheme is the most accurate and independent of viscosity. The LIBB and the QIBB schemes have a stronger dependence

on viscosity than the SBB scheme. Moreover, the SBB scheme and the later-proposed modified bounce-back scheme [105, 111] are not able to accurately compute the hydrodynamic force on the interface, especially when simulating moving particles. In this scenario the computed force and torque may experience fluctuation as the boundary nodes are remapped in a discrete manner at each timestep [107].

2.3.3 The Partially Saturated Method

To solve the problem of fluctuating forces, Noble and Torczynski [56] proposed a boundary condition for partially saturated computational cells, which is often referred to as the partially saturated method (PSM). In this approach, the LBE is modified so that nodes in the vicinity of the hydrodynamic boundary are processed using an interpolated combination of conventional relaxation and fluid-solid momentum exchange. This facilitates nodes either solely or partially covered by the solid obstacle to be treated in the same manner.

When using the PSM, the MRT-LBE is modified as,

$$|f_i(\mathbf{x}+\mathbf{e}_i\Delta t, t+\Delta t)\rangle - |f_i(\mathbf{x},t)\rangle = -\mathbf{M}^{-1}\mathbf{S}\mathbf{M}(1-\beta)(|f_i(\mathbf{x},t)\rangle - \left|f_i^{eq}(\mathbf{x},t)\right\rangle) + \beta\Omega_i^m, \tag{2.57}$$

where β is a solid weighting function dependent on the local solid volume fraction, γ, and Ω_i^m is the PSM collision operator that accounts for the fluid-solid interactions in the local nodal cell. In the original work of Noble and Torczynski [56], two forms of Ω_i^m were introduced. The first was based on the bounce-back of the non-equilibrium part of the density distribution function and defined as,

$$\Omega_i^m = f_{-i}(\mathbf{x},t) - f_i(\mathbf{x},t) + f_i^{eq}(\rho,\mathbf{u}_\mathbf{s}) - f_{-i}^{eq}(\rho,\mathbf{u}), \tag{2.58}$$

where $\mathbf{u}_\mathbf{s}$ denotes the velocity of the solid node in the subsequent timestep. The second form of Ω_i^m is computed from the superposition of the equilibrium density distribution functions at the solid boundary and a term of the deviation of the current density distribution function from its equilibrium. This is known as the superposition collision operator and given by,

$$\Omega_i^m = f_i^{eq}(\rho,\mathbf{u}_\mathbf{s}) - f_i(\mathbf{x},t) + \left(1-\frac{\Delta t}{\tau}\right)\left[f_i(\mathbf{x},t) - f_i^{eq}(\rho,\mathbf{u})\right]. \tag{2.59}$$

Holdych [112] modified the non-equilibrium bounce-back operator in Eq. (2.58) by replacing the fluid density equilibrium term in the reflected direction by the solid equilibrium, resulting in,

$$\Omega_i^m = f_{-i}(\mathbf{x},t) - f_i(\mathbf{x},t) + f_i^{eq}(\rho,\mathbf{u}_\mathbf{s}) - f_{-i}^{eq}(\rho,\mathbf{u}_\mathbf{s}). \tag{2.60}$$

In its simplest form, the solid weighting function is calculated directly as the solid coverage ratio of the cell,

$$\beta = \gamma, \tag{2.61}$$

which is illustrated in Fig. 2.7.

In testing, the superposition collision operator was found to perform well with Eq. (2.61), while the non-equilibrium reflection forms of Ω_i^m require a more complex τ-dependent solid weighting function. One form proposed by Noble and Torczynski [56],

$$\beta = \frac{\gamma(\tau-0.5)}{(1-\gamma)+(\tau-0.5)}, \tag{2.62}$$

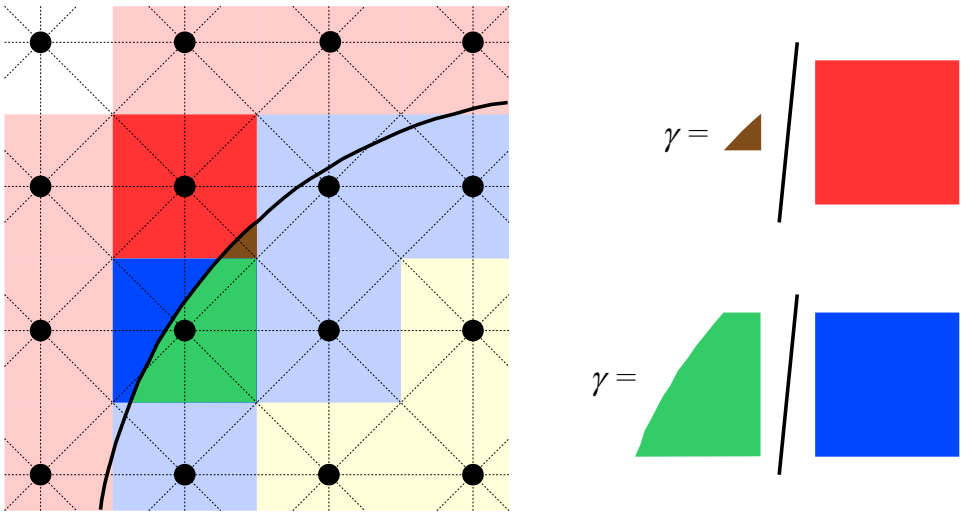

Figure 2.7: Evaluation of the solid coverage ratio, γ, in the partially saturated method. Remake from Fig. 3.4(a) in [3].

was empirically designed to minimise the viscosity-dependent slip which is intrinsic to boundary conditions based on bounce-back.

To complete the definition of the PSM, the total hydrodynamic force and torque acting on the solid obstacle can be obtained by,

$$\mathbf{F}_f = c\Delta x \left[\sum_n \left(\beta_n \sum_i \Omega_i^m \mathbf{e}_i \right) \right], \tag{2.63}$$

$$\mathbf{T}_f = c\Delta x^2 \left[\sum_n (x_n - x_c) \times \left(\beta_n \sum_i \Omega_i^m \mathbf{e}_i \right) \right]. \tag{2.64}$$

It is worth mentioning that when no solid obstacle is present in the lattice cell, the PSM for fluid–solid interaction can recover the standard LBE with $\gamma = 0$. In cases where multiple solid obstacles are mapped to the same LBM cell, a sub-grid-scale condition is applied [113]. This can occur when discrete elements approach or engage in contact, with the latter allowing slight overlap of boundaries. Consequently Eq. (2.57) is modified and expressed as,

$$|f_i(\mathbf{x}+\mathbf{e}_i\Delta t, t+\Delta t)\rangle - |f_i(\mathbf{x},t)\rangle = -\mathbf{M}^{-1}\mathbf{S}\mathbf{M}(1-\sum_d \beta_d)(|f_i(\mathbf{x},t)\rangle - |f_i^{eq}(\mathbf{x},t)\rangle) + \sum_d \beta_d \Omega_i^m, \tag{2.65}$$

where β_d is the solid weighting function for each obstacle, d, depending on their local solid fractions, respectively. Meanwhile, u_s in the PSM collision operator is calculated by the weighted average of the obstacle velocities.

2.4 Summary

This chapter has presented an introduction to the numerical methodologies used in this thesis, i.e. the coupled LBM-DEM framework using the PSM. As an ideal alternative approach for the conventional CFD methods to model fluid flow, the LBM is suitable for particle suspension modelling due to its high computational efficiency

and straight-forward mapping of solid obstacles. The application of a Cartesian grid ensures a reasonable computational expense without requiring the remeshing process or a moving mesh, which occur in many other methods such as the finite element method (FEM) and the finite volume method (FVM). In addition, the implementation of the TRT collision operator is expected to improve the computational accuracy and stability over the most commonly used BGK collision operator, at similar computational costs. Meanwhile, the DEM is an effective approach to the modelling of discrete solid elements, particularly for the large amount of solid particles in this project. The PSM allows for an accurate characterisation of solid boundaries on the LBM grid, which makes the coupling of the LBM and the DEM more efficient. All these features make the coupled LBM-DEM an ideal approach to study fluid-particle interaction in hydraulic fractures.

Chapter 3 - Improved Coupling of the LBM-DEM Using the PSM

[1] **D. Wang**, C. R. Leonardi, and S. M. Aminossadati, Improved coupling of time integration and hydrodynamic interaction in particle suspensions using the lattice Boltzmann and discrete element methods, *Computers & Mathematics with Applications*, 75, 7, 2018.

Significant portions of this chapter have been adapted from Sections 1-4 of the above paper. As the lead author of this paper, I was responsible for significant portions of the following aspects:

- literature review presented in Section 1,
- model development discussed in Section 4,
- analysis of results presented in Section 4,
- drafting of the manuscript and its review.

The listed co-authors provided contributions towards the final review of the paper and suggestions as well as towards developing and improving the discussed results both in terms of analyses conducted and their presentation.

Estimated Contributions by Candidate	
Conception and design	70%
Analysis and interpretation	85%
Drafting and production	70%

Chapter 3

Improved Coupling of the LBM-DEM Using the PSM

The viscosity-dependence of boundary conditions in the LBM has attracted significant interest in literature. Past research has shown that the drag, and consequently permeability, predictions of the LBM exhibit viscosity-dependence when used with certain boundary conditions such as bounce-back or interpolated bounce-back, and this is most pronounced when the BGK collision operator is employed. Numerous boundary conditions (as introduced in Section 2.3) have been proposed to reduce this viscosity-dependence, many of which, however, require additional computational cost.

In the context of the LBM-DEM numerical framework, the issue of viscosity-dependence is also related to explicit time integration as the two methods are run in parallel. In an ideal situation, both methods would propagate with an identical timestep size. Otherwise, a sub-cyling technique is required to allow several DEM iterations to be performed within one LBM timestep. However, the number of sub-cycles has certain constraints to avoid fluctuation of the hydrodynamic interactions. Under these circumstances, it is of great importance that the parameters that determine the LBM timestep have as little impact as possible on numerical accuracy.

As a potential solution to fluid-solid boundary conditions, the viscosity-dependence of the TRT-PSM scheme has to date remained unexplored. Therefore, an investigation on the viscosity-dependence of the TRT-PSM formulations will firstly be demonstrated in this chapter, using flow past a periodic array of spheres as the benchmark problem. A modified solid weighting function is then proposed to address the viscosity-dependence exhibited by the TRT-PSM scheme. Further studies using other flow configurations will also be presented to investigate the performance of the improved LBM-DEM coupling approach.

3.1 Computational Issues of the LBM-DEM Coupling

A range of collision operators (see Section 2.1.3) and boundary conditions (see Section 2.3) are now available for the formulation of an LBM model. Within the context of simulating particle suspensions, the single-relaxation-time BGK collision operator [87] along with a simple bounce-back scheme (SBB) remains the most popular combination. However, several shortcomings of BGK-LBM formulations have been widely reported in the literature, including poor stability and accuracy, particularly at low viscosities or high Reynolds number. Another

significant computational issue is the viscosity-dependence of boundary conditions, which highlights the impact of the computational viscosity, ν, on simulation results. It was reported by Zou and He [114] that when using SBB for hydrodynamic boundaries, the exact location of the no-slip interface becomes a function of the relaxation parameter (i.e. computational viscosity), and as such cannot be interpreted as halfway between a fluid and boundary node. The use of a MRT collision operator [90] can overcome some of the deficiencies of BGK-LBM formulations. However, the exact location of the no-slip boundary still depends on the computational viscosity [104]. Consequently, the viscosity-dependence, which can further be translated to a time stepping issue for the LBM-DEM coupling framework, has severely influenced the robustness and applicability of the model.

3.1.1 Cell Decomposition Technique in the PSM

From the introduction of the PSM in Section 2.3.3, it can be concluded that the PSM only requires local computation to enforce the hydrodynamic coupling of the fluid and solid. This maintains the inherent locality of the LBM. With the present implementation of the LBM, it is possible to incorporate complex obstacle geometries and a large number of particles in simulations, which is ideal for hydraulic fracturing modelling.

In the context of dense particle suspensions, particularly for particles of various sizes, the choice of lattice spacing, Δx, can cause conspicuous difference in the numerical accuracy. As shown in Fig. 3.1, Δx should be chosen according to the diameter of the smallest particle. Based on the testing results in this study, it is suggested that at least four lattice spacings are required to be covered by the particle diameter to ensure a reasonable accuracy. However, in the cases where the difference in particle size is significant, the computational cost will be considerably high.

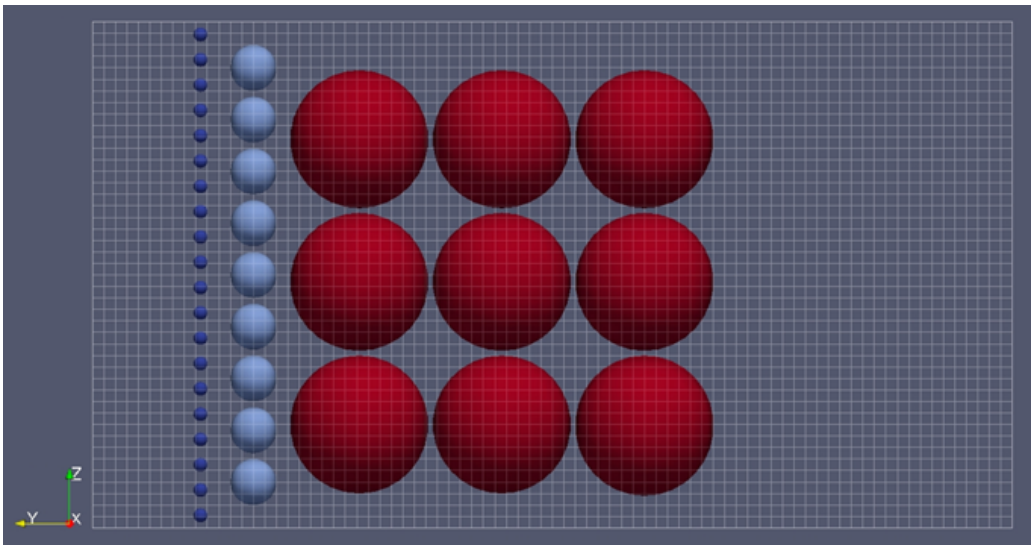

Figure 3.1: Mapping of particles of different sizes to the LBM grid.

To tackle this issue, a cell decomposition technique, which is shown in Fig. 3.2 is applied in this project for the calculation of solid coverage ratio. In this technique, the nodal cell is decomposed into $n_{subcell}^2$ identical subcells such that the side length of a subcell $\Delta x_{subcell} = \Delta x / n_{subcell}$.

It is notable that this technique is only required to be applied to the fluid-solid boundary cells where solid is present. It can be time consuming when $n_{subcell}$ increases for the purpose of a more accurate solid coverage evaluation. However, the computational cost is acceptable when compared to the implementation of a finer grid

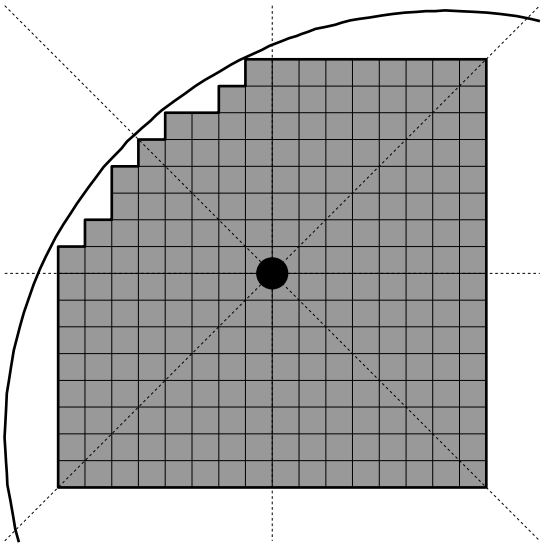

Figure 3.2: Cell decomposition technique for calculating solid coverage of a cell.

where the number of nodes increases quadratically with the lattice. In most of the studies presented in this thesis, $n_{subcell}$ is set to three to obtain accuracy while keeping the computational cost within a reasonable range.

3.1.2 Viscosity-Dependence of the LBM

Fig. 3.3 plots the results obtained by Pan et al. [4], who found that when simulating fluid flow through a porous medium, the calculated permeability, which is a physical property of the medium itself, changed with the computational viscosity. This represents a significant issue for a range of LBM applications, beyond porous media and suspension flows. Although it was also found that viscosity-dependence was reduced by using an MRT collision operator, the accuracy of the permeability predictions was dependent on the use of higher-order boundary conditions such as quadratically-interpolated (QIBB) or multi-reflection (MR) bounce-back. Other improvements [88, 108, 109] have been made to better describe fluid-solid boundaries on the underlying lattice but, like the QIBB and MR conditions, many of the improved boundary conditions require non-local computations which increase computational costs. Conversely, the use of a PSM for fluid-solid boundaries, such as that proposed by Noble and Torczynski [56], is attractive. The introduction to the LBE of the solid volume fraction in a cell improves the precision with which the no-slip boundary is represented. Validation in the literature [57, 62, 115] has shown that the technique is also capable of accurately computing the momentum exchange between fluids and solids using only local computations.

It is worthwhile to note that that Prestininzi et al. [116] recently presented an alternate interpretation of the viscosity-dependence of boundary conditions in BGK-LBM formulations. In this work, the authors show that the issue can be overcome when the Knudsen number, Kn, is kept small and constant. However, to keep Kn constant at varying relaxation parameter requires adjustment of the grid resolution, which is impractical in most engineering simulations (e.g. fully resolving the flow through small and tortuous pore networks, or around a suspended particle) due to limitations on memory and processor time. Further, the LBM is most often employed to mimic the Navier-Stokes equations, where the Knudsen number should have no effect on the results. To account for it in such simulations would be paradoxical.

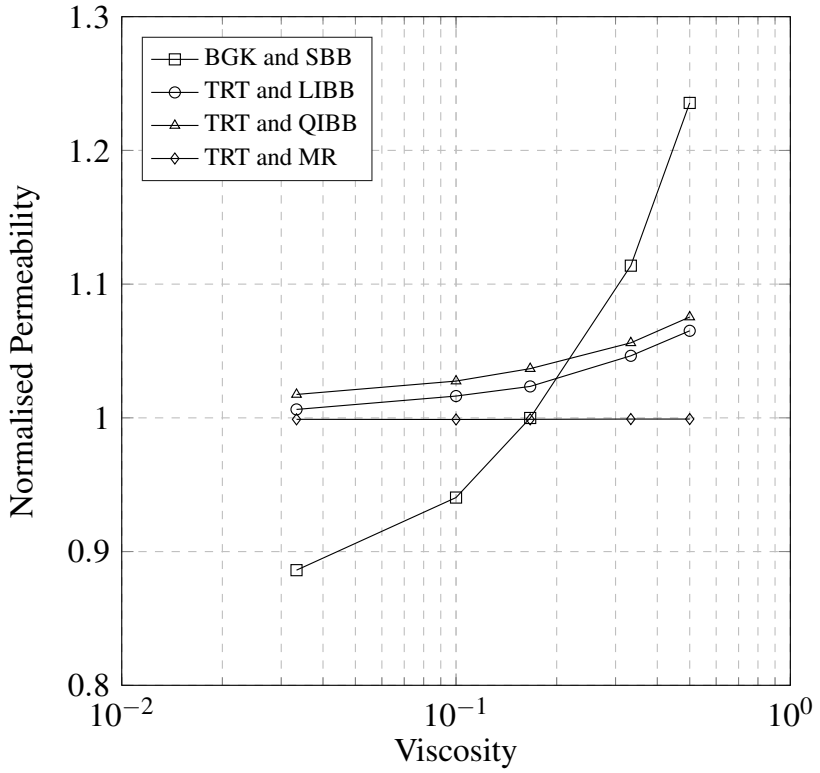

Figure 3.3: The normalised permeability, κ^*, at varying computational viscosity for flow past a body-centred-cubic array of spheres. Remake from Fig. 4a in [4].

3.1.3 Time Stepping of the LBM-DEM Coupling

Two independent timesteps are utilised in the implemented LBM-DEM framework, namely Δt_{LBM} and Δt_{DEM}. As shown in Eq. (2.10), the former is explicitly calculated as a function of τ, Δx, and ν, while Eq. (2.46) shows that the latter is limited by the material properties of the discrete element(s).

In cases where $\Delta t_{LBM} < \Delta t_{DEM}$, the simulation timestep can simply be chosen as Δt_{LBM}. This requires the DEM timestep to be conservatively reduced even further with respect to the stability limit. In this scenario the physical magnitude of both timesteps is equivalent and both algorithms evolve at the same rate per step.

Conversely, in cases where $\Delta t_{LBM} > \Delta t_{DEM}$, sub-cycling is employed to perform a number of DEM timesteps within one LBM timestep. The ratio between the two timesteps, $R_{sub} = \Delta t_{LBM}/\Delta t_{DEM}$, is integerised to calculate the number of DEM sub-cycles per LBM timestep, $n_{sub} = CEILING(R_{sub})$. Thus the new DEM timestep is calculated as,

$$\Delta t^*_{DEM} = \frac{\Delta t_{LBM}}{n_{sub}}. \tag{3.1}$$

There exists certain practical limits on the number of sub-cycles used in LBM-DEM simulations. In the implemented LBM-DEM framework, the boundary nodes and the hydrodynamic loadings of the discrete elements are kept unchanged during the sub-cycling process. Therefore, the solid boundary cannot cross more than one grid spacing before it is remapped at the next LBM timestep to avoid fluctuation in the hydrodynamic response [53, 115].

In the present work, Δx is selected as a compromise between accuracy and computational cost, while ν is prescribed by the physical properties of the fluid. In formulations where hydrodynamic drag is viscosity-

dependent the value of τ is constrained to some certain range, typically as close to one as possible. As a result, there is little scope for the adjustment of τ to modify Δt_{LBM} to more efficiently synchronise it with Δt_{DEM}. This is central to the motivation of this study, which aims to identify an LBM formulation that uses a local, viscosity-independent boundary implementation, thereby providing greater flexibility in the coupling of the two explicit schemes.

3.2 Modified Solid Weighting Function in PSM

Based on the computational issues discussed in Section 3.1, it would be beneficial to the construction of LBM-DEM models if the relaxation parameter, τ, could be used (within other constraints) as a free parameter that allows the optimal choice of the LBM timestep from the perspective of coupling to the DEM. This is not possible, however, as the choice of τ and the associated computational viscosity has implications for the precision of hydrodynamic coupling, as already discussed. Instead, τ is often prescribed a value of one when using BGK-LBM formulations with boundary conditions based on bounce-back, which minimises error but renders timestep coupling awkward. Although increasing the grid resolution can help mitigate these problems, this is not computationally efficient, especially for large-scale simulations involving millions of nodes, or more. Therefore, the aim of this work is to define a choice of LBM collision operator and boundary conditions which reduces the dependence of hydrodynamic coupling on computational viscosity, and maintains the locality of operations offered by boundary conditions based on the bounce-back principle. This will allow greater flexibility in the choice of relaxation parameter and LBM timestep, and result in more efficient coupling of time integration with the DEM.

Previous studies [88, 117] have shown that, for boundary conditions based on the bounce-back principle, the slip velocity is actually second-order with respect to τ. Therefore, a generalised form of Eq. (2.62) is proposed here in an attempt to address the $\mathscr{O}\left(\tau^2\right)$ component of the slip velocity and further reduce the viscosity-dependence of the PSM for moving boundaries,

$$\beta = \frac{\gamma \sum_b b\,(\tau - 0.5)^b}{(1-\gamma) + \sum_b b\,(\tau - 0.5)^b}. \tag{3.2}$$

This is herein referred to as the modified solid weighting function [1]. The empirical nature of the function means that the summation index, b, can be chosen to best suit the boundaries modelled. A sensitivity analysis of the free parameter, b, is presented in Section 3.3.1 to determine an optimal value for the studies included in this work. Obviously, Eq. (3.2) can be used to recover the original solid weighting function, Eq. (2.62), when $b = 1$.

3.3 Validation and Testing of the Improved LBM-DEM Framework

The coupled LBM-DEM framework with partially saturated boundaries was tested in its original form, with a TRT collision operator, and then with the modified solid weighting function proposed in Section 3.2. Accuracy and convergence results based on the flow profile and hydrodynamic forces are presented for a range of test cases. For each simulation set, a BGK collision operator case has been included for comparison with the TRT implementation.

3.3.1 Flow Past a Periodic Array of Spheres

The first test case investigated was the flow past a periodic array of spheres. This was undertaken to determine the viscosity-dependence of different combinations of PSM collision operators and solid weighting functions, when used in conjunction with a TRT collision operator. These combinations are listed as follows:

1. Non-equilibrium bounce-back collision operator (Eq. (2.58)) with the solid coverage ratio weighting function (Eq. (2.61));
2. Non-equilibrium bounce-back collision operator (Eq. (2.58)) with τ-dependent weighting function (Eq. (2.62));
3. Superposition collision operator (Eq. (2.59)) with τ-dependent weighting function (Eq. (2.62));
4. Holdych collision operator (Eq. (2.60)) with τ-dependent weighting function (Eq. (2.62)).

The model was constructed using a fully periodic cubic domain with a side length of 20. A sphere was fixed at the centre of the domain, with its radius prescribed to result in a solid volume fraction of 0.1250. This facilitated direct comparison with the results of Zick and Homsy [118]. The fluid was driven by a body force in the x-direction, and the computational Mach number was kept at a constant value of 0.001 for all test cases. For each case the relaxation parameter, τ, was prescribed and converted to kinematic fluid viscosity, ν, via Eq. (2.9).

For a simple-cubic (SC) periodic array of spheres, the drag coefficient is calculated as,

$$K = \frac{F_D}{6\pi\rho\nu r U_s}, \tag{3.3}$$

where F_D is the drag force on a single sphere, r is the sphere radius, and U_s is the superficial velocity in the domain in the flow direction. The superficial velocity in the x-direction is calculated as,

$$U_s = \frac{1}{n_x n_y n_z} \sum_{x,y,z} (1-\gamma) u_x, \tag{3.4}$$

where n_x, n_y, and n_z are the number of nodes in each dimension and u_x is the x-direction velocity.

The drag coefficient was calculated for varying relaxation parameter, τ, and compared to the reference value, $K^* = 4.292$. Fig. 3.4 plots the normalised drag coefficient, K/K^*, against the fluid viscosity for the combinations listed above. The results show that all of the PSM formulations exhibit some dependence on the computational viscosity, even after the inclusion of a TRT collision operator. This is most prominent at larger viscosities. The non-equilibrium bounce-back operator with the solid coverage ratio weighting function (i.e. Combination 1), and the superposition operator with the τ-dependent weighting function (i.e. Combination 3), both show strong dependence on viscosity. The latter is the most inaccurate across all tested values of viscosity. The performance of the non-equilibrium bounce-back operator improved when used with the τ-dependent weighting function (i.e. Combination 2), whereas the Holdych collision operator with the τ-dependent weighting function (i.e. Combination 4) also performed well. Both of these results showed that the use of a TRT collision operator could significantly reduce the viscosity-dependence of the PSM, when compared to the BGK collision operator (results included in Fig. 3.4 for comparison). Based on these findings, and the fact that it demonstrated the greatest accuracy at low viscosity, the non-equilibrium bounce-back collision operator combined with the τ-dependent weighting function (i.e. Combination 2) was chosen as the basis for the remaining simulations in this study.

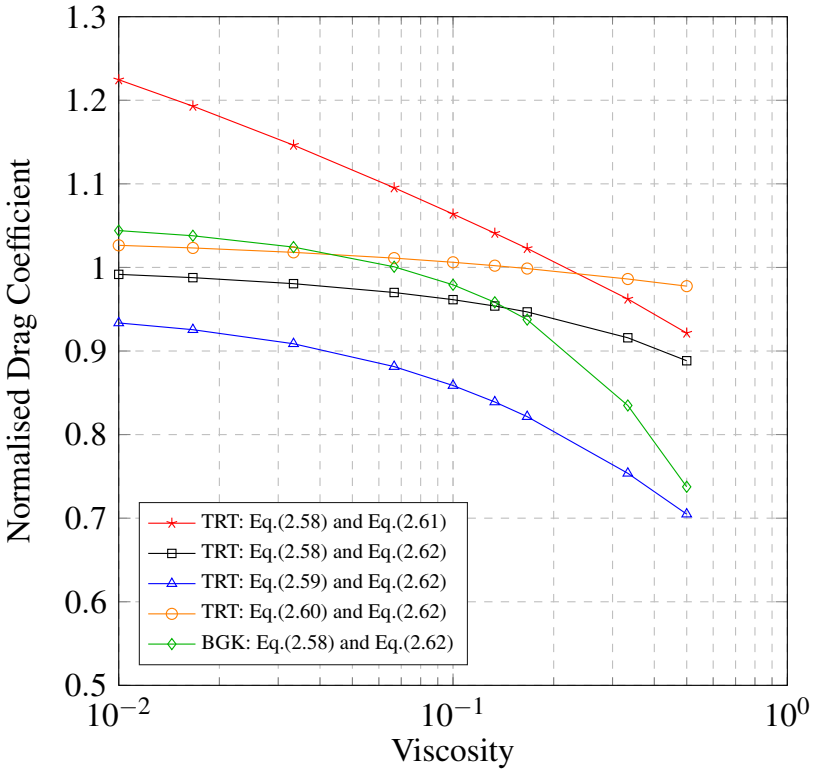

Figure 3.4: The normalised drag coefficient, K/K^*, at varying computational viscosity, ν, for the BCC model.

To test the performance of the modified solid weighting function proposed in Section 3.2, a sensitivity analysis of the summation index, b, was first undertaken. During this test, Eq. (2.58) was implemented in conjunction with Eq. (3.2) and tested using the same simple cubic (SC) array. The results are presented in Fig. 3.5(a). The results from Combination 2, which is equivalent to $b = 1$, are included for comparison. It can be seen that the modified solid weighting function has eliminated the dependence on viscosity in the range $\nu < 0.1$, which corresponds to $0.5 < \tau < 0.8$, with $b \geq 3$, and is more accurate than the original definition of the function. This result provides additional flexibility in the choice of relaxation parameter when trying to couple the timesteps of the LBM and DEM. Fig. 3.5(a) also indicates that increasing the value of b improves the accuracy and further eliminates the viscosity-dependence, which expands the range of applicable relaxation parameters. However, at least for the cases presented in this work, limited improvement was made with $b > 4$. As a result, $b = 4$ was selected as the optimal value for the remaining simulations in this study. Fig. 3.5(b) plots the modified solid weighting function at varying viscosity and $b = 4$ and contrasts it to the original solid weighting function. This highlights the greater influence of the modified solid weighting function as the computational viscosity increases.

To further test the modified solid weighting function, the spatial convergence was investigated using the same SC simulation. Fig. 3.6 graphs the normalised drag coefficient against the computational viscosity at different grid resolutions, with N representing the number of the grid spacings along each side of the cubic domain. The same data is then presented in Fig. 3.7 as the convergence of the relative error of the drag coefficient at varying relaxation parameter.

It can be seen in Fig. 3.6(a) that when the original solid weighting function is applied, increasing the grid resolution reduces the relative error but does not eliminate the viscosity-dependence. However, when

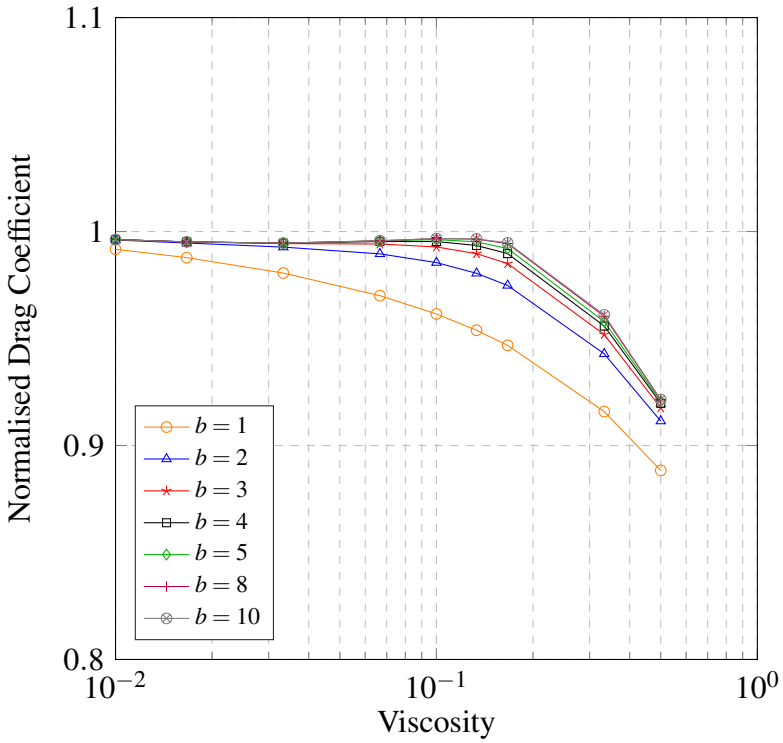

(a)

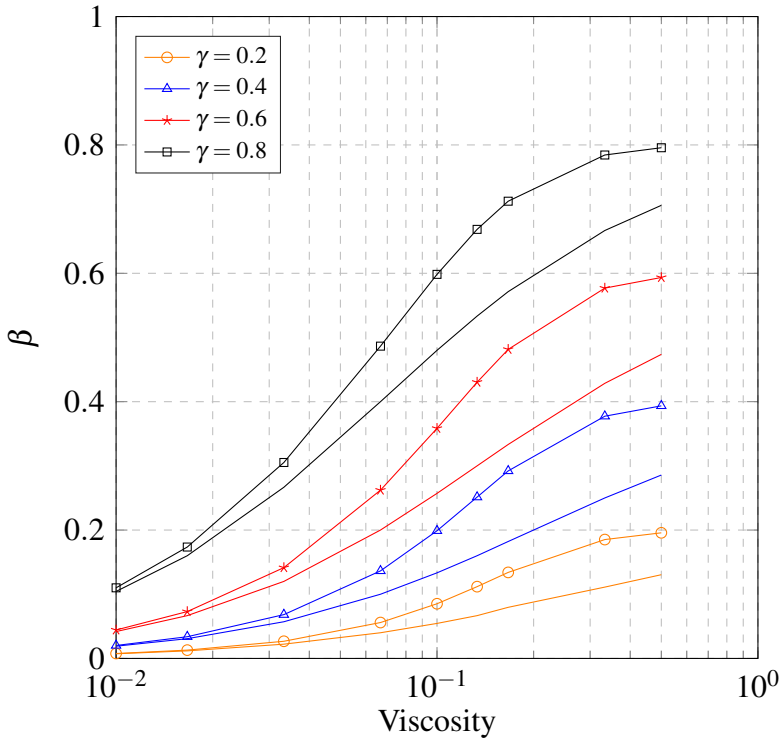

(b)

Figure 3.5: Performance of the modified solid weighting function, including (a) the normalised drag coefficient, K/K^*, at varying computational viscosity, ν, for the SC model with varying summation index, b, and (b) a comparison of the modified (with markers) and original (no markers) solid weighting function at $b = 4$ and under varying solid coverage, γ, and computational viscosity.

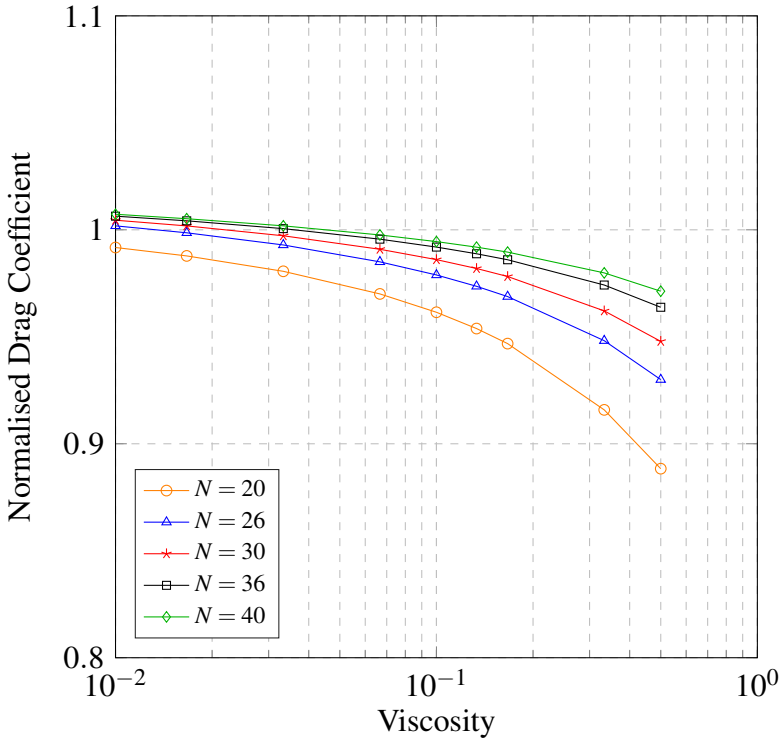

(a)

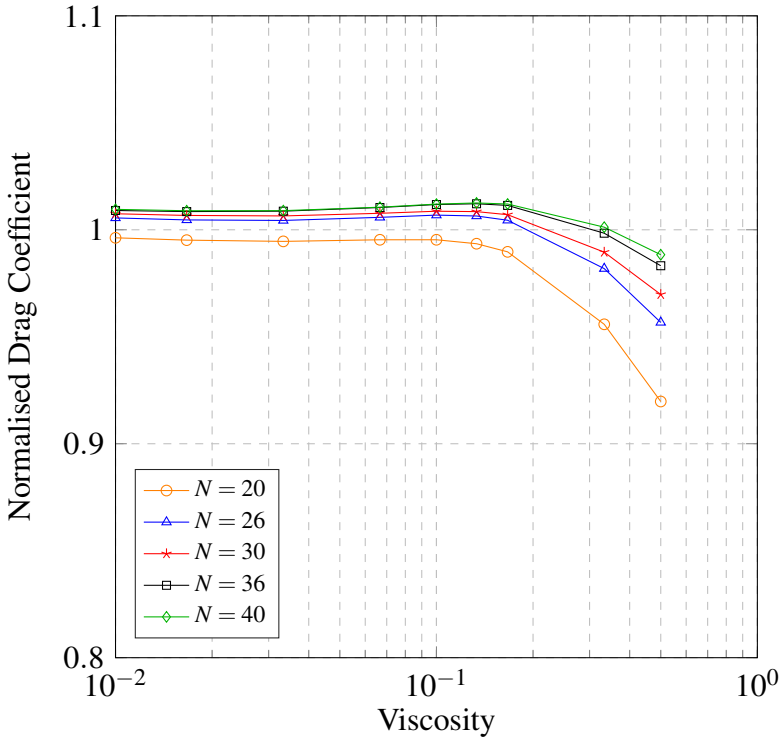

(b)

Figure 3.6: The normalised drag coefficient, K/K^*, at varying computational viscosity, ν, for the SC model with increasing lattice resolution, N, using (a) the original solid weighting function (Eq. (2.62)) and (b) the modified solid weighting function (Eq. (3.2)).

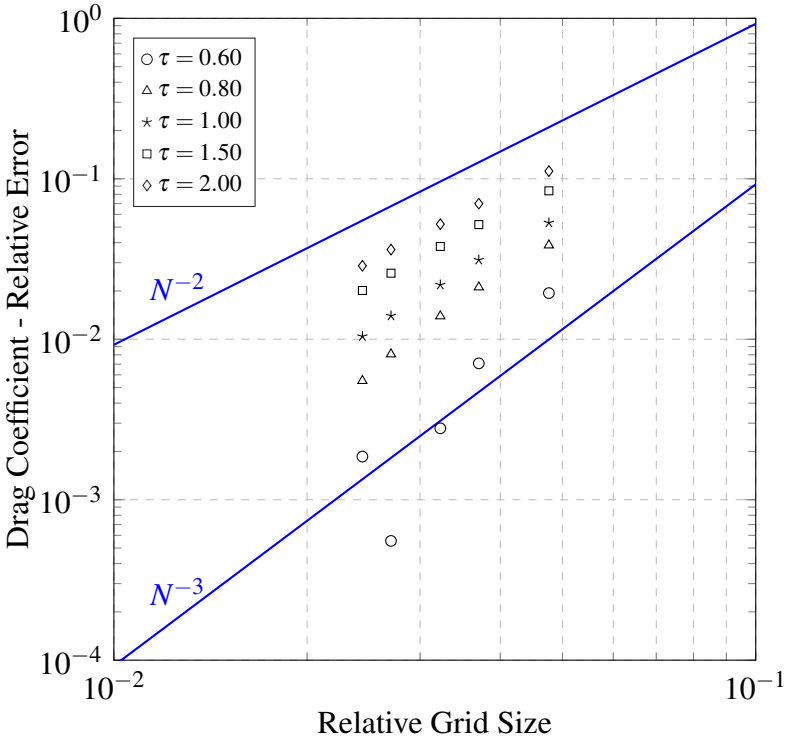

(a)

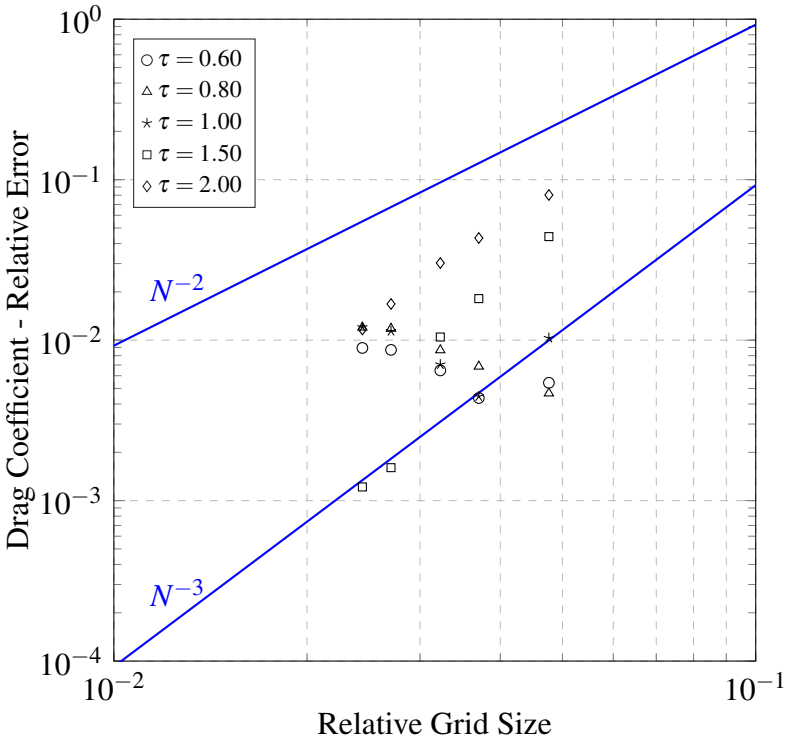

(b)

Figure 3.7: Convergence of the relative error of the drag coefficient against relative grid size when using (a) the original solid weighting function (Eq. (2.62)) and (b) the modified solid weighting function (Eq. (3.2)).

the modified solid weighting function is employed, as shown in Fig. 3.6(b), the results exhibit viscosity-independence at computational viscosities in the range $\nu < 0.1$. For both weighting functions, it can be seen that the prediction of drag coefficient increases with increasing lattice resolution, converging to a value just above the reference solution.

An interesting finding observed from Fig. 3.7 is that the order of convergence with the relative grid size changes with the relaxation parameter, τ. Approximately second-order convergence is exhibited at $\tau = 2$, which is equivalent to $\nu = 0.5$ in this case. The apparent order of convergence rises to three and even higher as τ decreases, until finally the results exceed the reference solution. This results in increasing error with increasing lattice resolution, and is more prominent for the modified solid weighting function (Fig. 3.7(b)) than it is for the original weighting function (Fig. 3.7(a)). Although the modified solid weighting function converges to an error of approximately 1%, the wide range of viscosity independence makes it a significant improvement over the original form.

To allow direct comparison of the TRT-PSM formulation, with the modified solid weighting function, to other fluid-solid boundary conditions, the case of flow through a body-centred-cubic (BCC) array of spheres was considered. The model was constructed as described in Pan et al. [4]. A BCC array of spheres with equal radii of approximately 11.8 was located in a fully periodic cubic domain. The resolution used was 32^3, and the flow was driven by a body force of 10^{-4}, resulting in a Reynolds number of 0.22. The normalised permeability results for the porous medium are presented in Fig. 3.8, along with reference results using the multi-reflection (MR) and quadratically-interpolated bounce-back (QIBB) boundary conditions.

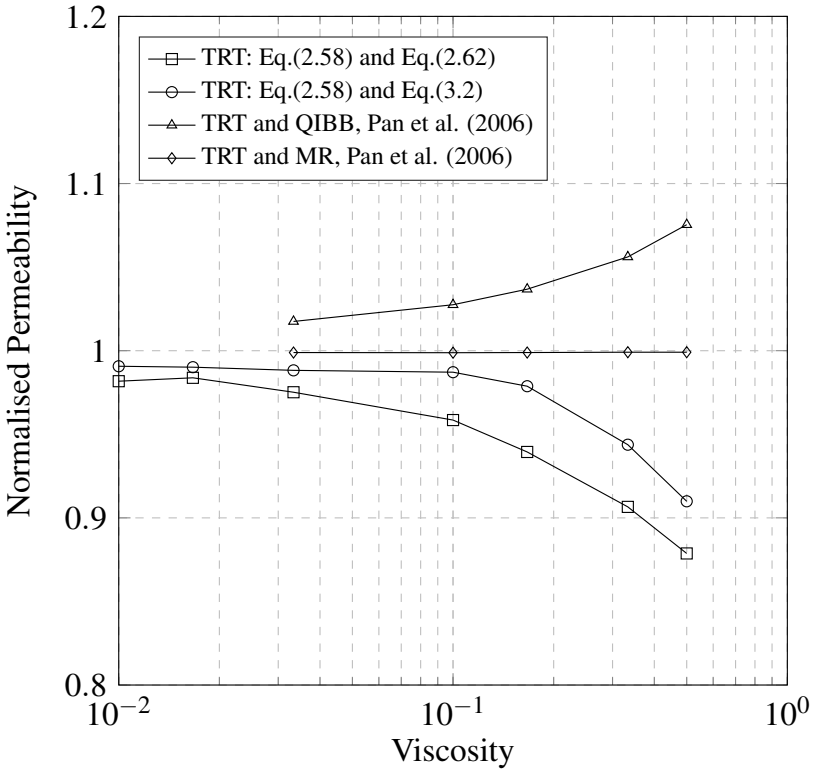

Figure 3.8: The normalised permeability, κ^*, at varying computational viscosity for flow past a body-centred-cubic array of spheres.

It can be clearly seen from Fig. 3.8 that the more complex MR boundary condition exhibits excellent accuracy and is virtually viscosity-independent. While the PSM with the modified solid weighting function

exhibits an error of approximately 2%, it is again viscosity independent in the range $\nu < 0.1$, and performs better than the original solid weighting function in both criteria. This is consistent with the results of the previous SC tests.

3.3.2 Force on a Sphere in Stokes Flow

As a natural extension to the testing reporting in Section 3.3.1, the drag coefficient of a SC array of spheres at different solid volume fractions was simulated. The model construction was similar to that of the previous test. A sphere with varying radius was fixed at the centre of a fully periodic cubic domain with $N = 30$ in each dimension. The fluid was driven by a body force of 10^{-4} in the x-direction and the relaxation parameter, τ, was set to be 0.53. The simulation was kept running until the fluid flow reached steady state.

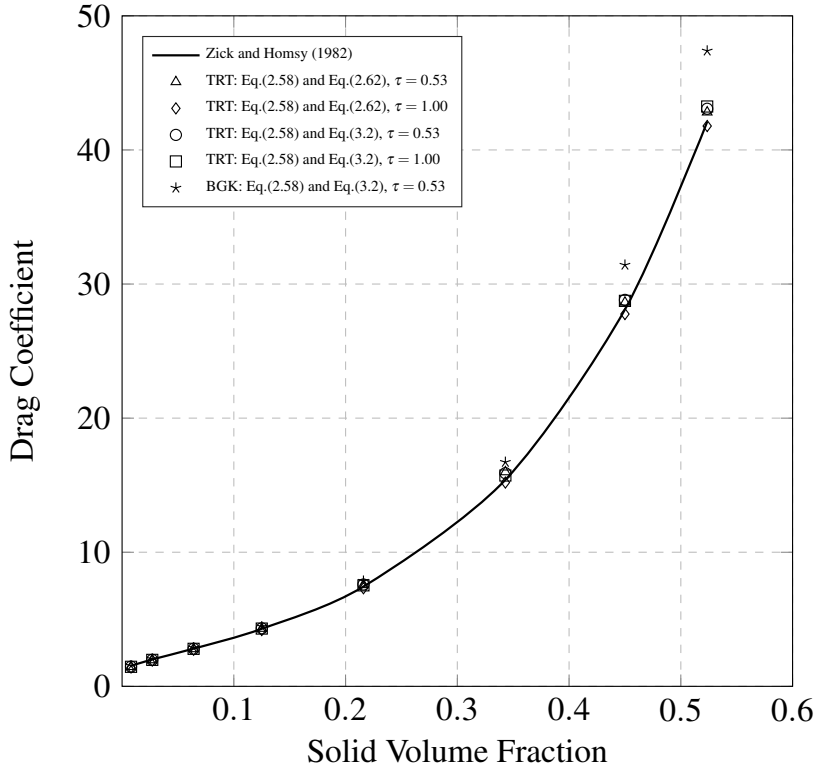

Figure 3.9: Drag coefficient, K, against solid volume fraction of the periodic cell, ϕ, for different TRT-PSM combinations. A BGK-PSM result has been included for comparison.

The results of the SC analysis at varying solid volume fraction are presented in Fig. 3.9, where it can be observed that the TRT-PSM formulation with the modified solid weighting function achieved excellent agreement with the reference values proposed by Zick and Homsy [118]. The relative drag coefficient errors of the TRT-PSM with the modified solid weighting function were within 2% of the reference values for all solid volume fractions simulated. Conversely, the BGK-PSM results deviated at high solid volume fractions. When using different relaxation parameters, it was found that the error fluctuation of the TRT-PSM was between 3% and 5%, depending on the solid volume fraction. When used with the modified solid weighting function, the error fluctuation was restricted to within 1%, which provides further evidence of the improved performance of the modified function. It should be noted that the solid volume of $\phi = \pi/6 \approx 0.524$ represents the theoretical packing limit of a SC array of spheres.

3.3.3 3D Duct Flow

To test the modified solid weighting function in a lattice-aligned geometry, steady-state flow through a square duct was simulated. Maier et al. [119] analysed this problem using both the D3Q15 and D3Q18 lattices with periodic and pressure boundary conditions. Various factors including the Mach number and the driving force were found to affect the rate of convergence to the analytical solution. Monotonic convergence was noticed when using periodic boundaries with a constant Mach number for all test cases. However, when using pressure boundaries, a *saturation effect* was reported, in which the error initially decreased but then increased with increasing lattice resolution. The authors found that the velocity was over-predicted at low resolutions and was under-predicted at high resolutions. This *saturation effect* is similar to what was observed in the convergence behaviour reported in Section 3.3.1, where the calculated drag coefficient was underestimated at low resolutions but increased to above the reference solution at high resolutions.

The quasi-parabolic axial velocity distribution for flow in a rectangular duct is given by the series approximation,

$$u_x(y,z) = \frac{16a^2}{\rho\nu\pi^3}\left(-\frac{\partial p}{\partial x}\right)\sum_{k=1,3,5,\ldots}(-1)^{(k-1)/2}\left[1-\frac{cosh(k\pi z/2a)}{cosh(k\pi b/2a)}\right]\frac{cos(k\pi y/2a)}{k^3}, \tag{3.5}$$

in which $-a \leq y \leq a$ and $-b \leq z \leq b$. It has been stated in the past that the LBM cannot exactly reproduce this flow profile due to spatial discretisation errors [120]. In addition, results [119] have shown that the error in peak velocity is the largest at an aspect ratio (the ratio of width to height of the cross-section) of one, which represents a square duct. The duct flow approaches Poiseuille flow as the aspect ratio rises, while the error decreases.

To consider the worst-case geometry, the simulation was constructed using a square duct with height, width and length of 4, 8, 10, 20, and 40 grid spacings. These correspond to lattice node counts of 5, 9, 11, 21, and 41 across the height and width of the duct, and ensure that a node is located at the centre of the cross-section. Periodic boundaries were applied to the inlet and outlet, while the PSM boundary condition was utilised for the four transverse boundaries of the duct. A body force of 10^{-5} was used to drive the fluid flow in the x-direction. To minimise the impact of the Mach number on simulation results, the body force was adjusted according to the grid spacing for each case to maintain a constant Mach number of 0.0023. The relaxation parameter was set to be 0.55 for all test cases.

The duct simulation results are summarised in Fig. 3.10. The relative error of the maximum velocity at the centre of the duct is shown in Fig. 3.10(a). The relative error of the flow profile is shown in Fig. 3.10(b), and is presented in the form of the L_2-Norm,

$$\varepsilon_{L_2} = \sum\sqrt{\frac{(u_{LBM}-u_A)^2}{u_A^2}}, \tag{3.6}$$

where u_A is calculated using Eq. (3.5) and u_{LBM} is captured from the simulation results. The error was calculated using all of the lattice nodes in the duct which were common to each simulation. The slopes in Fig. 3.10 reveal that approximately second-order convergence can be obtained for both the relative error in maximum velocity and the L_2-Norm error of the flow profile. It should be noted that the slope of the curve is greater than the theoretical slope of the LBM, which is second-order accurate in space, however this might be attributed to errors inherent in the reference solution.

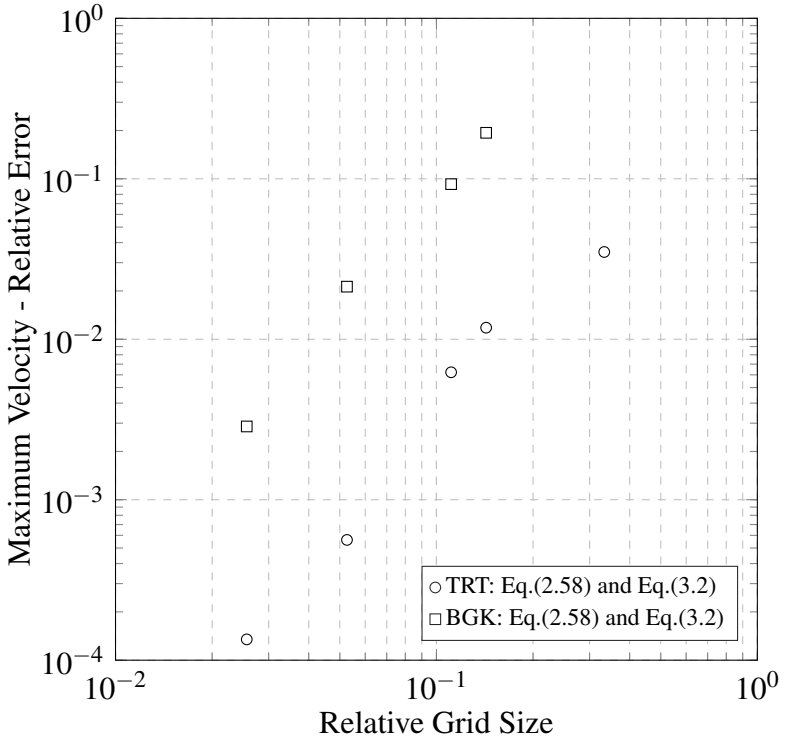

(a)

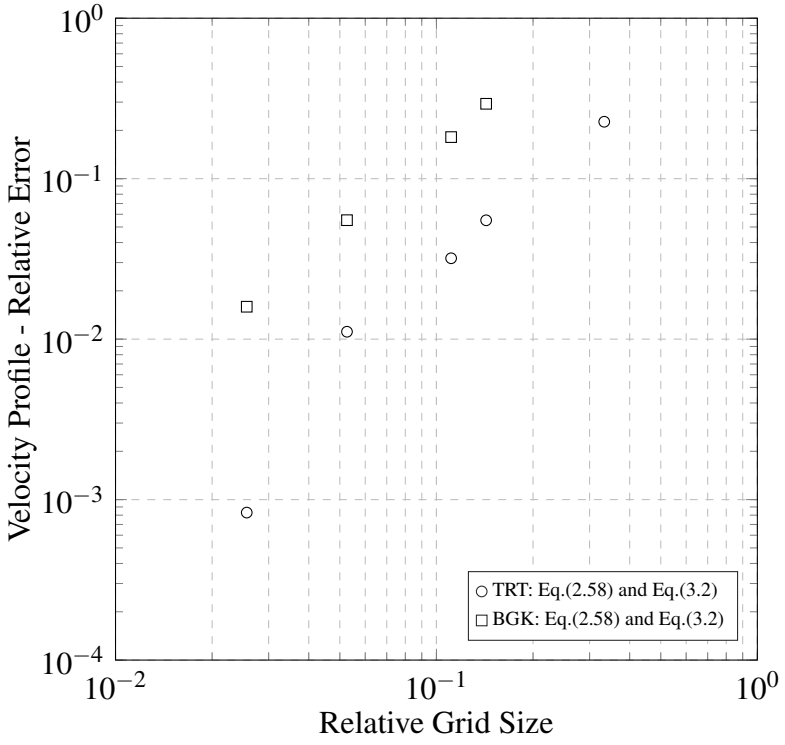

(b)

Figure 3.10: Convergence of the square duct flow simulations with increasing lattice resolution, showing (a) the relative error of the maximum velocity and (b) the relative error of the velocity profile in terms of the L_2-Norm.

3.3.4 Force on a Settling Sphere Between Two Parallel Plates

Thus far, the tests in this study have focused on flow past and through fixed solid obstacles. In order to test the modified solid weighting function for cases in which the fluid-solid boundary can move across the lattice, a heavy sphere settling between two parallel plates was simulated. The drag force acting on a settling sphere is given by,

$$F = \frac{-6\pi\rho\nu r U_{sphere}}{1 - 0.625(r/l) + 0.1475(r/l)^3 - 0.131(r/l)^4 - 0.0644(r/l)^5}, \tag{3.7}$$

where r again is the sphere radius, l represents the distance from the sphere centre to the closer wall, and U_{sphere} is the sphere velocity.

The model construction followed the case described by Strack and Cook [62], where the BGK-PSM formulation was implemented. Feng and Michaelides [121] presented a similar case where the the sphere was fixed and a velocity boundary condition was applied to the infinite lateral boundaries. Here, the walls were fixed and the sphere was allowed to settle under gravity. A schematic diagram of the simulation is shown in Fig. 3.11(a). The model was initialised with the sphere located between two walls that are $8r$ apart, and positioned such that $r/l = 0.5$. The length and depth of the domain were set to be $64r$ to minimise the impact of the domain size (see [62] for further details). Bounce-back conditions were applied to the walls while periodic conditions were used for other two directions. The sphere was allowed to settle in the static fluid under a gravitational acceleration of 10^{-4}, which resulted in a Reynolds number of approximately 0.04. The simulation was run until the velocity of the sphere reached steady state.

The settling sphere results are shown in Fig. 3.11(b), where the force can be seen to be converging at near second-order with decreasing relative grid size (the grid spacing divided by the distance between the walls). It can be seen that the TRT-PSM formulation with the modified solid weighting function is more accurate than the BGK-PSM results of Strack and Cook [62]. Similar to the results shown in Section 3.3.3, the slope of the curve exceeds the theoretical order of convergence of the LBM by a small amount, which is also reported by Strack and Cook [62]. The approximate nature of the analytical solution may be one reason for that.

3.4 Summary

This chapter has presented improvements to the simulation of particle suspensions using the LBM-DEM coupling approach. First, the benefit of using a TRT collision operator, instead of the popular BGK collision operator, was demonstrated. Second, a modified solid weighting function for the PSM for fluid-solid interaction was defined and tested. Results were presented for a range of flow configurations, including sphere packs, duct flows, and settling spheres, with good accuracy and convergence observed. The improvements presented here resulted in a range of computational viscosities, and therefore relaxation parameters, within which drag and permeability predictions remain invariant. This allows for greater flexibility in using the relaxation parameter to adjust the LBM timestep, which can subsequently improve synchronisation with the time integration of the DEM. This has significant implications for the simulation of large-scale suspension phenomena, where the limits of computational hardware persistently constrain the resolution of the LBM lattice.

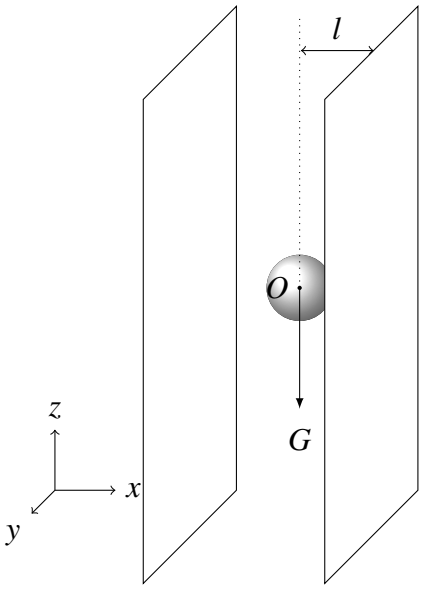

(a)

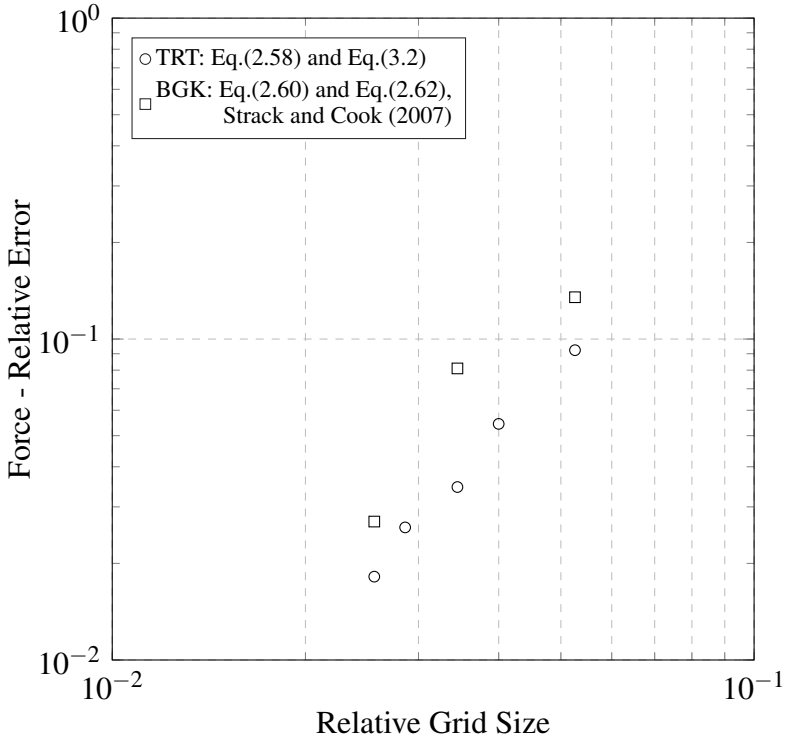

(b)

Figure 3.11: A sphere settling in a quiescent fluid between two parallel plates, including (a) a schematic diagram of the simulation and (b) convergence of the force on the sphere with increasing lattice resolution.

Chapter 4 - Numerical Rheometry of Dense Particle Suspensions

B. D. Jones, **D. Wang**, C. R. Leonardi, J. R. Williams and S. D. R. Others, Validation of a numerical framework for simulation of dense particle suspensions, *Journal of Fluid Mechanics*. (draft)

Significant portions of this chapter have been adapted from Sections 2-4 of the above manuscript. As the co-author of this paper, I was responsible for significant portions of the following aspects:

- literature review presented in Section 2,
- model development discussed in Section 4,
- analysis of results presented in Section 4,
- drafting of the manuscript.

The listed co-authors provided contributions towards the final review of the paper and suggestions as well as towards developing and improving the discussed results both in terms of analyses conducted and their presentation.

Estimated Contributions by Candidate	
Conception and design	50%
Analysis and interpretation	80%
Drafting and production	65%

Chapter 4

Numerical Rheometry of Dense Particle Suspensions

The transport of dense particle suspensions is of interest in a broad variety of industries from drug development to oil recovery. It is also of great importance to a more efficient hydraulic fracturing operation. However, the rheology of such suspensions is often characterised by semi-empirical models which lack the flexibility required to accurately capture the relevant phenomena in cases of arbitrary geometry.

Previous work in this field has focused on the development of constitutive equations to describe the effective viscosity of the suspensions as a function of the solid volume fraction. Typically derived from experimental data on fluid flow between parallel plates, the rheology specified by such expressions is often used to calibrate a power-law based rheological model. However, work by Lyon and Leal [122] has shown that even in a relatively simple Poiseuille flow situation the distribution of solid particulates is not uniform across the entire aperture. This spatially varying solid volume fraction brings into question the applicability of constitutive equations to fully describe suspension rheology.

In this chapter, the improved LBM-DEM framework is applied to numerically investigate the rheology of dense particle suspensions. Using this coupled framework with the PSM, a 3D numerical Couette flow rheometer was implemented, in which discrete element particles of different solid volumes are packed into a cubic lattice Boltzmann domain which is periodic in the lateral directions. Using either shear stress or strain rate control, this model then simulates the shear-dependent behaviour of the particulate suspensions. The resultant hydrodynamic and mechanical reactions acting on the shearing plane are evaluated once the model has reached the steady state, where these results are used to compute an effective suspension viscosity, μ_f. The results from this analysis are validated against several existing semi-empirical expressions. Meanwhile, comparison between the BGK and TRT collision operators is also presented, highlighting the better performance of the TRT-PSM formulation.

4.1 Constitutive Modelling of Particle Suspensions

The rheology of non-Brownian particle suspensions is dependent on the quantity of solid inclusions by volume. Conceptually, a suspension will behave as a simple fluid or as a granular material at low and high solid volume fractions, ϕ, respectively. This is due to the fact that the constitutive behaviour of the suspension is characterised

by stress contributions from the fluid and particulate phases. At low solid volume fractions ($\phi < 0.1$) particle-particle contact is rare, and particulates are simply advected by the fluid. At comparatively high solid volume fractions ($\phi < 0.4$) particle-particle contact is common and impacts upon the fluid's ability to flow. There also exists a limiting solid volume fraction, ϕ_m, at which the particulate inclusions become jammed and the fluid must percolate through the void space.

In the case of a Newtonian fluid the relationship between shear stress, τ_s, and shear strain rate, $\dot{\gamma}$, is known to be,

$$\tau_s = \mu_f \dot{\gamma}, \tag{4.1}$$

where μ_f is the fluid viscosity.

Singh and Nott [123] demonstrated experimentally that the apparent viscosity of particle suspensions is dependent both on solid volume fraction and shear rate. As such, Eq. (4.1) is not sufficient to fully describe the constitutive behaviour. Instead the combination of contributions from the fluid and particulate phases can be described with a suspension balance model [124] in which the shear and normal stresses exerted by the suspension are related to the shear strain rate so that,

$$\tau_s = \mu_f \mu_s \dot{\gamma}, \tag{4.2}$$

and,

$$p' = \mu_f \mu_n \dot{\gamma}, \tag{4.3}$$

where the terms μ_f, μ_s, and μ_n, are the fluid, particle shear, and particle normal viscosities respectively.

The particle shear and normal viscosities are dimensionless and can be found by,

$$\mu_s = \frac{F}{I}, \tag{4.4}$$

and,

$$\mu_n = \frac{1}{I}, \tag{4.5}$$

in which F is the *friction coefficient*. I is the dimensionless *viscous number*, first proposed by Cassar et al. [125], and is simply the ratio of fluid shear stress to particle normal stress,

$$I = \frac{\mu_f \dot{\gamma}}{p'}. \tag{4.6}$$

The viscous number characterises the relative impact of particle and fluid stresses on apparent viscosity. Where I is low, viscous stresses exerted by the solvent are insignificant when compared with particle stress. Conversely, in the case of a high value of I viscous stresses are dominant.

By considering the experimental data of Phillips et al. [126], Morris and Boulay [127] proposed expressions for prediction of the viscous number and friction coefficient which are dependent only on the solid volume fraction and two tuning parameters. Their expression for viscous number is given by,

$$I(\phi) = \frac{\left(\frac{\phi_m}{\phi} - 1\right)^2}{K_n} \tag{4.7}$$

where comparison to Phillips et al. [126] determines the tuning parameter to be, $K_n = 0.75$. Morris and Boulay [127] then use the viscous number to predict a friction coefficient,

$$F(I) = F_1 + I + \frac{5}{2}\phi_m \frac{I^{\frac{1}{2}}}{K_n^{\frac{1}{2}}}, \tag{4.8}$$

with $F_1 = 0.133$ and a jamming solid volume fraction of $\phi_m = 0.68$.

An important consideration for these expressions is that the jamming solid volume fraction selected is above the random close pack limit which has been found to be in the range, $\phi_{rcp} = 0.63 - 0.64$. Additionally, since Morris and Boulay [127] calibrated their expressions against the data of Phillips et al. [126], their validity should be limited to low Reynolds number cases.

Building on the work of Morris and Boulay [127], Boyer et al. [128] carried out a series of experiments using a custom built annular shear cell, also at low Reynolds numbers. Since they were interested in resolving the relationship between particle pressure and friction coefficient, the annular shear cell was designed with a porous top surface. Such a design allows the confining pressure to be imposed upon the suspension, though the solid volume fraction is variable as a result. Another modification to their annular shear cell over a typical shear cell rheometer was the addition of $0.5mm$ steel bars to the top and bottom surfaces. The spacing of these steel bars was chosen to be consistent with the particle diameter, with the intention of better capturing the bulk rheology of dense particle suspensions. By assuming a jamming solid volume fraction of $\phi_m = 0.585$, the results from this experimental analysis suggested that the scaling parameter K_n is unnecessary so that,

$$I(\phi) = \left(\frac{\phi_m}{\phi} - 1\right)^2. \tag{4.9}$$

Considering this adjusted expression, Boyer et al. went on to propose the following equation to approximate the friction coefficient,

$$F(I) = F_1 + \frac{F_2 - F_1}{1 + \frac{I_0}{I}} + I + \frac{5}{2}\phi_m I^{\frac{1}{2}}, \tag{4.10}$$

where the tuning parameters are chosen to be $F_1 = 0.32$, $F_2 = 0.7$ and $I_0 = 0.005$, to agree with their results.

The motivation behind the form of these equations for friction coefficient was to separate particle contact (or mechanical) and hydrodynamic contributions to friction. Where the last two terms in Eq. (4.8) and Eq. (4.10) represent the hydrodynamic contribution, and the preceding terms represent the contact contribution. In their recent work, Lecampion and Garagash [124] propose that the expression of Boyer et al. [128] is erroneously dominated by hydrodynamic contributions as the solid volume fraction approaches the limiting solid volume fraction ($\phi \to \phi_m$). They propose instead that the friction coefficient is more accurately represented by the following expression where the first two terms represent the inter-particle contact contribution,

$$F(I) = F_1 + \frac{\phi_m}{\beta}\left(1 - \frac{\phi}{\phi_m}\right) + \left(I + \left(\frac{5}{2}\phi_m + 2\right)I^{\frac{1}{2}}\right)\left(1 - \frac{\phi}{\phi_m}\right)^2. \tag{4.11}$$

This expression for friction coefficient is designed to be compatible with the expression for viscous number proposed by Boyer et al. [128], and was calibrated against their experimental results.

4.2 Approaches to Modelling Particle Suspensions

Numerical simulation of suspension rheometry requires, in the general case, the coupling of two simulation techniques to represent the fluid and particulate phases individually. This has been explored by a variety of authors using a number of techniques including classical application of time and space integration to the Navier-Stokes and Newtonian motion equations, to the more recent dissipative particle dynamics and lattice Boltzmann methods. Here a brief review of contemporary works and accompanying numerical methods is firstly presented.

4.2.1 Stokesian Dynamics

The simplest numerical approach applied in the literature is that of Stokesian dynamics [129]. Of the techniques discussed here, Stokesian dynamics is unique in that it does not explicitly consider the fluid phase. Instead, hydrodynamic drag is applied to particles using the analytical expression under the Stokes flow regime. The interaction between particles includes an additional *lubricating* force to include consideration of the strong hydrodynamic forces exerted on approaching particles. Since no additional work is done to consider directly the fluid phase, this method could be seen as computationally inexpensive, however the consideration of long range particle interactions increases the computational expense of the particle phase significantly.

Sierous and Brady [130] applied Stokesian dynamics to the investigation of suspension rheometry. They found that with their model they were able to correctly capture suspension rheology in the dilute regime without needing to account for lubrication forces. In order to correctly capture the suspension rheology at high concentrations, explicit treatment of lubrication forces was required. The authors do not comment on whether shear dependent rheology was observed.

In a following study Sierous and Brady [131] applied Stokesian Dynamics to the study of uniformly sheared suspensions, in which a pair-distribution function was determined to characterise the inter-particle contact. Furthermore, the pair-distribution function clearly showed anisotropy in the microstructure between particles, which caused non-Newtonian behaviour. However, their results showed a shear thickening behaviour, which disagreed with the experimental study. The simple potential-like force description was not able to mimic the shear-rate-dependent non-hydrodynamic inter-particle forces. In the work by Swan and Brady, [132, 133], Stokesian Dynamics were applied to the investigation of particle suspensions between parallel walls. In these studies, the hydrodynamic interactions were divided into near- and far-field components. A splitting parameter was introduced to further distinguish the far-field hydrodynamic interactions into those mediated by both walls and those mediated by a single wall. The splitting procedure caused an exponentially small error, as the interactions mediated by both walls were reproduced while those mediated by a single wall were treated as a superposition approximation. Stokesian Dynamics has also been extended to non-spherical particle suspensions, where a modified lubrication tensor was developed to describe the interactions between multiple pairs of overlapping particles [134].

4.2.2 Smoothed Particle Hydrodynamics

Smoothed particle hydrodynamics (SPH) is seen as a similar approach to dissipative particle dynamics (DPD), in that they are both particle based methods. However, their respective interaction forces are fundamentally different. SPH is a partition of unity method, in which particles are Lagrangian elements representing a continuum field.

Where SPH differs from DPD is that the SPH formulation is a discretisation of the Navier-Stokes equation which is therefore included explicitly, rather than being emergent. Despite this fundamental difference, the treatment of boundary conditions is similar. In their work, Bian et al. [135] applied the *frozen particle* approach to represent suspended particles in order to investigate the rheology of suspensions. A lubrication force correction, which was solved by an implicit splitting integration scheme [136], was incorporated to account for the short-range forces between particles. By shearing suspensions of spherical particles, Bian et al. [135] validated their approach by comparing, favourably, to published constitutive expressions at a fixed shear rate. In contrast to the work of Iwashita and Yamamoto [137], Bian et al. [135] found their model to exhibit shear thickening rheology. It should be noted that the work of Bian et al. [135] was done in 2D only, which may be a source of observed differences.

Vazquez-Quesada et al. [138] extended the SPH model to 3D to simulate particle suspensions under shear flow conditions. Results from the 3D SPH model were in good agreement with the literature for the solid volume fraction, ϕ, up to 0.3. With the increase of ϕ, the deviation significantly grew up to 60% at the largest value considered, which was 0.5. To better characterise particle interactions, Vazquez-Quesada and Ellero [139] modified the lubrication force correction by incorporating both normal and tangential interparticle short-range lubrication forces. Additional repulsive forces were also introduced to prevent overlapping between particles. This modification successfully expanded the simulation results agreement up to $\phi = 0.35$, while reducing the deviation to 20% at $\phi = 0.5$. It was also found that the suspension rheology was Newtonian at low solid concentrations up to $\phi = 0.3$. Weak shear-thickening behaviour was observed for larger solid volume fractions. In another study, Vazquez-Quesada et al. [140] applied the 3D SPH model to investigate particle suspensions in Non-Newtonian fluid. A hidden high-shear power law behaviour was introduced to the suspending fluid, resulting in a strong shear-thinning effect of the overall suspension rheology. Even the original weak shear-thickening behaviour where Newtonian fluid was applied turned to shear-thinning with the non-Newtonian fluid model. In a recent study, Vazquez-Quesada and Ellero [141] extended the 3D SPH model to investigate particle suspensions in a viscoelastic liquid, to which a coarse-grained fluid-particle model was applied. Test cases including single particle rotation and migration, two-particle trajectories and multi-particle sedimentation were demonstrated.

4.2.3 The Finite Element Method

The finite element method (FEM) has been applied to direct numerical simulations of fluid-solid systems for decades. One outstanding feature of this approach is that one can calculate both the status of the fluid field and the particle velocities at the same time step. An arbitrary Lagrangian-Eulerian (ALE) technique [142] is applied to handle the movement of the domain and to update the body-fitted mesh at each time step. A detailed discussion on the criteria of the remeshing procedure can be found in [143]. Thogersen and Dabrowski [144] introduced a 2D finite element model for particle suspensions to investigate the hydrodynamic limit and mixing behaviour due to simple shear flow. It was found that the shear-induced self-diffusive behaviour of the fluid was stronger than the particle phase. However, the particles were assumed to be fully lubricated throughout the study. The simulation would stop whenever particle overlap was detected, which certainly added a limit to the particle density as well as the strain rate that was applied.

Walter et al. [145] coupled an explicit finite element method with a boundary integral method to simulate the motion of a spherical capsule enclosed by a membrane in simple shear flow. During each time step, the load acting on the membrane was calculated using the deformation from the finite element method, thus the velocity of the capsule could be determined from the obtained load using the boundary integral method. In this approach,

a variational form of the sphere surface equilibrium equation was applied to overcome the topological problem when using the local equilibrium equation. This approach was found to be appropriate to characterise fluid-solid interactions especially for deformable solid particles and shell-like objectives. Matsunaga et al. [146] expanded the coupled finite element and boundary element method to investigate the rheology of dense spherical capsule suspensions. To account for the interactions between particles, a fine mesh was required to resolve the near-field forces, while the far-field forces were coarse-grained by a multi-pole expansion [147], where a patch consisting of a group of elements was applied to resolve the particle surface. Several validation cases were demonstrated in the literature. However, this approach is still not computationally efficient due to large number of boundary elements and the remeshing process.

4.2.4 Homogenisation Modelling

Chateau et al. [148] studied the behaviour of rigid particle suspensions in a yield-stress fluid using a homogenisation approach, in which a representative element volume was defined to describe the suspension domain. It was assumed that the fluid was homogeneous and the solid particles were isotropically distributed over the domain. Avazmohammadi and Castaneda [149] extended this homogenisation approach to deformable viscoelastic particle suspensions by the use of a deformation gradient tensor. In their studies, a shear-thinning behaviour was observed as a result of the particle deformation under shear flow conditions. The homogenisation approach has emerged as an appropriate method to capture the macroscopic behaviour of particle suspensions. However, due to homogenisation and isotropic assumptions, the homogenisation cannot fully resolve the exact suspension behaviour such as the particle interactions and distribution.

4.2.5 The Lattice Boltzmann Method

Within the scope of the LBM, one popular approach to characterise the fluid-solid boundary conditions is the interpolated bounce-back (IBB) scheme. However, as stated in Section 2.3, these IBB schemes are not able to accurately compute the hydrodynamic force on the interface, especially when simulating moving particles. In this scenario the computed force and torque may experience fluctuation as the boundary nodes are remapped in a discrete manner at each time step. To diminish the hydrodynamic force fluctuation, an efficient hydrodynamic radius, which is greater than the actual sphere radius, was introduced to the LBM. Haddadi and Morris [150] applied this scheme to study dilute sheared suspensions of neutrally buoyant spheres at low Reynolds numbers. In this study, the hydrodynamic interaction between particles was calculated by the near-field lubrication force and he particle velocity was obtained from a partitioned algorithm.

Another popular approach is to couple the LBM with the immersed boundary method (IBM) to treat fluid-solid boundary conditions. In IBM, a set of discrete markers which are governed by Lagrangian dynamics are used to describe the fluid-solid boundary geometry. Hence the fluid-solid interaction is modelled by an additional forcing term on the fluid boundary node via the Dirac delta function. It is worth mentioning that the IBM exhibits first-order accuracy, which is different to the bounce-back boundary conditions. Breugem [151] implemented a direct forcing scheme in which a second-order midpoint rule was applied and thus improved the IBM to second-order accuracy. In a more recent study, Zhou and Fan [152] incorporated the Runge-Kutta scheme with inner steps in the IBM to achieve better accuracy when simulating rigid-particle-laden flows.

In many of the LBM-based simulations, the hydrodynamic force acting on a moving particle is evaluated by the momentum exchange method (MEM), in which the momentum changes between fluid nodes and fluid-solid boundary nodes are summed up during bounce-back. However, studies [153, 154] have shown that the conventional MEM is not locally Galilean invariant. Wen et al. [154] corrected the conventional MEM force calculation by incorporating the relative velocity between the fluid population and the fluid-solid boundary to achieve Galilean invariance. The new, Galilean invariant MEM has better simulation accuracy as well as a clearer physical interpretation especially for the modelling of moving particles in fluids.

To evaluate the performance of various formulations of the LBM, Peng et al. [155] set up several benchmark problems for analysis. It was concluded that all the tested interpolated bounce-back schemes were second-order accurate, among which the quadratic interpolations were more accurate than the linear interpolations, with weaker force fluctuations. Furthermore, the MEM with rigorous Galilean invariance yielded better accuracy when calculating hydrodynamic force. Special attention was paid to the refilling process by Peng et al. [155] and Shi et al. [156]. Many of the LBM simulations for particle suspensions treat the fluid-solid boundary as a moving shell. Bounce-back is applied to both inside and outside nodes of the shell. Hence the hydrodynamic force is affected by the momentum exchange on both sides. However, in some treatments, only the contribution from outside the shell is considered when calculating the hydrodynamic force. Consequently when a particle is in motion, some fluid nodes which are originally inside the particle would appear with unknown particle distribution functions. This is called the *refilling* process. For simulations of complex flows with large amount of moving particles, the refilled fluid nodes significantly affect the stability and accuracy. Comparisons of different refilling schemes can be found in [155] and [156]. It was stated that the velocity-constrained normal extrapolation refilling scheme provided the best stability and accuracy.

Johnson et al. [157] coupled the LBM with the DEM via the partially saturated method to study the shear-thickening phenomenon of particle suspensions. Several parameters including the solid fraction, particle-wall contact stiffness and inter-particle contact stiffness were investigated. It was found that the dilation was a key observation during shearing, which was also a probable reason for the shear-thickening behaviour. Results also showed that there existed a potential critical value for the applied shear stress to achieve shear-thickening. In their study, shear-thickening was observed when the applied shear stress was less than $10kPa$. However, due to the lack of test cases, the suspension behaviour was unclear for shear stresses larger than $10kPa$.

4.3 Numerical Rheometry in a Periodic Shear Cell

To validate the LBM-DEM coupling framework for suspension viscosity against the semi-empirical expressions introduced in Section 4.1, a periodic shear cell rheometer was defined. The model domain was periodic in the lateral x- and y-directions. Two discrete element platens were mapped to the z-boundaries, with the upper driven by either a constant shear force or velocity and the lower kept static. In this investigation, the rheometer was configured with a certain platen height, where the particulates in this case had a nominal radius of $100\mu m$ with a standard deviation of $10\mu m$. The models were run under both stress and strain rate control, where a stress of $\tau_s = 15\ Nm^{-2}$, or strain rate of $\dot{\gamma} = 150\ s^{-1}$, were respectively applied. A schematic diagram of the rheometer is included in Fig. 4.1 for reference.

After the validation of suspension viscosity, the viscous number and friction coefficient of the suspension were computed and compared with the semi-empirical expressions. In a more detailed analysis, the hydrodynamic

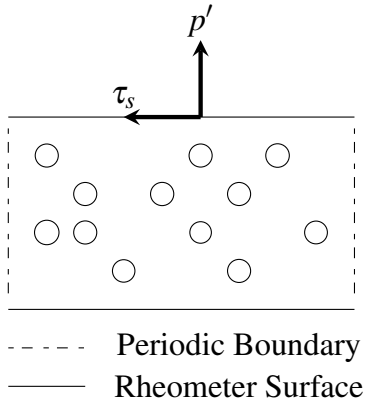

Figure 4.1: A schematic diagram of the rheometer.

and mechanical contributions to the friction coefficient were evaluated separately. In addition, shear-dependent behaviour of the suspension was also investigated, providing fundamental new insights to particle suspensions.

4.3.1 Model Setup

To minimise the impact of simulation parameters on the results, a set of sensitivity tests were firstly conducted, where a rheometer of $0.004m \times 0.002m \times 0.0025m$ was set up. The upper platen was set at the height of $z = 0.002m$ to execute stress or strain rate control. The lattice spacing, Δx, was chosen as $0.00005m$, leading to a total of $169,371$ nodes. The kinetic viscosity ν was $10^{-4}\ m^2/s$ and the relaxation parameter τ was 1, resulting in an LBM timestep $\Delta t_{LBM} = 4.17 \times 10^{-6} s$. The DEM timestep, Δt_{DEM}, was set as the same as Δt_{LBM} to ensure the coupling system executes stably. From these tests, an appropriate platen height was expected to be obtained such that the platen surfaces do not heavily affect the physical property of the suspensions, e.g. viscosity. To achieve this, a series of models where the platen height, H_z, was chosen as a function of the average particle diameter, $r_{average}$, ranging from $r_{average}$ to $10 r_{average}$.

The results are shown in Fig. 4.2, where the ratio of effective suspension viscosity to carrier fluid viscosity ($\mu_r = \mu_{eff}/\mu_f$) is plotted against the platen height. The model shows that the viscosity ratio is relatively consistent for a platen height above two particle diameters. Hence, the rheometer was configured with a platen height of 10 nominal particle diameters in all cases presented in the following sections, while other simulation parameters were kept the same as that stated in the previous paragraph.

4.3.2 Validation of Suspension Viscosity

The simulation results for effective viscosity were compared with the values computed from Eq. (4.8), Eq. (4.10), and Eq. (4.11). For this comparison, the friction coefficients were computed using the viscous number recovered from the computational model and calculated with Eq. (4.6). The effective viscosity suggested by these expressions is then found by equating Eq. (4.1) and Eq. (4.2), as the product of the solid and fluid viscosities so that,

$$\mu_{eff} = \mu_f \mu_s. \tag{4.12}$$

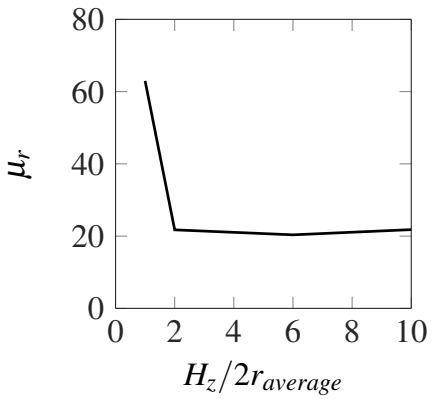

Figure 4.2: Platen height H_z in average particle diameters $r_{average}$ against viscosity ratio μ_r, at a solid volume fraction of $\phi = 0.5$.

The viscosity ratio, as the ratio of suspension viscosity to carrier fluid viscosity ($\mu_r = \mu_{eff}/\mu_f$), was then computed and compared with the values calculated from the semi-empirical expressions.

Shown in Fig. 4.3 and Fig. 4.4 are the results from this modelling, where those shown in the former are taken under strain rate control ($\dot{\gamma} = 150\ s^{-1}$) and the those in the latter are computed under stress control ($\tau_s = 15\ Nm^{-2}$). The BGK results are included for a direct comparison.

The LBM-DEM results for viscosity ratio agree in general with the expected viscosity suggested by the semi-empirical expressions, with quantitative agreement below a solid volume fraction of 40% ($\phi < 0.4$) in both control regimes, for both TRT and BGK collision operators. However, the TRT exhibits better accuracy and numerical stability over the BGK, especially under strain rate control where the BGK was unstable in some cases (e.g. $\phi = 0.2$ and $\phi = 0.55$). Under stress control, quantitative agreement is achieved with Morris and Boulay up to a very dense solid volume fraction of 55% ($\phi \approx 0.55$), where agreement in this region is more qualitative than that under strain rate control. Both TRT and BGK performed well in this regime.

The results obtained under strain rate control in Fig. 4.3 show a substantial difference between the expression of Lecampion and Garagash and those of the other authors. In fact, Lecampion and Garagash designed their expression to closely match the expression of Boyer et al. and tuned it to match their own experimental data. To explain such difference, recall Eq. (4.11), in which Lecampion and Garagash use the solid volume fraction, ϕ, as a scaling parameter. However, this requires that there is a constant relationship between the viscous number I and ϕ. However, this relationship is only applicable in the shear stress controlled models, which exhibit a much lower strain rate than that applied in the strain rate controlled regime. In addition, in the work of Lecampion and Garagash, it is also suggested that the experimental results of Boyer et al. are of better quality than those of Phillips et al.. In the experiments by Phillips et al., the platen was smooth, and conducted under shear stress control at a fixed vertical offset. This is in contrast to the experiments of Boyer et al., who used a rough platen under both normal and shear stress control. The motivation behind such an experiment was to better capture the bulk fluid behaviour.

The purpose of the studies presented in this section is to showcase the capability of the computational model to reproduce the actual rheology of particle suspensions. The model itself is configured more closely to the experiments of Phillips et al. and thus, the LBM-DEM results agree more closely with the expression proposed by Morris and Boulay, Eq. (4.8). The results of the computational models deviate quickly when the solid volume fraction exceeds 55% in both control regimes. This limitation is likely due to the stiffness of particle contact in

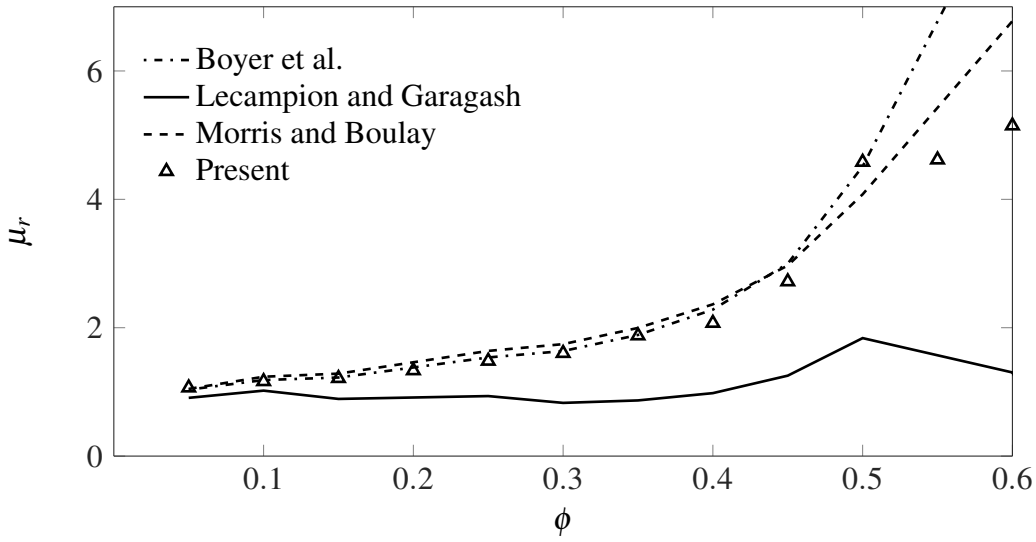

(a)

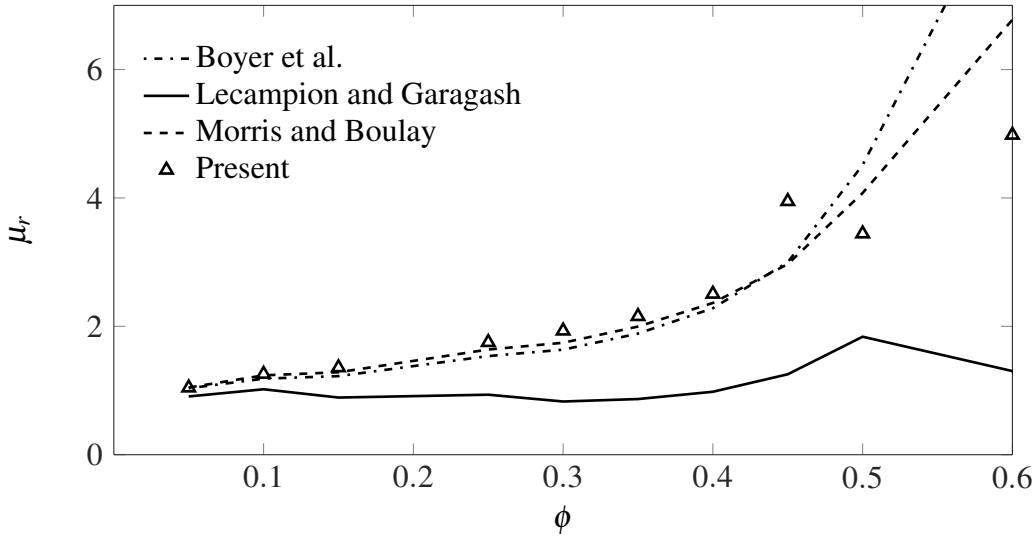

(b)

Figure 4.3: Solid volume fraction against viscosity ratio under strain rate control using (a) TRT and (b) BGK.

the discrete element model. At high solid volume fractions, the particle pressure increases exponentially. To ensure that particles do not penetrate excessively in this case, the contact stiffness would have to be increased proportionately. Whilst this is technically possible, the DEM timestep would be severely decreased, which has implications for the LBM timstep and the wall time required for the model. It is expected that results for solid volume fractions approaching the random close pack limit would improve drastically with a higher contact stiffness, which will be presented in Section 4.3.6.

4.3.3 Validation of Viscous Number and Friction Coefficient

Shown in Fig. 4.5 are plots of the viscous number against the resultant friction coefficient in both control regimes. Due to the large range of the results, Fig. 4.5(b) presents a closer look into the relationship between the viscous number and friction coefficient within the low friction coefficient range, from 10^{-4} to 1.

Results show that the LBM-DEM results are in good agreement with Eq. (4.8) proposed by Morris and

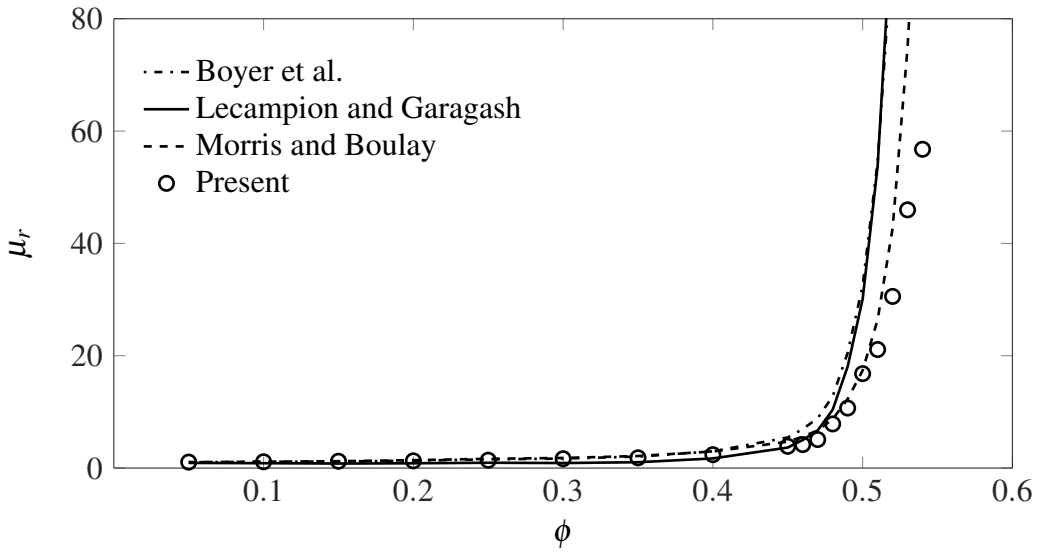

(a)

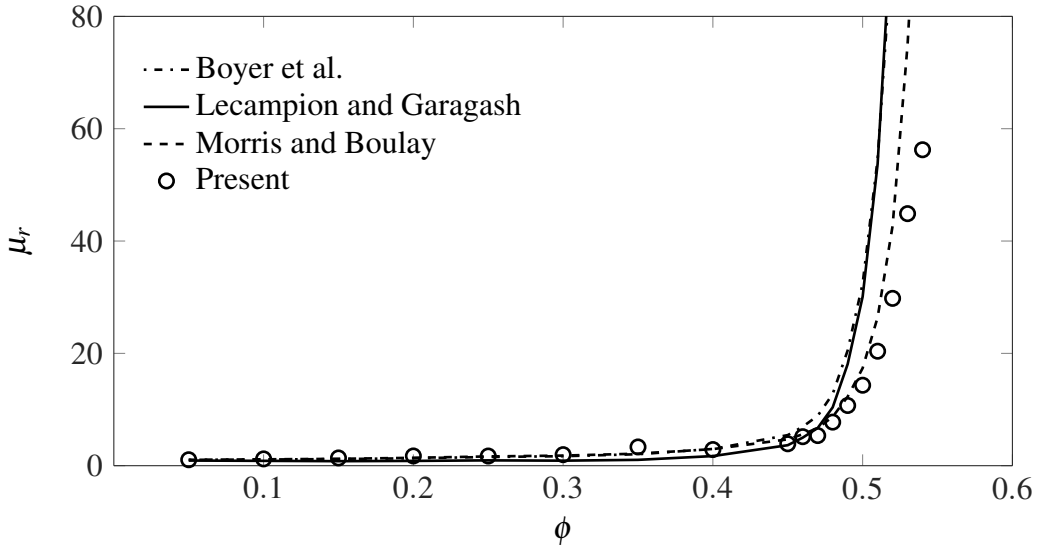

(b)

Figure 4.4: Solid volume fraction against viscosity ratio under stress control using (a) TRT and (b) BGK.

Boulay, which is consistent with the results discussed in Section 4.3.2. This is also expected as the moving platen implemented in the computational model was smooth, and not as rough as that used by Boyer et al.. It is notable that qualitative agreement with all expressions is achieved across the entire range of viscous numbers, ranging from 10^{-4} up to approximately 10^{3}.

4.3.4 Analysis of Hydrodynamic and Mechanical Contributions to Suspension Friction Coefficient

In the experiments carried out with a rheometer, it is somewhat difficult to distinguish the hydrodynamic and mechanical contributions to the shear and normal stresses acting on the moving platen. However, this is possible in the numerical modelling with the use of the LBM-DEM coupling approach. In detail, the hydrodynamic F^{hydro} and mechanical F^{mech} contributions to the friction coefficient can be calculated separately from the LBM

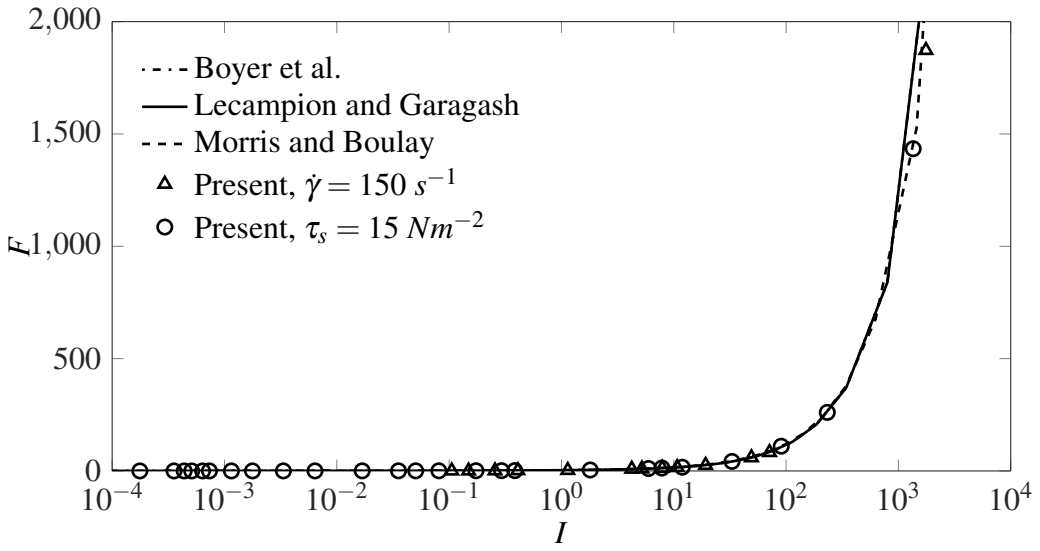

(a) Full range of modelling results

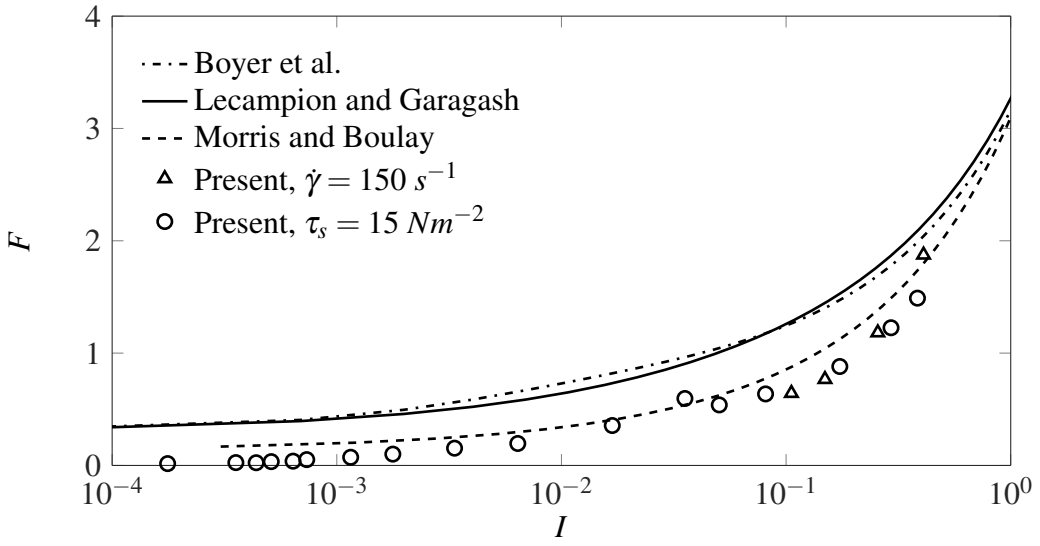

(b) Low friction coefficient range

Figure 4.5: Viscous number against friction coefficient under either strain rate or stress control.

and DEM modules. This is significant as Eq. (4.8), Eq. (4.10), and Eq. (4.11) are proposed using the principle of combined hydrodynamic and mechanical contributions to the friction coefficient.

To compute the hydrodynamic and mechanical contributions to the friction coefficient, the following equations are used,

$$F^{hydro} = \frac{\tau^{LBM}}{p'}, \tag{4.13}$$

for the hydrodynamic contribution and,

$$F^{mech} = \frac{\tau^{DEM}}{p'}, \tag{4.14}$$

for the mechanical contribution. τ^{LBM} and τ^{DEM} are the shear stresses acting on the moving rheometer platen with from the viscous fluid and particles, respectively.

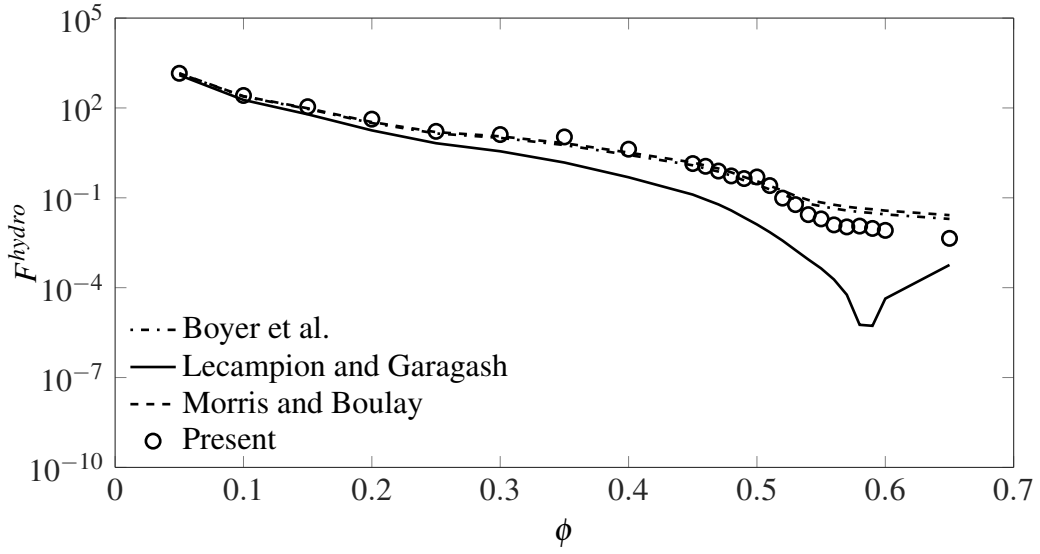

(a)

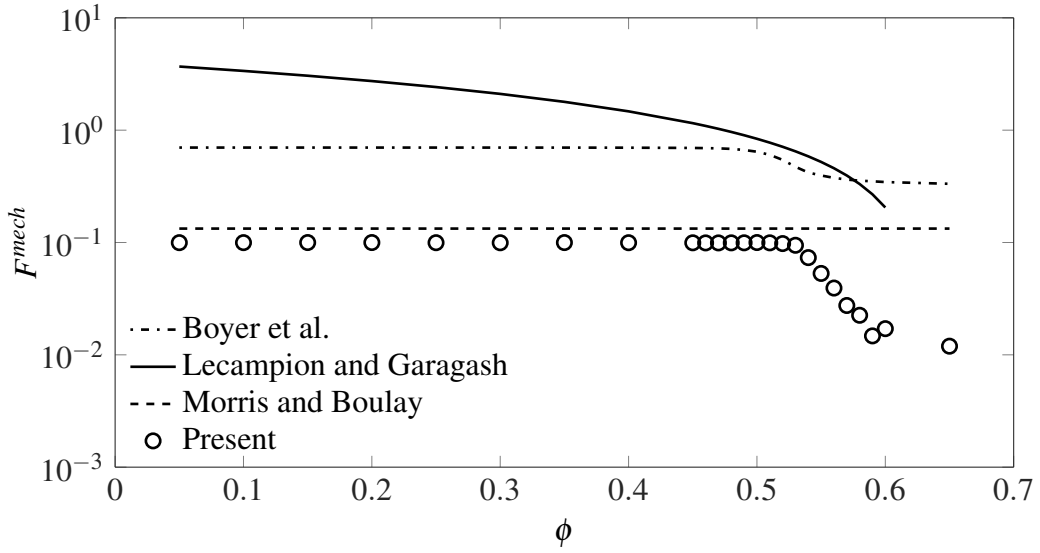

(b)

Figure 4.6: Hydrodynamic and mechanical contributions to the friction coefficient.

The results are collated in Fig. 4.6, with the semi-empirical expressions included for comparison. It is worth mentioning that the results presented in Fig. 4.6 are calculated from the stress control regime, which also enables the verification of the LBM-DEM model against the shear stress which was applied to the platen.

An intuitive observation from Fig. 4.6 is that both contributions start to dramatically decrease when the solid volume fraction exceeds 55%. This effect can be explained by the significant decrease in the platen velocity at high solid volume fractions, as the platen is driven by a constant shear force.

In regard to the hydrodynamic contribution which is plotted in Fig. 4.6(a), the LBM-DEM results are in good agreement with both Morris and Boulay and Boyer et al., despite a deviation from the expressions above a solid volume fraction of 55%. As discussed in the previous sections, it is expected that this region would improve with an increase in the DEM contact stiffness. For the mechanical contribution to friction coefficient, the LBM-DEM results are in greatest agreement with the expression of Morris and Boulay. However, this level of agreement ceases above a solid volume fraction of 55%. Again, an increase in the DEM contact stiffness

would be expected to improve the agreement. It is worth noting that while there is little quantitative agreement with the expression of Boyer et al., good qualitative agreement is achieved. The lack of quantitative agreement with the expression of Boyer et al. is expected. The empirical expression suggests a higher contact friction which is consistent with the fact that their platen had a rough surface, while the platen surface in the computational model was geometrically smooth.

4.3.5 Shear-Dependent Rheology of Particle Suspensions

As shown in the semi-empirical expressions in Section 4.1, the viscous number, I, is only a function of the the solid volume fraction, ϕ. Additionally, in the equations for friction coefficient, the viscous number is the only variable as other terms are tuning parameters. Hence, these semi-empirical expressions are not able to capture the shear-dependent rheology, which is commonly observed in particle suspensions. To explore the exact rheology of the suspensions, a series of models at $\phi = 0.20$ and $\phi = 0.55$ with varying strain rates in the strain rate control regime were implemented and tested. These solid volume fractions were chosen as they represent a relatively sparse and dense packing of the particles, where the former case is dominated by hydrodynamic force, and the latter by mechanical contacts. A schematic diagram of the velocity contour at these two solid volume fractions is illustrated in Fig. 4.7 under a strain rate $\dot{\gamma} = 50\ s^{-1}$. It is clearly shown that a near-linear velocity profile is generated at a dilute solid volume fraction of 0.20, while this effect is not obvious at a dense solid volume fraction of 0.55.

The viscosity ratio of the suspensions is computed as for strain rates up to $\dot{\gamma} = 180\ s^{-1}$, and is plotted along with the resultant viscous number in Fig. 4.8.

The simulation results show that, for sufficiently dense particle suspensions, generally a strongly shear thinning rheology is observed, while the less dense model with a solid volume fraction of 20% did not exhibit much shear dependence. However, it is interesting that at low strain rate range, shear-thickening rheology is exhibited by both models. Similar behaviour is also reported by Johnson et al. [157], in whose study shear-thickening was observed when the applied shear stress was less than $10kPa$ in dense particle suspensions at $\phi = 0.45$ and $\phi = 0.53$. Their results are qualitatively consistent with the LBM-DEM results where the effective shear stress is below $17kPa$ for the shear-thickening region. It is, however, difficult to find quantitative explanations for this behaviour in the literature.

To further investigate such behaviour exhibited by the suspension models, the hydrodynamic and mechanical contributions to the friction coefficient were computed and plotted in Fig. 4.9. Generally speaking, the curves of the hydrodynamic contribution, F^{hydro}, are consistent with those of the viscous number. In regards to the mechanical contribution F^{mech}, it is roughly a constant for $\phi = 0.20$. However, dramatic increase is observed for $\phi = 0.55$ at the beginning of the shearing process, if the models are considered as a continuous test in which the strain rate keeps increasing. Based on the understanding of the author, it is likely that under low shear stresses, the distance between particles decreases, which results in a *consolidated* effect in the suspension, thus increasing the effective viscosity. In other words, the fluid between the particles is extruded at the beginning of the shearing, which weakens the lubrication effect and increases the friction between particles. When the applied shear stress exceeds a certain threshold which can be characterised by the contact stiffness of the particles, the structure of the suspension would quickly collapse, which leads to a shear-thinning rheology.

When looking at the variation of viscous number against strain rate, which is presented in Fig. 4.10, it is clearly shown that the viscous number changes greatly at low strain rates in the Stokesian regime. At these low

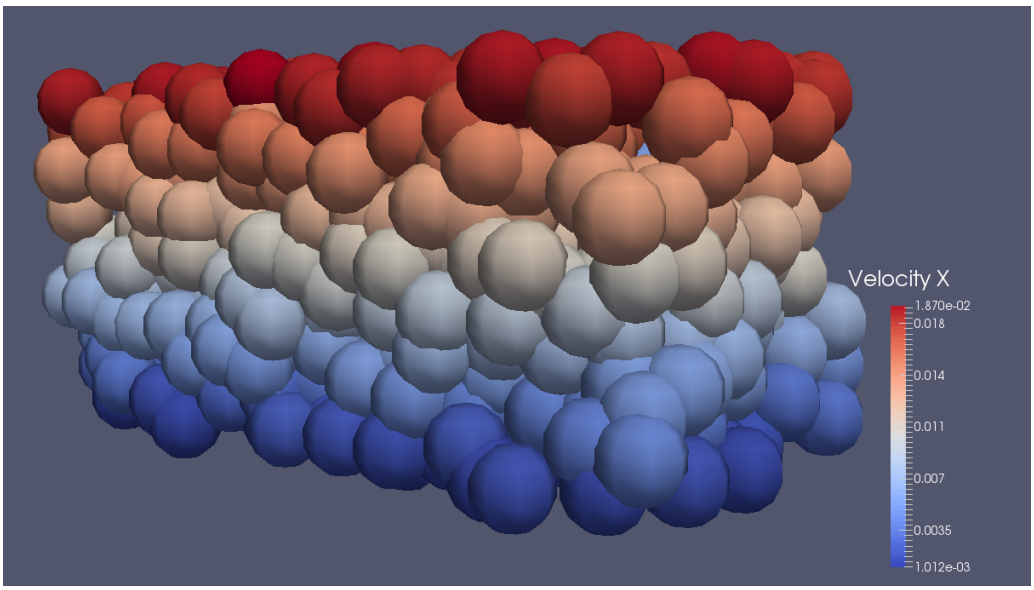

(a)

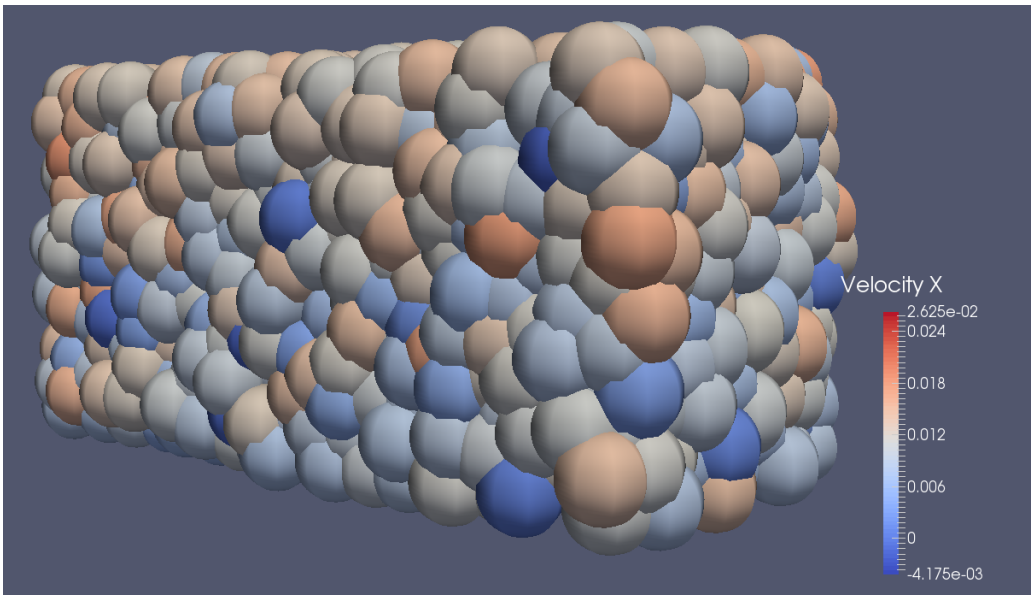

(b)

Figure 4.7: Velocity contour of particle suspensions at (a) $\phi = 0.20$ and (b) $\phi = 0.55$.

strain rates, the high solid volume fraction model is dominated by normal stresses, where the opposite is true for the low solid volume fraction case. Both models tend to approach an asymptotic limit as the strain rate is increased.

It can be observed that the empirical equations fail to capture the relationship between the viscous number and strain rate. In the high particle concentration case, however, there is an intercept between the LBM-DEM results and the empirical expressions. It is expected that the shear rate at these intercepts is representative of the shear rates applied during the experiments of Boyer et al. [128] and Phillips et al. [126].

4.3.6 Duplication of the Experimental Conditions

So far, the results show that the LBM-DEM approach achieved the greatest agreement with the expression proposed by Morris and Boulay among the three semi-empirical expressions. While there is qualitative agreement

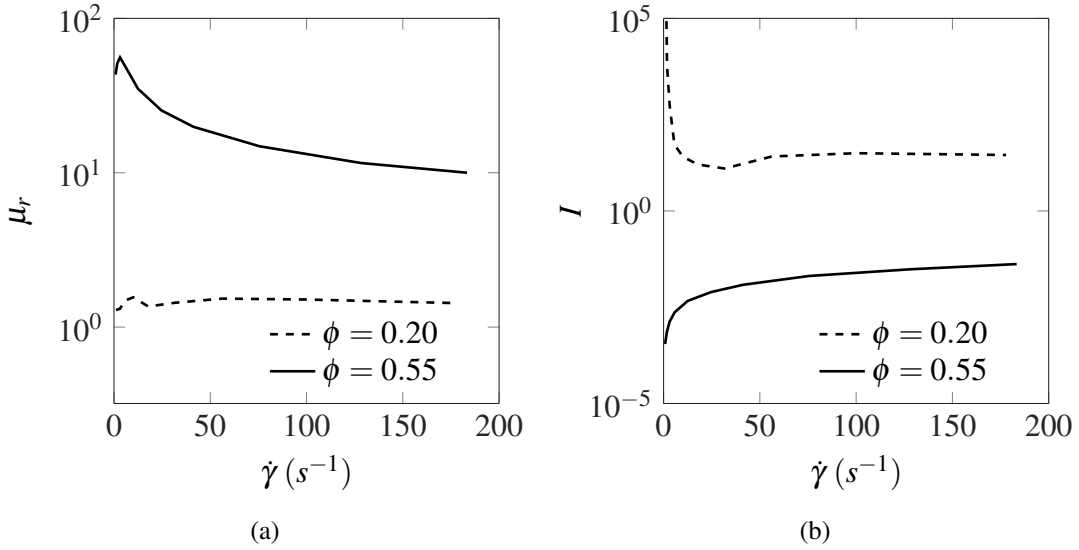

Figure 4.8: Shear dependence of (a) viscosity ratio and (b) viscous number.

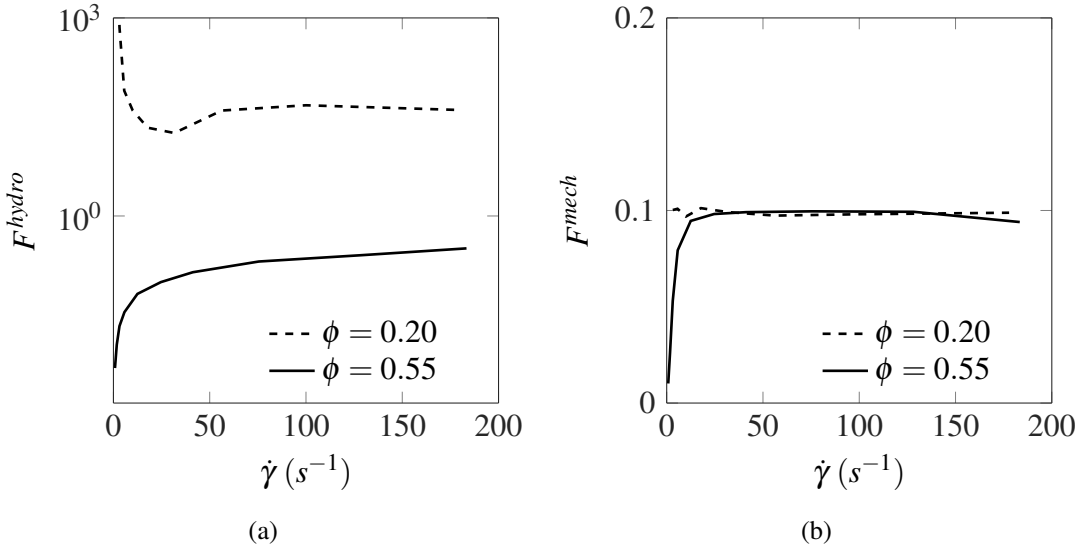

Figure 4.9: Hydrodynamic and mechanical contributions to the friction coefficient in shear-dependent flow models.

with the experimental results of Boyer et al., quantitative agreement is only achieved in the hydrodynamic contribution to the friction coefficient which is shown in Fig. 4.6(a). To resolve the difference between the numerical model and the empirical expression proposed by Boyer et al., the geometry of the experimental rheometer needs to be properly replicated, whose schematic diagram is shown in Fig 4.11.

The most significant difference between the numerical model (shown in Fig. 4.1 and the rheometer used by Boyer et al. is the steel bars attached to the top platen of the rheometer, which make the platen surface non-smooth. As a result, it can also be determined from Fig. 4.6(b) that the mechanical contribution computed by Boyer et al. is much larger than the results from Morris and Boulay.

To address the roughness difference in platen surfaces and better capture the experimental phenomena, the DEM friction coefficient, F^{DEM}, which was 0.1 in the previous models, was increased to 0.5 to mimic the textured platen. The results for viscosity ratio are plotted in Fig. 4.12, with the BGK results included for comparison. Note that the results presented in this section are obtained under strain rate control where $\dot{\gamma} = 150$

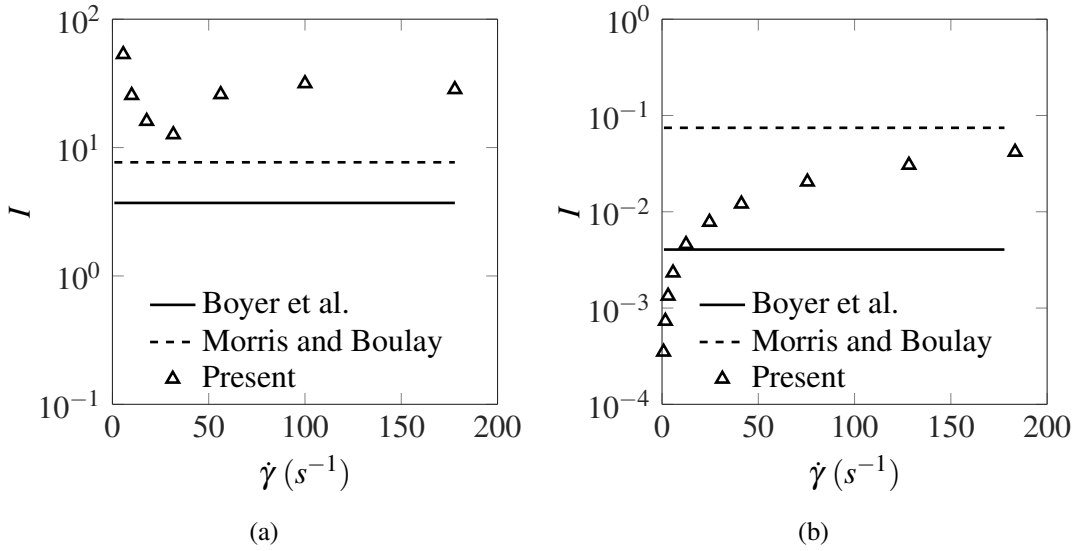

Figure 4.10: Shear dependence of the viscous number compared to semi-empirical expressions at (a) $\phi = 0.20$ and (b) $\phi = 0.55$.

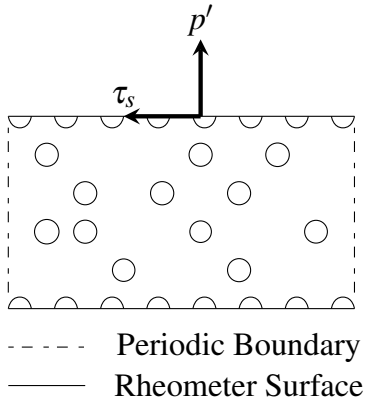

Figure 4.11: A schematic diagram of the rheometer used by Boyer et al..

s^{-1}.

With the increase of F^{DEM}, an improved agreement has been exhibited by both the TRT and BGK collision operators. As expected, the TRT results are of better accuracy over the BGK results. Quantitative agreement is achieved up to a very dense solid volume fraction of $\phi = 0.65$, which is a result that is rarely seen in the literature.

For further validation of the improved numerical model, the relationship between the viscous number and friction coefficient was investigated, which is shown in Fig. 4.13(a). Comparing to the results in Fig. 4.5(b), an improved agreement is again obtained with a DEM contact friction coefficient of $F^{DEM} = 0.5$.

As with the previous modelling results, the contributions of hydrodynamic and mechanical stresses to the friction coefficient have been computed and are shown in Fig. 4.14. Unlike the previous results where a decrease of platen velocity was present with high solid volume fractions, the mechanical contribution is a constant under strain rate control where a constant velocity is applied to the platen. Much like the previous results, the hydrodynamic contribution is in excellent agreement with the semi-empirical equations across the entire range of solid volume fractions tested. The mechanical contribution is very close to the DEM contact friction coefficient applied in the model and valued at 0.5.

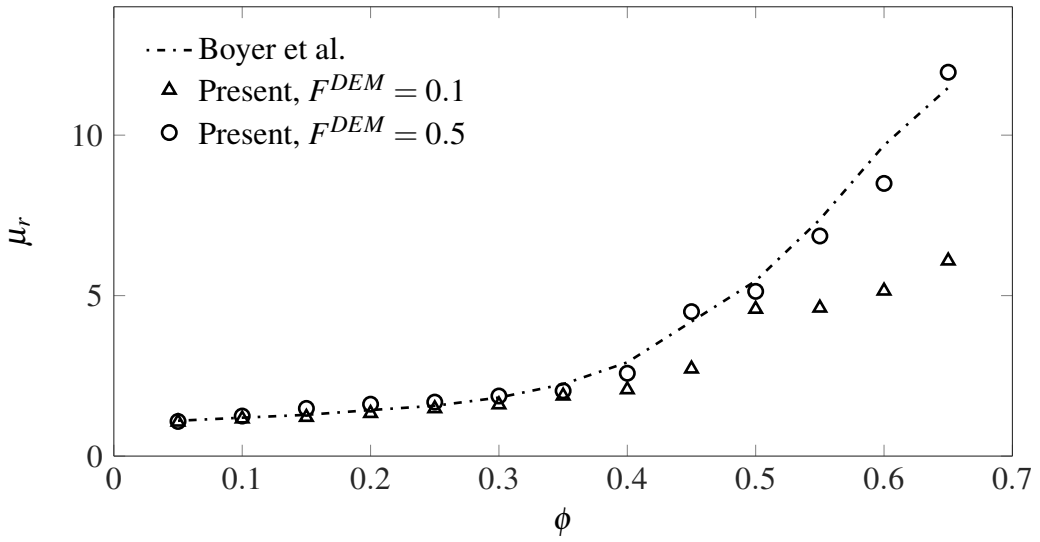

(a)

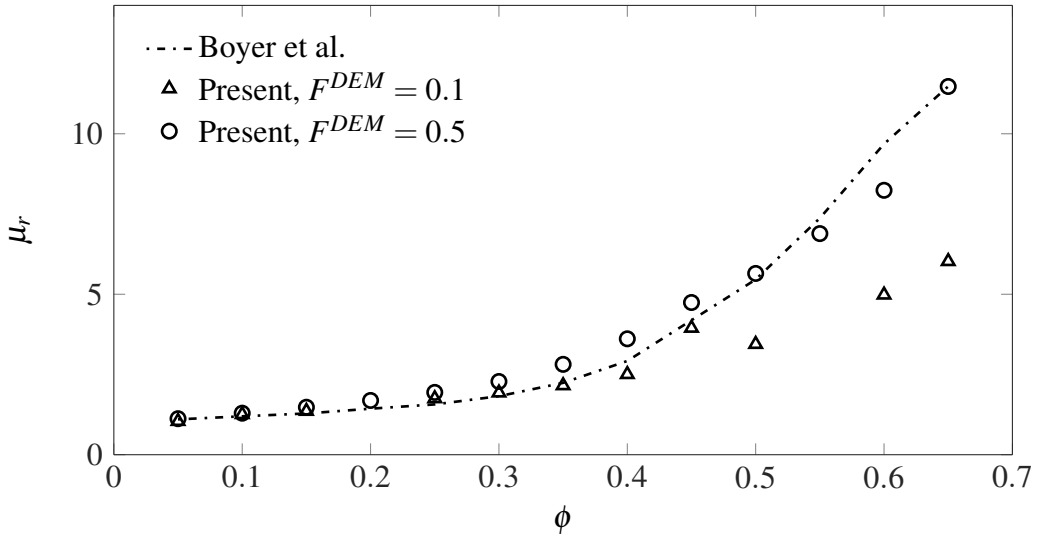

(b)

Figure 4.12: Solid volume fraction against viscosity ratio using (a) TRT and (b) BGK.

4.4 Summary

This chapter has presented the application of the improve LBM-DEM coupling approach in numerical modelling of dense particle suspensions. A periodic shear cell rheometer was used to compare the coupled LBM-DEM model to the empirical expressions for suspension viscosity. Discrete element particles were packed into a cubic lattice Boltzmann domain which was periodic in the lateral directions. Using either shear stress or strain rate control, the numerical model was used to simulate the shearing of the particulate suspension. The resultant hydrodynamic and mechanical forces on the shearing plane were recovered once the model had reached steady state, where these results were used to compute the effective suspension viscosity.

The results from this analysis were validated against existing empirical expressions. It was found that the LBM-DEM model reached a packing limit between 0.60 and 0.65, which is a result that is rarely seen in the literature. In addition, it was also found that the viscous number, I, was not only a function of the solid volume fraction, but also depended on the shearing of the suspensions. Later in the shearing test, the numerical model exhibited shear thickening under low shear stress, while exhibiting shear-thinning under high shear stress, at high

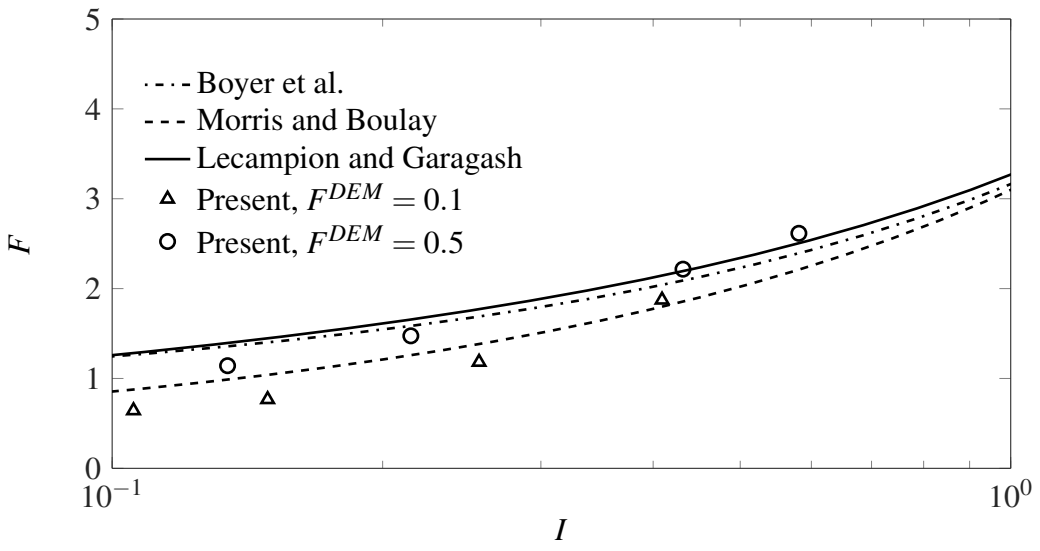

(a)

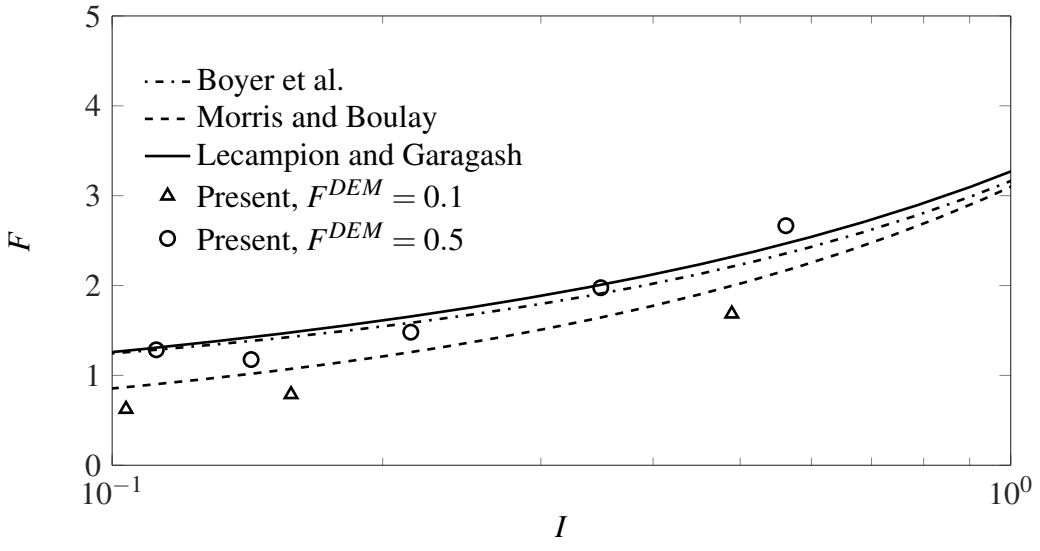

(b)

Figure 4.13: Viscous number against friction coefficient using (a) TRT and (b) BGK.

solid volume fractions. Additionally, the coupled LBM-DEM framework presented a means of investigating the dominant micromechanical features of the suspensions, as the hydrodynamic and mechanical forces could be calculated separately in the computational model.

This study provides good understandings of the suspension flows by investigating several parameters including solid volume fraction and shear rate. Furthermore, these observations can be used to characterise the macroscopic behaviour of fracking fluids, which demonstrates the potential for large-scale modelling of hydraulic fracturing.

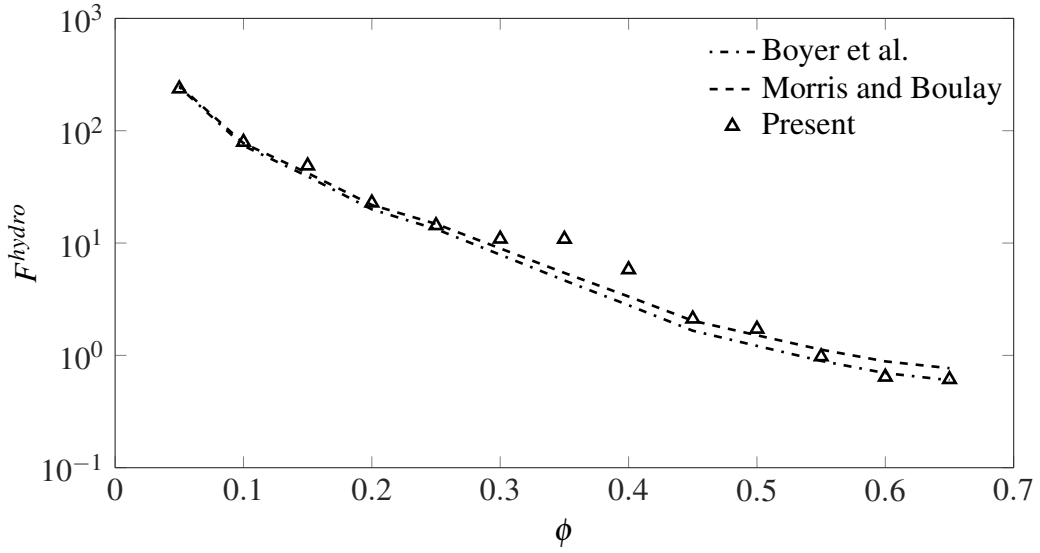

(a)

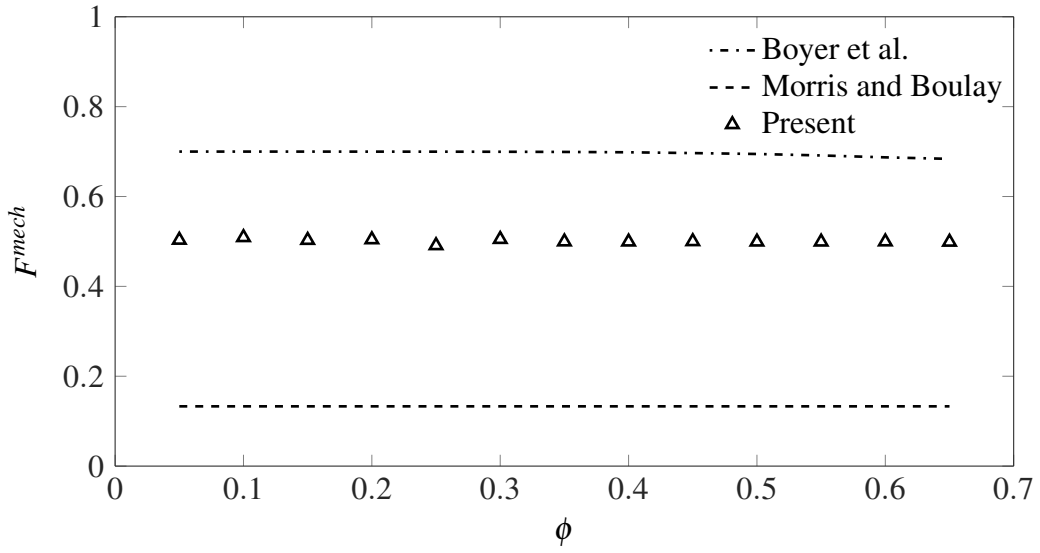

(b)

Figure 4.14: Solid volume fraction against viscosity ratio under strain rate control with a DEM contact friction coefficient of $F^{DEM} = 0.5$ using (a) TRT and (b) BGK.

Chapter 5

Numerical Modelling of Fluid Flow Around Proppant in Hydraulic Fractures

Hydraulic fracturing aims to create high-conductivity fractures in formations to improve the recovery efficiency of energy resources such as oil and gas. However, the fracture conductivity can be reduced significantly by various factors such as proppant embedment, proppant breakage, residual fracture fluid, and long-term creeping deformation of the formations. Proppant embedment occurs when proppant penetrates into the reservoir formation due to the closure stress following the fracking operation, which leads to a decrease of fracture aperture and significant conductivity loss, especially for the weakly consolidated sandstones and coalbeds. Proppant embedment can result in a reduction of 10 to 60% in the fracture width with subsequent reduction of productivity from oil and gas wells in weakly consolidated sandstone, while a 20% reduction in the fracture width may lead to an approximately 50% decrease in fluid flow and recovery [158]. Consequently, it is important to understand and model proppant embedment as it significantly affects the fracture conductivity as well as the overall production from the hydraulic fracturing stimulation.

In this chapter, recent studies on the theoretical models for proppant embedment and fracture conductivity will be comprehensively reviewed. The LBM model is firstly implemented to replicate the case where the Hertz contact model is used to characterise the elastic contact between fracture walls and proppant. The fracture permeability diagram is generated to analyse the impact of proppant embedment on fracture permeability reduction under different stress conditions. Following that, the implemented computational model is then applied to evaluate the fracture permeability under the influence of proppant embedment. To assist with this part of study, *Elfen*, which is an advanced finite element-discrete element package developed by Rockfield Software Ltd., is used for geometry generation of propped fractures. The fracture permeability results are then applied to the mathematical model proposed by [159] for well productivity prediction.

5.1 Review of Studies on Fracture Conductivity

Numerous studies can be found in the literature regarding proppant embedment and fracture conductivity. Among the earliest studies, Darin and Huitt [160] conducted an experiment to study the conductivity of propped fractures by assuming that the proppant particles were uniformly embedded in the fractures. Their results showed

that the conductivity of the fracture with a partial monolayer of a single large-size proppant was much higher than the fracture with a proppant pack. A numerical model of the fracture conductivity was then derived by modifying the Kozeny-Carman equation. However, this study was based on the assumption that the single, large-size proppant was able to sustain the confining stress, which is not realistic in many industrial operations. In the early 1980's, Volk et al. [161] investigated various factors which affect proppant embedment including proppant size, proppant concentration and distribution, rock type and fracture surface, and proposed empirical equations based on experiment data. Lacy et al. [158] developed a new computer-controlled laboratory approach to study propped fracture aperture and proppant embedment in weakly consolidated formations by taking water saturation and gelled fluid leak-off into consideration. Besides the factors mentioned above, multilayer proppant embedment was also investigated, where water saturation and formation cementation disintegration had critical impact. In a recent study, Alramahi & Sundberg [162] developed a numerical model to calculate the conductivity loss in normalised fracture as a function of the closure stress, where the fracture aperture data was taken directly from the experimental results. The relationship between proppant embedment and the Young's modulus of the formation was also investigated, which allowed for an optimised selection of completion zones in shale gas or oil formations.

Li et al. [163] derived a series of analytical models to calculate proppant embedment, proppant deformation, the change in fracture aperture and fracture conductivity, with several assumptions including a homogeneous fracture surface, even proppant paving in the fracture, a linear elastic model, and uniform proppant size distribution. Both single-layer and multi-layer embedment patterns, which are illustrated in Fig. 5.1, were simulated and analysed.

For the single-layer embedment model (Fig. 5.1(a)), the embedment depth, d, is calculated as,

$$d = \frac{\left(\frac{3}{8}Pr_s\right)^{2/3}}{r_s}\left[2\left(C_1+C_2\right)^{2/3} - \left(2C_1\right)^{2/3} - \left(2C_2\right)^{2/3}\right], \tag{5.1}$$

where P is the contact force between the proppant and coalbed, r_s is the proppant radius, ν and E are the Poisson's ratio and elastic modulus of the proppant and coalbed. Two parameters, C_1 and C_2 are defined as,

$$C_1 = \frac{1-\nu_1^2}{E_1}, \tag{5.2}$$

and,

$$C_2 = \frac{1-\nu_2^2}{E_2}. \tag{5.3}$$

The embedment depth for the multi-layer embedment model (Fig, 5.1(b)) can be computed as,

$$d = b_0 + b_1\left\{1.04h\left(H^2\sigma_0\right)^{2/3}\left[\left(C_1+C_2\right)^{2/3} - \left(C_1\right)^{2/3}\right] + D\frac{\sigma_0}{E_2}\right\}, \tag{5.4}$$

in which b_0 and b_1 are correction factors that can be obtained by fitting with the experimental data, h denotes the fracture aperture, H is a dimensionless distance coefficient, D is the thickness of the coalbed which is by assumption identical for the both sides, and σ_0 is the confining stress.

Consequently, a theoretical model for the evaluation of fracture conductivity was derived by Li et al. [163], which is written as,

$$K_f = \frac{C_0 f_1\left(f_1 - 0.74\right)\left(hf_1 - 2r_s f_2 - 2D\frac{\sigma_0 C_2}{1-\nu_2^2}\right)}{0.5f_1^2}D_1^2, \tag{5.5}$$

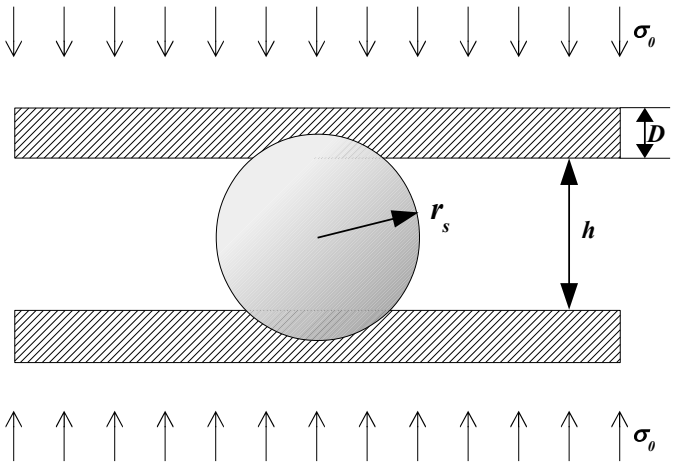

(a)

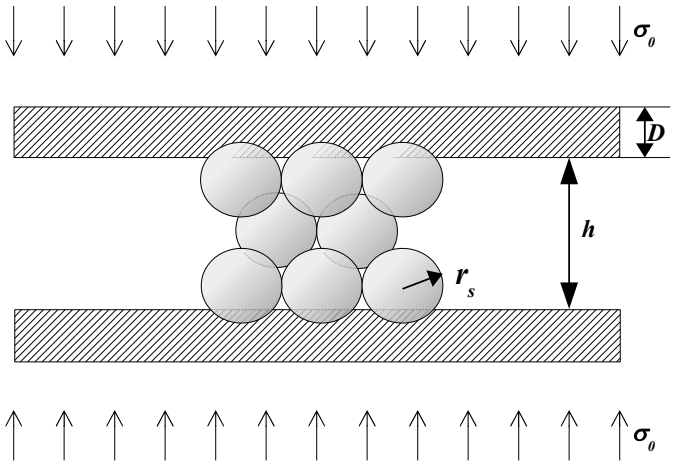

(b)

Figure 5.1: Schematic diagrams of numerical models of proppant embedment in coalbeds with (a) single-layer proppant and (b) multi-layer proppant.

in which the two parameters, f_1 and f_2 are calculated as,

$$f_1 = 1 - 2.08\,(\sigma_0 C_1)^{2/3}, \tag{5.6}$$

and,

$$f_2 = 2.08\,(\sigma_0 C_1 + \sigma_0 C_2)^{2/3} - 2.08\,(\sigma_0 C_1)^{2/3}. \tag{5.7}$$

This model indicates that the proppant embedment increases with the closure pressure, the proppant diameter and the elastic modulus of the proppant, and decreases with the elastic modulus of the coalbed. The fracture conductivity increases with the proppant diameter, the initial fracture aperture and the elastic modulus of the coalbed and proppant, and decreases with the closure pressure.

Recently, Hou et al. [164] improved the analytical models proposed by Li et al. [163] by incorporating the creeping deformation of the rock using the Kelvin-Voigt model. The results of the analytical models agreed with the experimental data, highlighting the significance of the proppant distribution pattern in the fractures. The heterogeneous proppant placement was shown to result in higher fracture conductivity than the uniform proppant distribution at low closure pressures. However, there exists a certain threshold pressure which is determined by the proppant concentration, and opposite results can be obtained when exceeding the threshold pressure.

However, experimental studies and semi-empirical models have certain limitations and may not be suitable for calculating fracture conductivity due to lack of generalisation. It is of great importance to develop effective and accurate models to analyse fracture conductivity.

As the power of computers has grown, notable progress has been witnessed during the past decade in the numerical modelling of proppant embedment and fracture conductivity. Zhang et al. [165] demonstrated experimental and numerical studies to understand the impact of excessive proppant embedment on fracture conductivity in shale. Their experiments were conducted using Barnett shale samples with representative rock properties. The damage process was simulated in the laboratory by flowing water through the propped shale fractures. Experimental results showed that the shale fracture surface softening after its exposure to water caused a loss of up to 88% of the undamaged fracture conductivity, and the average embedment depth was larger when exposed to water than those when exposed to gas. A computational fluid dynamics (CFD) model was also implemented by Zhang et al. [165] to quantify the conductivity loss due to proppant embedment using the finite volume method to solve the 3D Navier-Stokes equations. The CFD results showed that the first 10% of proppant embedment volume could cause a conductivity reduction of 45 to 80% of the undamaged fracture conductivity. With the same proppant volume loss due to embedment, the conductivity reduction was less in fractures with multi-layer proppant, where the fracture conductivity depended more on the internal proppant rather than the flow area adjacent to the fracture surface. Fracture propped by a monolayer of proppant experienced severe conductivity loss due to large loss of flow area.

In another study, Zhang et al. [166] developed a new model which coupled the discrete element method (DEM) to the CFD. In the developed model, the mechanical interaction between the proppant and fracture surface was characterised by the DEM, and the fluid flow through proppant pack was modelled by the coupled DEM-CFD. The fluid domain was discretised into rectangular fluid cells with several fluid particles involved. The driving force acting on the fluid was then applied to those fluid particles to generate the fluid flow. The DEM-CFD framework was validated by the Kozeny-Carman equation and laboratory studies. The results showed that the fracture conductivity increased with the proppant concentration and proppant size, and decreased with the closure stress and the degree of formation hydration which caused surface softening and proppant embedment. The main drawback of this approach is that the coarse grid resolution of the fluid discretisation cannot provide pore-scale understanding of the proppant embedment, which constraints the accuracy of the modelling.

In many studies, the Hertz contact model is commonly used to model the proppant-fracture interaction. For example, Zheng et al. [167] used the Hertz contact theory to calculate the fracture aperture. An analytical expression of the fracture permeability was also derived based on the Kozeny-Carman equation. They applied the model to investigate the effects of proppant distribution density and proppant pillar radius on the fracture conductivity. Their results indicated that the fracture conductivity increased at first and then decreased rapidly with the proppant distribution density. The conductivity factor reached the maximum value when the vertical pillar spacing was equal to the horizontal spacing. In another study, Chen et al. [168] applied a transformed Hertz

contact model with a power law model to the characterisation of proppant embedment and fracture deformation. In this model, the effective stress and the embedment depth formed a power law relationship based on the Oliver-Pharr indentation. A theoretical model for the permeability reduction was also derived. The results showed that the power law relationship could better fit the experimental data, especially when the conventional Hertz contact model became invalid in the cases where the embedment was large compared to the proppant size.

Besides the factors mentioned above, other factors which affect the proppant embedment and fracture conductivity have also been investigated by researchers. Mueller et al. [169] studied the impact of fracture surface hardness on proppant embedment. They concluded that the interaction between the fracking fluid and fracture surface led to a reduction in surface hardness and therefore resulting in an increase in the embedment depth. In the same study, a representative 20/40 mesh sand was used in numerical modelling to compare two different types of proppant size distribution (i.e. the normal size distribution and the uniform size distribution). Results showed that proppant size distribution had a significant impact on the fracture conductivity loss. The normal size distribution resulted in larger displacement of the fracture surface, which consequently led to larger reduction in fracture conductivity than the uniform size distribution. In another study, Zhang et al. [170, 171] investigated the performance of surface modification treated (SMA) proppant. Analytical models were derived to compute the SMA treated proppant embedment and fracture conductivity, with a visco-elastic Kelvin-Voigt creeping deformation model incorporated in the models. Their results showed that when comparing to regular proppant, the SMA treated proppant effectively reduced proppant deformation and embedment and thus benefited fracture conductivity. However, it was also found that the SMA treated proppant required longer time for the fracture conductivity to reach steady state than regular proppant, which may affect the economic benefit and efficacy of the hydraulic fracturing operation.

In a most recent study, Tang et al. [172] demonstrated experimental and numerical evaluations to study the proppant embedment at varying proppant coverage (i.e. the proppant covered area divided by the total cross-section area of the sample). The experiment was set up using the Mount White sandstone rock formation which was collected from New South Wales, Australia. The collected blocks were then cored into cylinders with 54mm diameter and 30mm height. A ceramic proppant used in the experiments, being one of the most commonly used types of proppant. In the numerical model, the PARTICLE Flow Code 2D (PFC2D) was applied using the discrete element method module. Their results showed that proppant embedment reduced with the proppant concentration, and eventually reached steady state after 150% proppant coverage. It was explained that the extra half layer of proppant helped make up the remaining space caused by particle movement to achieve a fully covered proppant monolayer. Therefore, 150% coverage was thought to be the optimal proppant concentration when considering the influence of proppant embedment. In addition, at high proppant coverage, greater proppant embedment was observed for water-saturated fluid than oil-saturated fluid.

Proppant embedment as well as fines generation were recently observed and reported for two coals from the Cooper Basin, Australia, based on laboratory conductivity cell testing [173]. They found that embedment decreased with increasing coal rank (i.e. a proxy for hardness) and increased sphericity of the proppant used. Finally, reduced fines migration generated from embedment was observed when smaller versus larger diameter proppant (i.e. $30/50$ vs. $20/40$ mesh) was used in the testing.

5.2 Replication of Fracture Permeability Modelling

The implemented TRT-PSM framework was firstly applied to replicate the fracture permeability analysis, where Khanna et al. [174] used the CFD package of *ANSYS* to mimic the fluid flow through propped hydraulic fractures. In this study, a simplified theoretical model was considered, in which the fracture deformation was elastic and was governed by Hertz contact theory. With certain functions characterising the shape of the deformed fractures, these functions were directly imported into the LBM code to generate the fracture boundaries and then mapped to the underlying lattice of the LBM domain. No finite element modelling was required for the models shown in this section.

Additionally, assumptions were made to further simply the modelling, which include uniform proppant distribution within the fracture and a disregard of the coalbed cracking mechanism. These assumptions strictly limited the applicability of the computational model. Nevertheless, this study was suitable as a benchmark problem which could provide insight on proppant embedment and fracture conductivity loss. In the end, a rough estimation of the optimal proppant concentration is presented, highlighting the influence of proppant concentration on fracture permeability.

5.2.1 Elastic Deformation of the Propped Fracture

A schematic diagram of the propped fracture in the x-z plane is illustrated in Fig. 5.2. A remote confining stress, σ_0, is applied to this elastic space, which induces deformation of the fracture and squeezes the rigid particle inside the fracture. The particles are assumed to be uniformly distributed across this monolayer such that the distance between the adjacent particles equals to L. u_z is the deformation of the fracture surface in the z-direction and h is the fracture aperture.

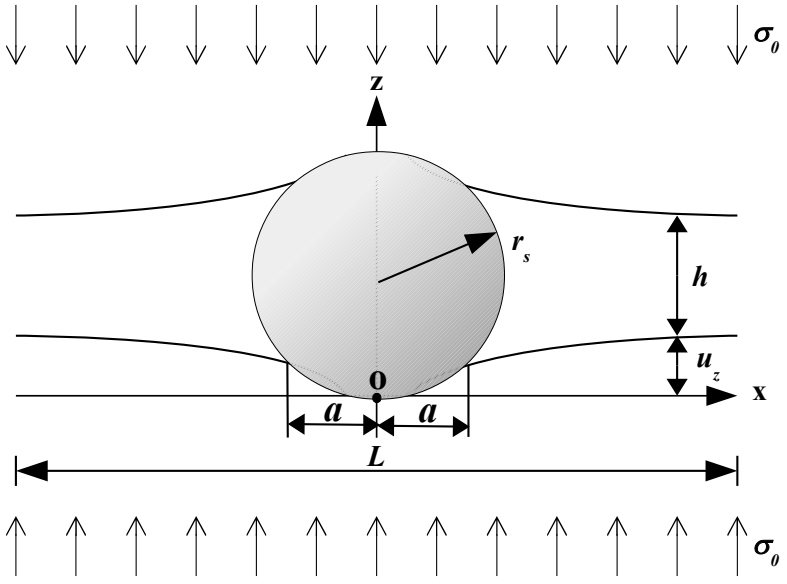

Figure 5.2: Elastic deformation of the propped fracture.

Solutions to the geometry of this elastic contact model are available in the literature (more details can be found in Ref. [175] for details). The radius of the contact zone, a, is calculated as,

$$a^3 = \frac{3}{4}\frac{\left(1-\nu^2\right)\sigma_0}{E} r_s L^2, \tag{5.8}$$

where r_s is the radius of the particle, ν is the Poisson's ratio and E is the elastic modulus of the coal material. The resultant displacement of the fracture surface is computed as,

$$u_0(r) = -\frac{\left(2a^2 - r^2\right)}{2r_s}, \tag{5.9a}$$

for $r \leq a$ and,

$$u_0(r) = -\frac{1}{\pi r_s}\left[\left(2a^2 - r^2\right) sin^{-1}\frac{a}{r} + r^2\frac{a}{r}\left(1-\frac{a^2}{r^2}\right)^{1/2}\right], \tag{5.9b}$$

for $r > a$, where r is the distance from the observation point to the contact point $\mathbf{o}$.

However, besides u_0, other neighbouring particles within the fracture also have an impact on the displacement of the observation point (x,y). Under these circumstances, a region with a radius of R in the propped fracture is taken into account, which is shown in Fig. 5.3. The highlighted region with a side length of L is called a *symmetry element* which indicates the computational domain of the model.

The distance between point (x,y) and a neighbouring particle (iL, jL) is computed as,

$$r_{ij} = \sqrt{(iL-x)^2 + (jL-y)^2}, \tag{5.10}$$

where i and j are, respectively, the particle number in the x- and y-direction.

Substituting Eq. (5.10) into Eq. (5.9), the displacement at point (x,y) due to particle (iL, jL) can be obtained. Hence, the cumulative displacement at point (x,y) due to all the particles within the region of radius R is summarised as,

$$u_1 = \sum_i \sum_j u_0(r_{ij}) H(R - r_{ij}), \tag{5.11}$$

in which H is the Heaviside step function. Additionally, the resultant vertical displacement of the fracture surface is characterised by the elliptic integral which is given as,

$$u_2 = \frac{4}{\pi}\frac{\left(1-\nu^2\right)\sigma_0}{E} R \int_0^{\pi/2} \sqrt{1 - \frac{x^2+y^2}{R^2} sin^2\theta}\, d\theta. \tag{5.12}$$

Consequently, the total vertical displacement of the fracture surface at (x,y) can be computed by adding Eq. (5.11) and Eq. (5.12),

$$u_z(x,y) = u_1 + u_2, \tag{5.13}$$

and the fracture aperture at (x,y) is calculated as,

$$h(x,y) = 2\left(r_s - u_z(x,y)\right). \tag{5.14}$$

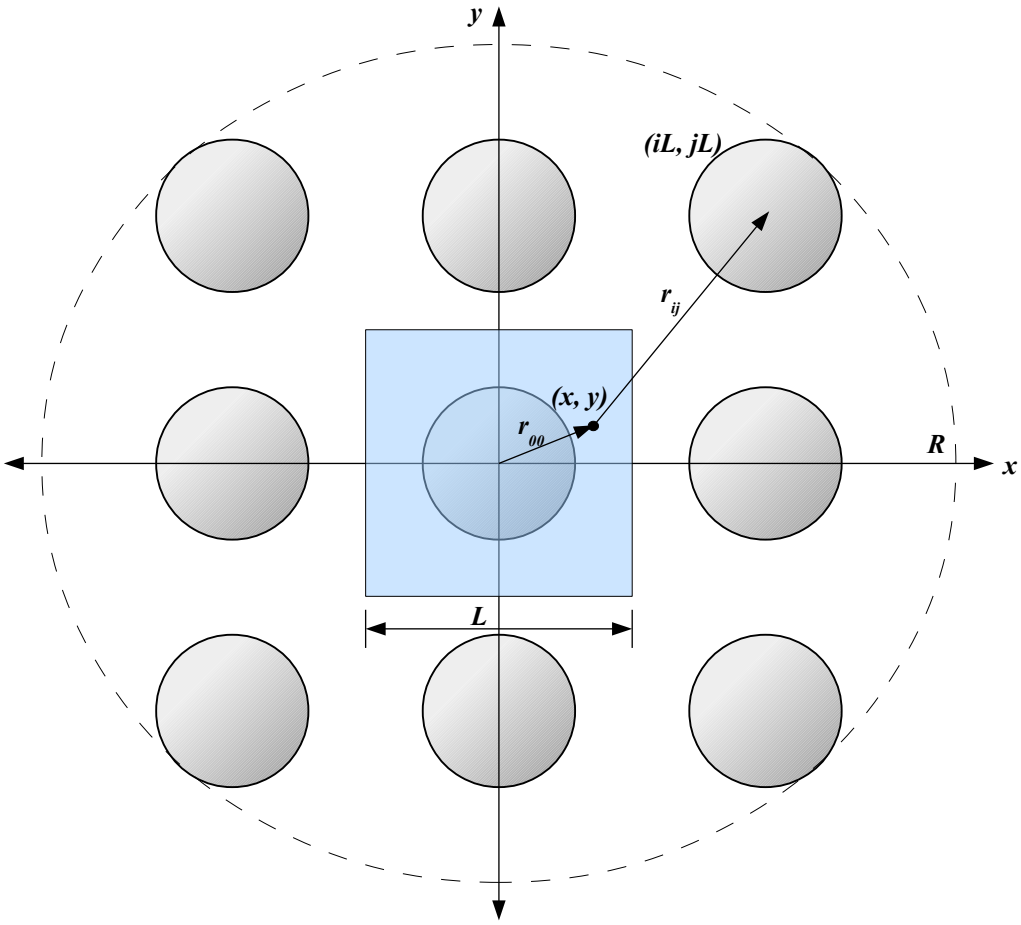

Figure 5.3: The impact of the neighbouring proppant within the monolayer on fracture deformation at point (x,y).

Eq. (5.14) was implemented in the computational model to generate the fracture opening profile. The TRT-PSM kernel was then used to solve the fluid flow through the deformed fracture and to accurately capture the shape of the fracture surfaces.

5.2.2 Numerical Modelling of Fracture Permeability

The purpose of this modelling was to investigate the dependence of fracture permeability on proppant concentration. It can be observed from Eq. (5.8) and Eq. (5.13) that for any given proppant size (r_s) and spacing (L), the fracture opening profile $h(x,y)$ only depends on the remote confining stress, σ_0, and material properties of the coal (i.e. the Poisson's ratio, ν, and the elastic modulus, E). To simplify the analysis, the affecting factors were combined into one single parameter which was referred to as the dimensionless stress σ_d and was calculated as,

$$\sigma_d = \frac{\left(1-\nu^2\right)\sigma_0}{E}, \tag{5.15}$$

to account for different stress conditions in these simulations.

The proppant radius r_s was kept a constant for all cases that were simulated. The length of the computational domain was equal to the particle spacing, L. The change in particle concentration was facilitated by changing

ρ_p	$\sigma_d = 10^{-3}$	Δx	$\sigma_d = 10^{-2}$	Δx
0.057	0.044811	0.02	N/A	N/A
0.067	0.036679	0.02	N/A	N/A
0.1	0.021210	0.02	N/A	N/A
0.167	0.010621	0.02	0.045460	0.02
0.2	0.008293	0.02	0.033351	0.02
0.25	0.006125	0.04	0.025873	0.02
0.3	0.004715	0.04	0.019609	0.02
0.35	0.003769	0.04	0.015708	0.02
0.4	0.003230	0.04	0.013245	0.04
0.5	0.002381	0.04	0.009778	0.04
0.6	0.001815	0.1	0.007380	0.04
0.67	0.001606	0.1	0.006501	0.04
0.8	0.001237	0.1	0.004953	0.04
1	0.000920	0.1	0.003637	0.05

Table 5.1: Maximum elastic displacement (*mm*) of the fracture surface and the corresponding Δx (*mm*) for varying particle concentration.

the particle spacing, L, which then controlled the particle aspect ratio, ρ_p. This was calculated as,

$$\rho_p = \frac{2r_s}{L}. \tag{5.16}$$

Periodic boundary conditions were applied to the lateral faces of the computational domain. Since the normalised permeability, rather than the actual permeability value, was of interest, r_s was set as a unit length of $1mm$ for simplicity, thus making the original fracture aperture $2mm$. A body force, $\mathbf{G}$, was applied to the fluid domain to drive the flow. The fluid viscosity was also set to be unit value. To ensure the numerical accuracy and stability of the simulations, the Mach number was kept below 10^{-2} to ensure a laminar flow condition and the Reynolds number is of the order of 10^{-2} for all cases.

Fig. 5.4 illustrates a cross-section view of a simulation domain under a dimensionless confining stress of $\sigma_d = 10^{-2}$ for $\rho_p = 0.2$. It can be observed that substantial elastic deformation was caused by the remote confining stress, resulting in an approximately 33% reduction of the initial fracture aperture. A summary of the maximum displacement of the fracture surface, $u_{z,max}$, is listed in Table 5.1. As expected, the maximum displacement increased with the increase of remote confining stress and with the decrease of normalised particle concentration. At $\rho_p = 0.057$, 0.067 and 0.1, the computed $u_{z,max}$ using Eq. (5.13) exceeded the radius of the proppant, which indicated that the fracture is completely shut. Note that the listed data is the displacement of fracture surface on one side and the total reduction in the fracture aperture needs to be doubled. Under these circumstances, the lattice spacing, Δx, needed to be selected carefully according to the exact displacement in each of the simulation cases to ensure an accurate characterisation of the fracture surface. A summary of Δx in each case is also presented in Table 5.1.

The simulation was kept running until the fluid flow reached steady state. The fracture permeability, K_f, was then calculated using the equation,

$$K_f = \frac{U\mu}{\rho \mathbf{G}}, \tag{5.17}$$

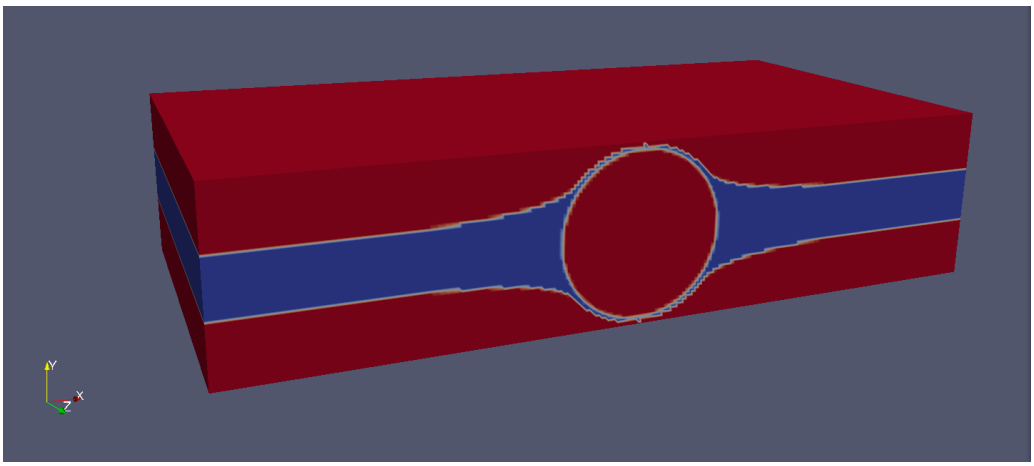

(a)

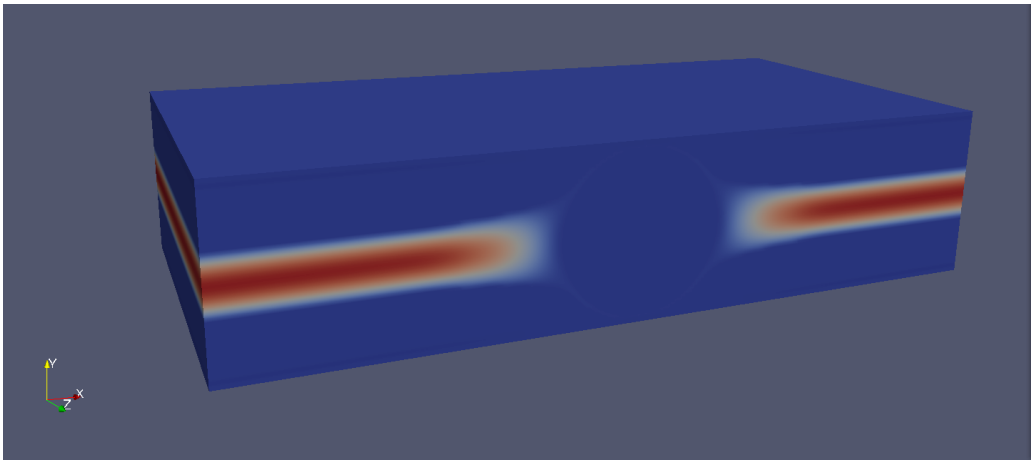

(b)

Figure 5.4: Particle embedment in elastically deformed fracture showing (a) fracture surface deformation with coal and particle shown in red and flow region in blue and (b) flow velocity contour with coal and particle shown in blue and fluid in coloured contours.

where U is the flux across the cross-section area of the fracture. Afterwards, the computed permeability was normalised against the permeability of an open channel whose aperture was equal to the diameter of the proppant $2r_s$.

The computed normalised fracture permeability is plotted in Fig. 5.5, against the normalised particle concentration. The results obtained by Khanna et al. [7] using the CFD package of *ANSYS* were also incorporated for direct comparison. It was shown that the LBM results agreed well with the CFD results. The upper envelope corresponds to zero confining stress, under which no deformation is caused to the fracture surfaces. As expected, the increase in confining stress caused dramatic permeability loss to the fracture. For every given value of the confining stress, there existed a certain range of particle concentration, namely the optimal particle concentration, which led to the maximum fracture permeability. The resultant optimal particle concentration increased with the increase of confining stress. Meanwhile, it was also found that the permeability was more sensitive to the particle concentration around the optimal concentration value than other values. In other words, the slope of the curve was obviously larger near the optimal particle concentration and was smaller when approaching the maximum and minimum particle concentrations. Lower particle concentration was not able to protect the fracture against closure, while higher particle concentration was likely to cause hydraulic resistivity within the fracture. Hence,

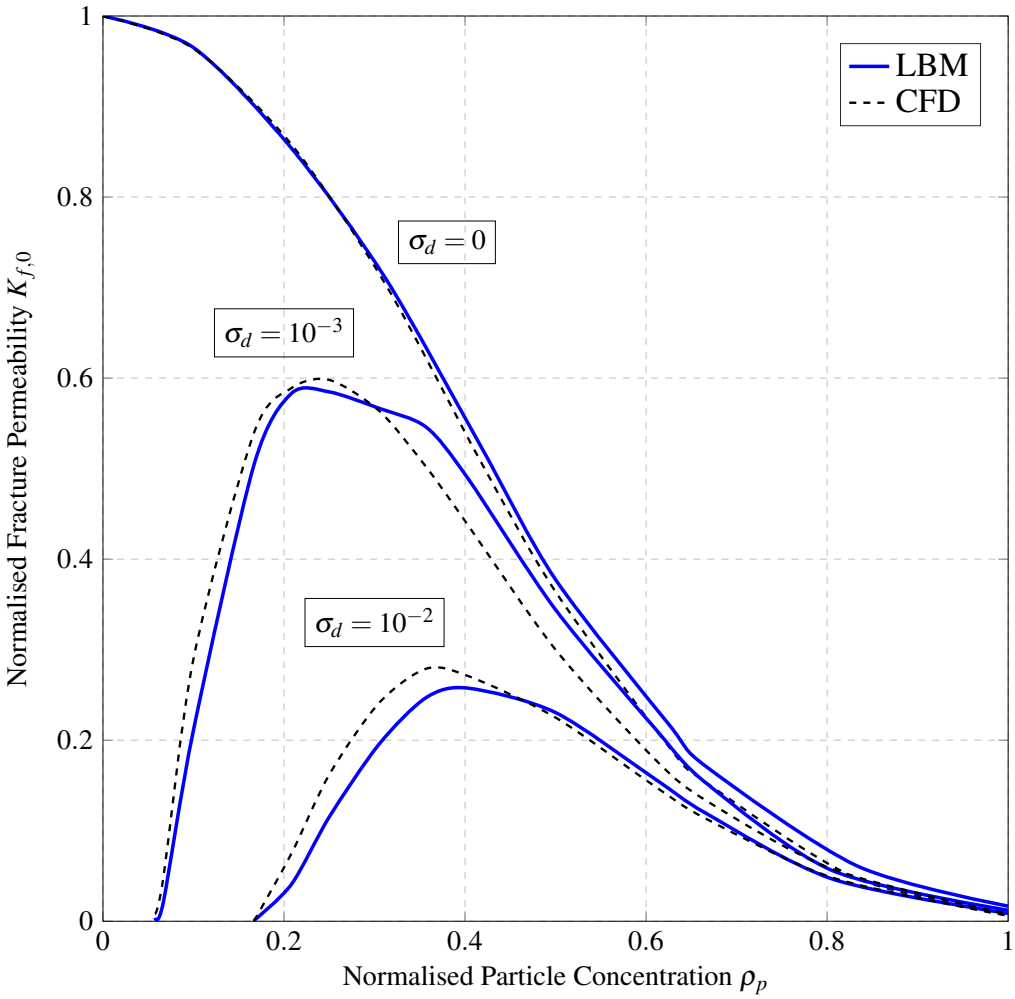

Figure 5.5: Fracture permeability diagram: the normalised fracture permeability against normalised particle concentration under varying dimensionless confining stress, with elastic deformation.

it is significant to use the fracture permeability diagram to predict the ideal proppant concentration at different stress conditions in order to maximise reservoir permeability and oil/gas productivity.

5.3 Numerical Modelling of Fluid Flow in Hydraulic Fractures: Elastoplastic Model

In Section 5.2, a replicated study on fracture permeability, with the Hertz contact theory characterising the interaction between the proppant and fracture surfaces as well as the deformation of the propped fractures, was presented. However, coals are usually recognised as an elastoplastic material. Studies [163, 164] have also shown that proppant will be embedded into coalbeds by a certain depth under remote confining stress, as introduced in Section 5.1. Hence, the elastic model has severe limitations when analysing the efficacy of a hydraulic fracturing treatment in real cases. To improve the reliability and applicability of the proppant embedment model, the fracture permeability modelling was then repeated using an elastoplastic model. In this section, the geometries of deformed fractures were firstly generated using the finite element-discrete element modelling package, *Elfen*, under varying confining stress and particle concentration. The obtained geometries were then imported into

the LBM solver in order to investigate the fluid flow through the propped fractures. Consequently, the optimal particle concentration using the elastoplastic model could be obtained by the use of the fracture permeability diagram similar to Fig. 5.5.

5.3.1 Geometry Generation of the Propped Fractures

Fig. 5.6 graphs the original configuration of an elastoplastic model in *Elfen*, selecting $\rho_p = 0.2$ as an example. In this 2D, axisymmetric model, the proppant radius was kept as a constant of $0.05mm$. Based on the assumption of uniform distribution of particles in the fracture, a single, axisymmetric, unit cell from the propped fracture could be used, substantially improving the computational efficiency. The thickness of the coal was designed to be thick enough to obtain a reasonable geometry of the propped fracture as well as to avoid formation breakage. A loading, which was linearly increasing with time t, was applied to the top surface of the upper coalbed and the bottom of the lower coalbed was constrained. The Young's modulus was set to be $3GPa$ and the Poisson's ratio was 0.3 for the coal material.

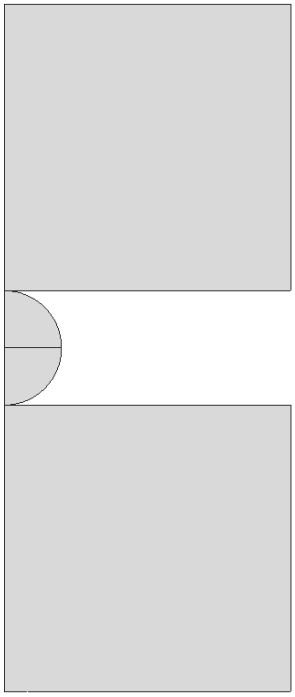

Figure 5.6: The original configuration of a propped fracture model of $\rho_p = 0.2$ in *Elfen*.

The model was run for a total solution time of $10s$, during which the computed dimensionless confining stress using Eq. (5.15) increased from 0 at $t = 0s$, to 10^{-4} at $t = 0.1s$, to 10^{-3} at $t = 1s$, and to 10^{-2} at $t = 10s$. Fig. 5.7 to Fig. 5.16 illustrate the contour plots of vertical displacement of the fracture as well as the proppant embedment mechanism in all simulations from $\rho_p = 0.1$ to $\rho_p = 1.0$, for different stress conditions. The numbers shown in these figures were normalised by 10 times the particle diameter. These figures clearly show the proppant embedment and the reduction of fracture apertures under remote confining stress. Comparing Fig. 5.8(c) with Fig. 5.14(c), and Fig. 5.8(d) with Fig. 5.14(d), it is also shown that lower particle concentration is not able to prevent the fracture against closure, while higher particle concentration can maintain the fracture aperture but meanwhile reduces the effective channel width for fluid flow. In addition, comparing Fig. 5.8(d)

with Fig. 5.4(a), substantial difference can be noticed between the elastic and elastoplastic models with the same particle concentration of $\rho_p = 0.2$, under the same dimensionless confining stress of $\sigma_d = 10^{-2}$. In the elastic model, severe elastic deformation was generated due to remote confining stress, but the maximum deformation was smaller than the proppant radius which maintains an open channel for fluid flow. While in the elastoplastic model, the proppant was fully embedded into coalbeds and the fracture was completely shut.

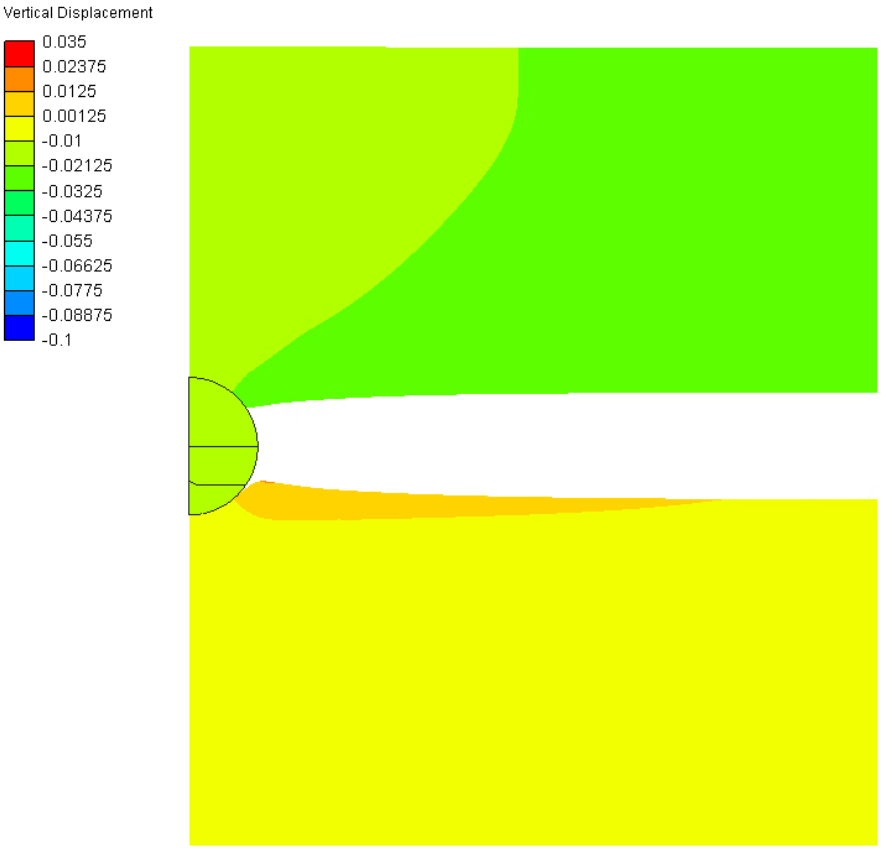

(a)

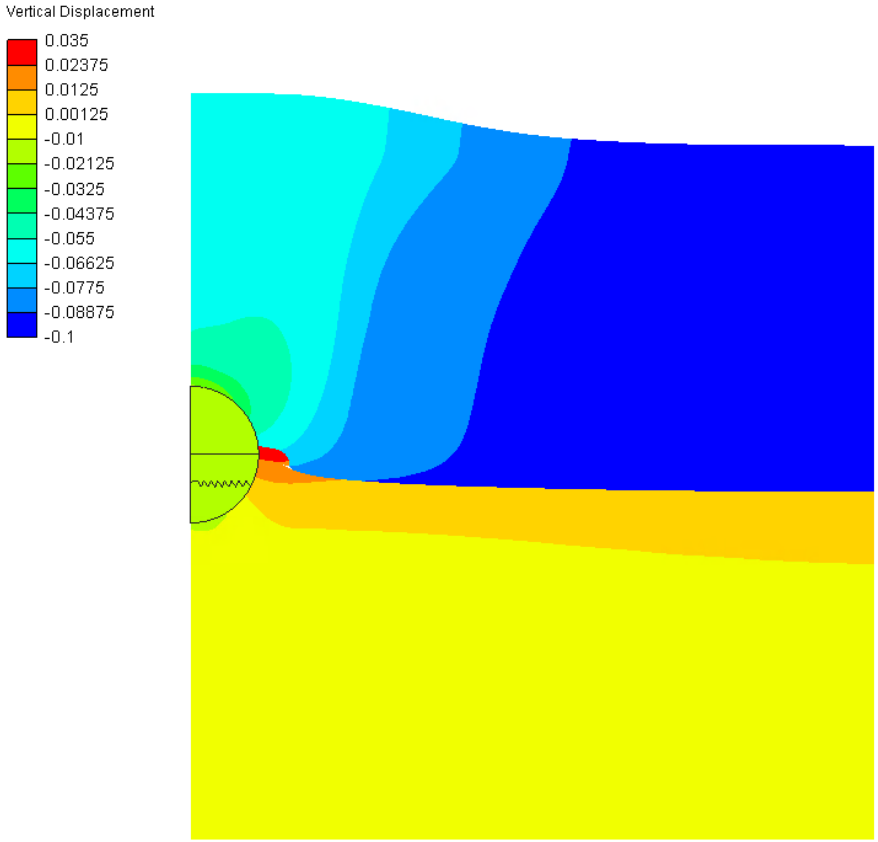

(b)

Figure 5.7: Contour plot of the vertical displacement in elastoplastic finite element mdoelling of proppant embedment for $\rho_p = 0.1$ under (a) $\sigma_d = 10^{-4}$ (b) $\sigma_d = 5 * 10^{-4}$ (c) $\sigma_d = 10^{-3}$ and (d) $\sigma_d = 10^{-2}$. (First part)

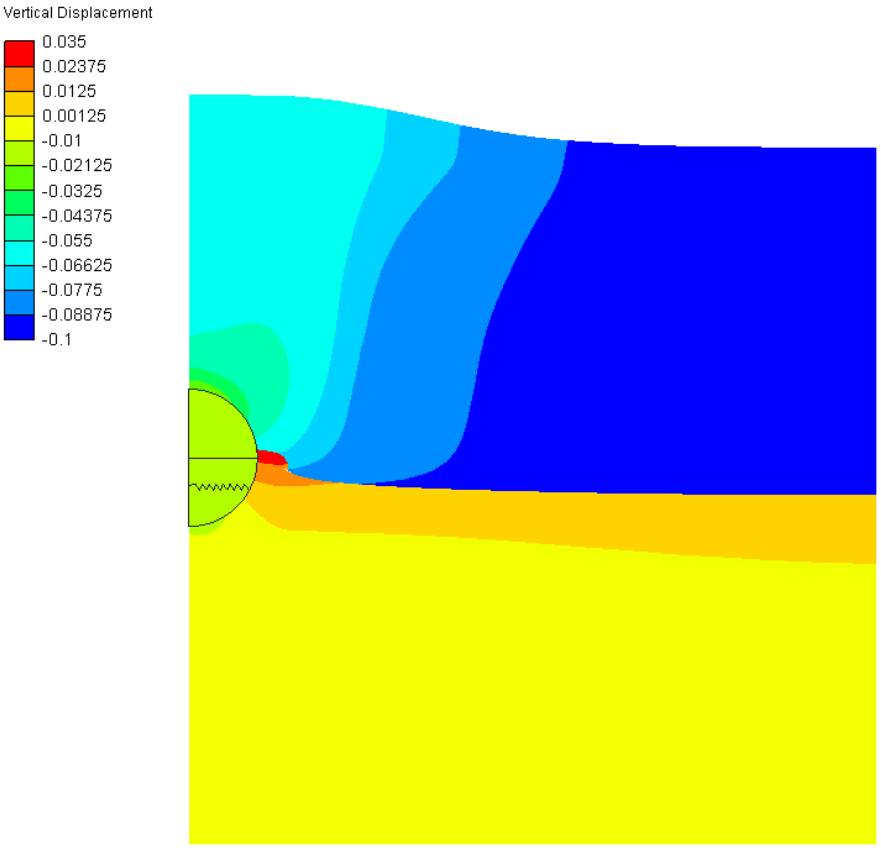

(c)

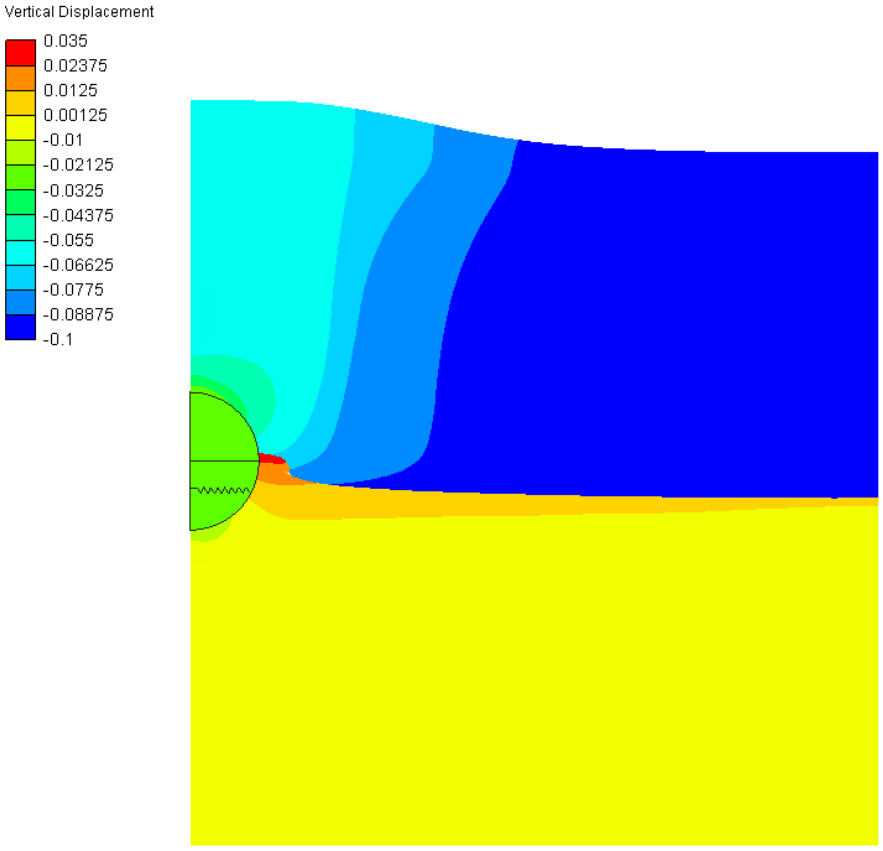

(d)

Figure 5.7: Contour plot of the vertical displacement in elastoplastic finite element mdoelling of proppant embedment for $\rho_p = 0.1$ under (a) $\sigma_d = 10^{-4}$ (b) $\sigma_d = 5 * 10^{-4}$ (c) $\sigma_d = 10^{-3}$ and (d) $\sigma_d = 10^{-2}$. (Cont.)

ρ_p	$\sigma_d = 10^{-4}$	Δx	$\sigma_d = 10^{-3}$	Δx	$\sigma_d = 10^{-2}$	Δx
0.1	N/A	0.003125	0	N/A	0	N/A
0.2	0.090044	0.002	N/A	0.002	0	N/A
0.3	0.095137	0.00208	0.059012	0.00208	0	N/A
0.4	0.097163	0.00156	0.076454	0.00156	0	N/A
0.5	0.097981	0.00125	0.084115	0.00125	0	N/A
0.6	0.098367	0.00104	0.090332	0.00104	0	N/A
0.7	0.098798	0.00111	0.093404	0.00111	0.030393	0.00111
0.8	0.098958	0.00098	0.094623	0.00098	0.048349	0.00098
0.9	0.099234	0.00116	0.094729	0.00116	0.066209	0.00116
1	0.099275	0.00104	0.096403	0.00104	0.065664	0.00104

Table 5.2: Average fracture aperture (*mm*) of the elastoplastic model under various values of dimensionless confining stress and the corresponding Δx (*mm*)for varying particle concentration.

Of the greatest interest in these figures is the one shown in Fig. 5.8(c), in which the proppant was completely embedded into coal. However, there still existed an open channel for fracking fluid to flow through. The fracture aperture increased with the distance away from the proppant, which was in contrast to the elastic model where the fracture aperture decreased with the distance away from the contact area. Fig. 5.17 graphs the principal stress of the proppant embedment modelling for $\rho_p = 0.2$ under $\sigma_d = 10^{-3}$. The stress concentrated around the contact area which caused dramatic deformation in coal. The stretch area was less influenced by the proppant embedment, thus maintaining a larger portion of the initial fracture aperture.

The average fracture aperture under varying dimensionless confining stress for each particle aspect ratio is listed in Table 5.2, where 0 denotes closure of the fracture and N/A indicates irregular fracture shape such as the one shown in Fig. 5.8(c). As expected, the average fracture aperture decreased with the remote confining stress and increased with the normalised particle concentration. In addition, comparing the listed data in Table 5.2 that in Table 5.1, the elastoplastic models suffered from larger deformation, which led to more dramatic reduction in fracture permeability under the same stress conditions.

5.3.2 Numerical Analysis of Fracture Permeability

After the finite element modelling of the proppant embedment was finished, the obtained geometry was then imported into the LBM solver based on the axisymmetric method, thus creating a 3D computational domain for fluid. A D3Q27 lattice was used. The height of the fluid domain was set as $2r_s = 0.1mm$ and the fluid viscosity was set as the unit value of 1 in order to improve computational efficiency. For most of the elastoplastic models that were simulated, the curvature of the deformed fracture surfaces could be neglected as if the proppant was directly embedded into coal by a certain depth, as illustrated in Fig. 5.1(a). However, for those cases where the fractures were subjected to irregular deformation such as the one shown in Fig. 5.8(c), additional treatment was required to generate a geometry file according to the coordinates of the points on fracture surfaces. The geometry files were then imported into the LBM solver to create the computational fluid domain. Fig. 5.18 presents a cross-section view of the velocity contour of the fluid flow through a propped fracture generated from one of those special cases shown in Fig. 5.8(c). The values of Δx in other simulation cases are presented in Table 5.2. Different Δx was selected according to the fracture aperture and deformation, which was consistent with the elastic model. For example, a grid spacing of $0.002mm$ was selected for the case of $\rho_p = 0.2$, which

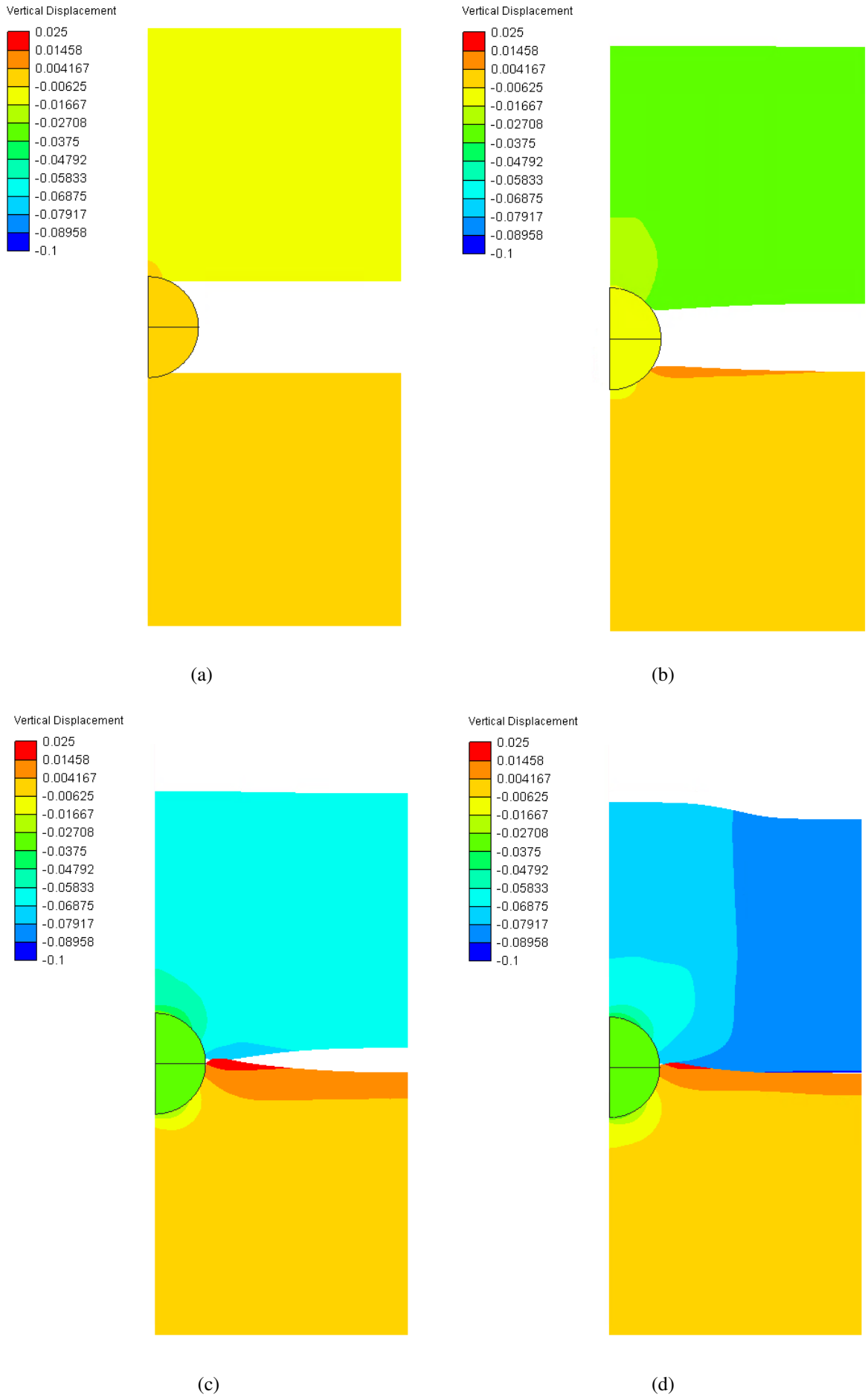

Figure 5.8: Contour plot of the vertical displacement in elastoplastic finite element mdoelling of proppant embedment for $\rho_p = 0.2$ under (a) $\sigma_d = 10^{-4}$ (b) $\sigma_d = 5 * 10^{-4}$ (c) $\sigma_d = 10^{-3}$ and (d) $\sigma_d = 10^{-2}$.

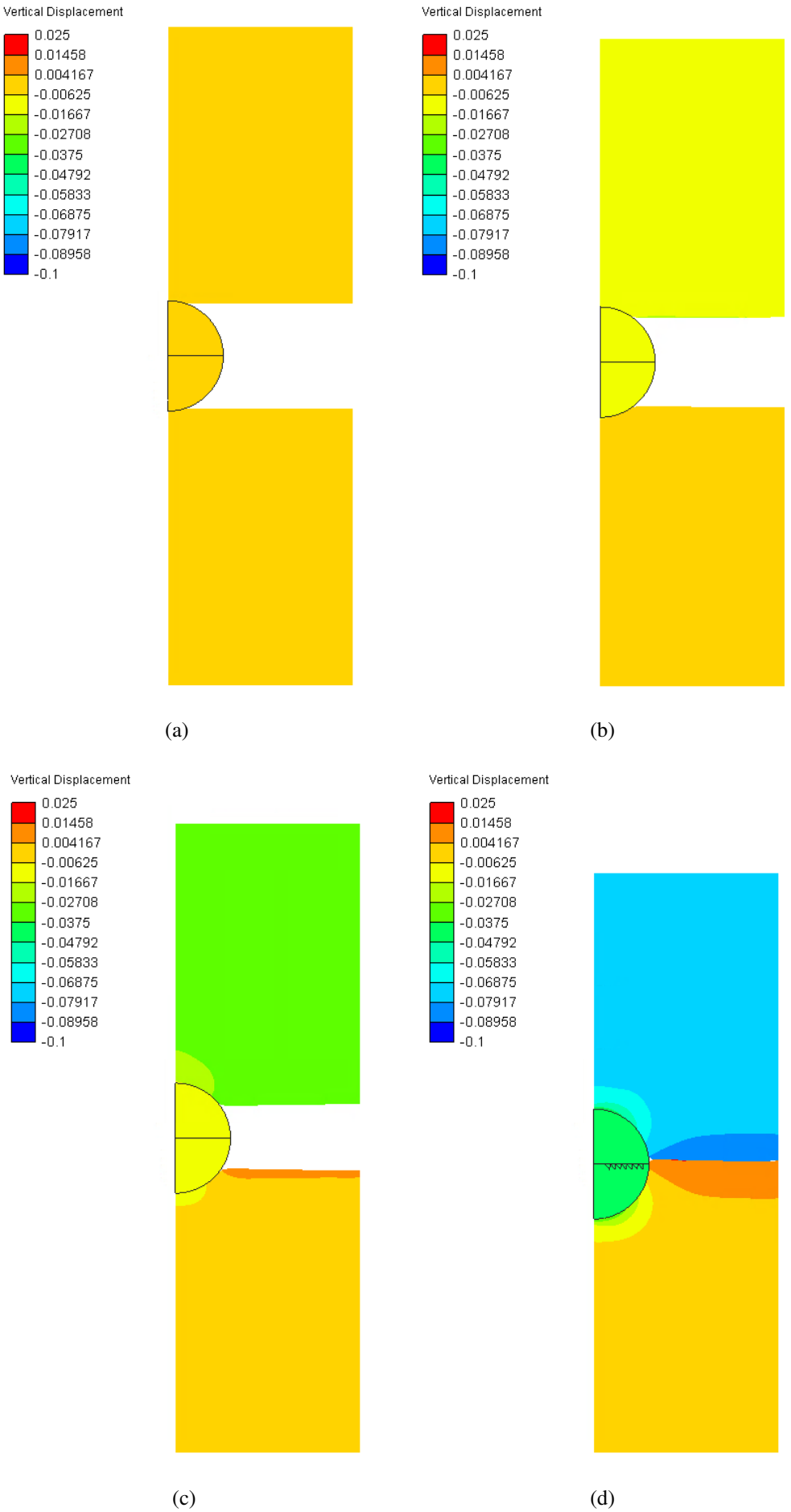

Figure 5.9: Contour plot of the vertical displacement in elastoplastic finite element mdoelling of proppant embedment for $\rho_p = 0.3$ under (a) $\sigma_d = 10^{-4}$ (b) $\sigma_d = 5 * 10^{-4}$ (c) $\sigma_d = 10^{-3}$ and (d) $\sigma_d = 10^{-2}$.

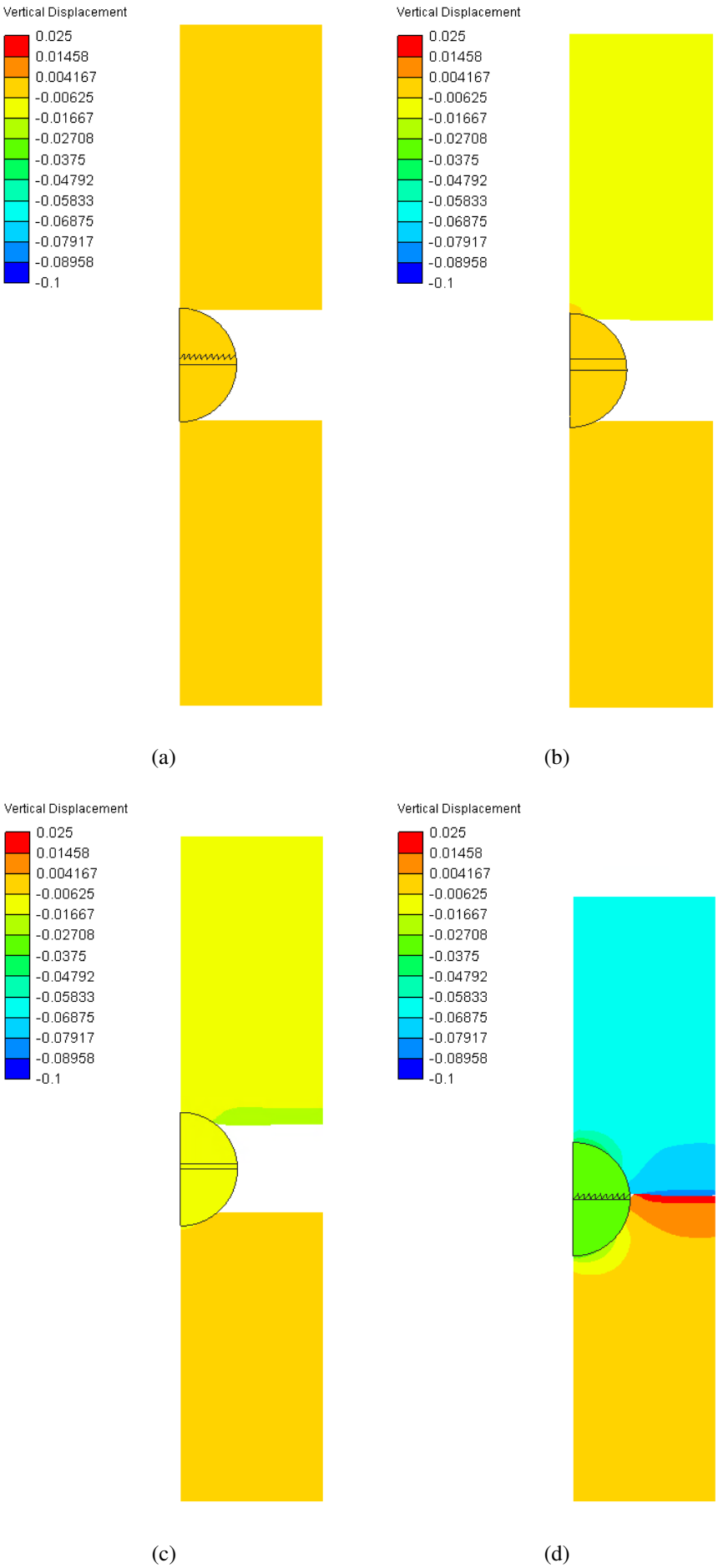

Figure 5.10: Contour plot of the vertical displacement in elastoplastic finite element mdoelling of proppant embedment for $\rho_p = 0.4$ under (a) $\sigma_d = 10^{-4}$ (b) $\sigma_d = 5 * 10^{-4}$ (c) $\sigma_d = 10^{-3}$ and (d) $\sigma_d = 10^{-2}$.

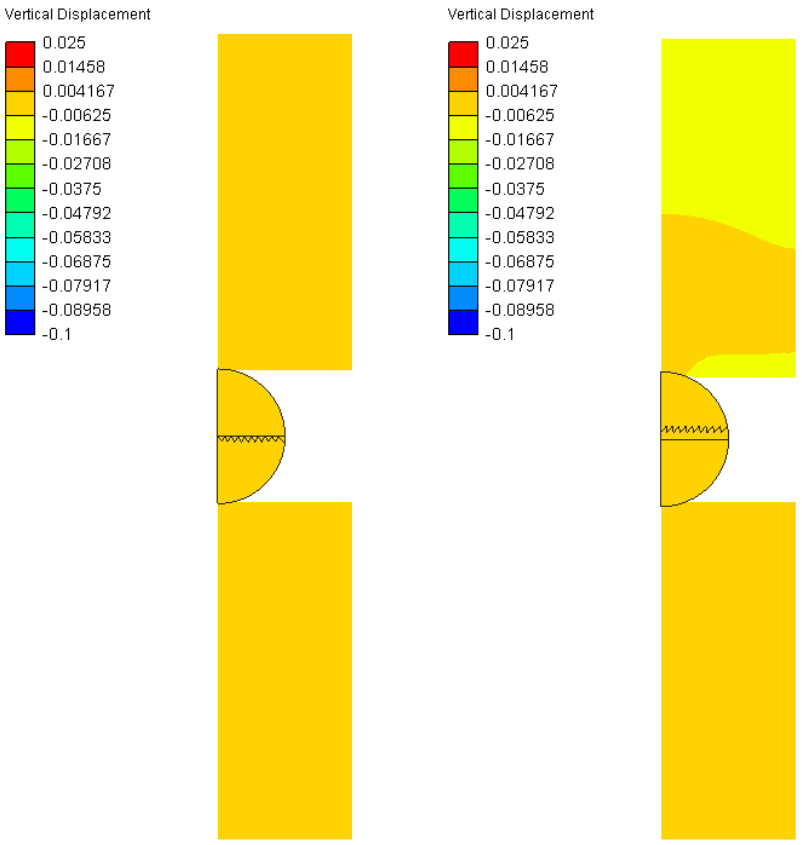

(a)

(b)

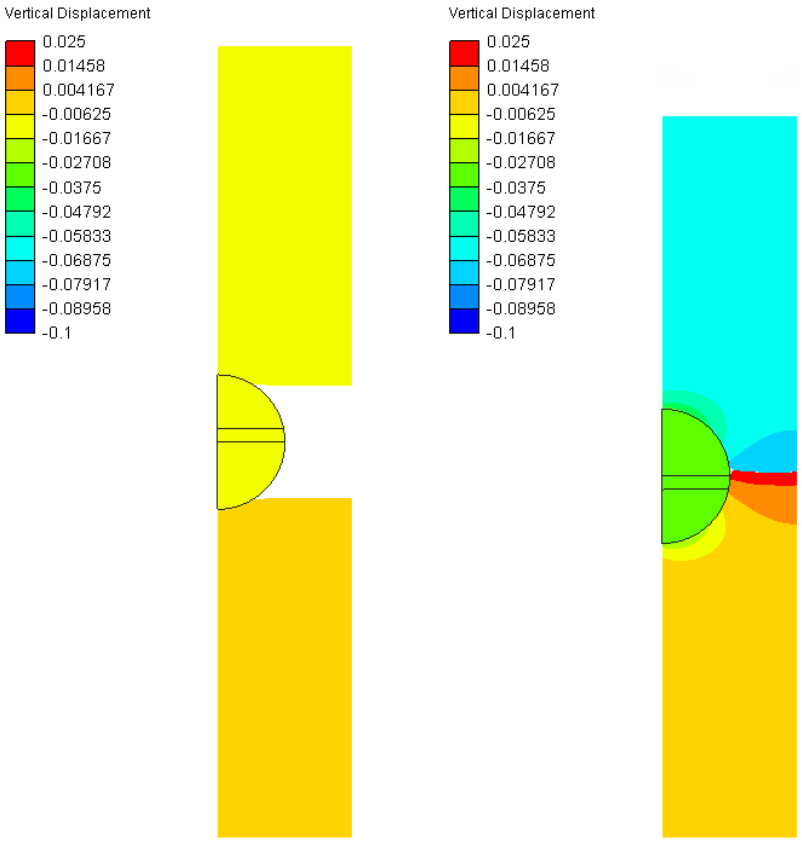

(c)

(d)

Figure 5.11: Contour plot of the vertical displacement in elastoplastic finite element mdoelling of proppant embedment for $\rho_p = 0.5$ under (a) $\sigma_d = 10^{-4}$ (b) $\sigma_d = 5 * 10^{-4}$ (c) $\sigma_d = 10^{-3}$ and (d) $\sigma_d = 10^{-2}$.

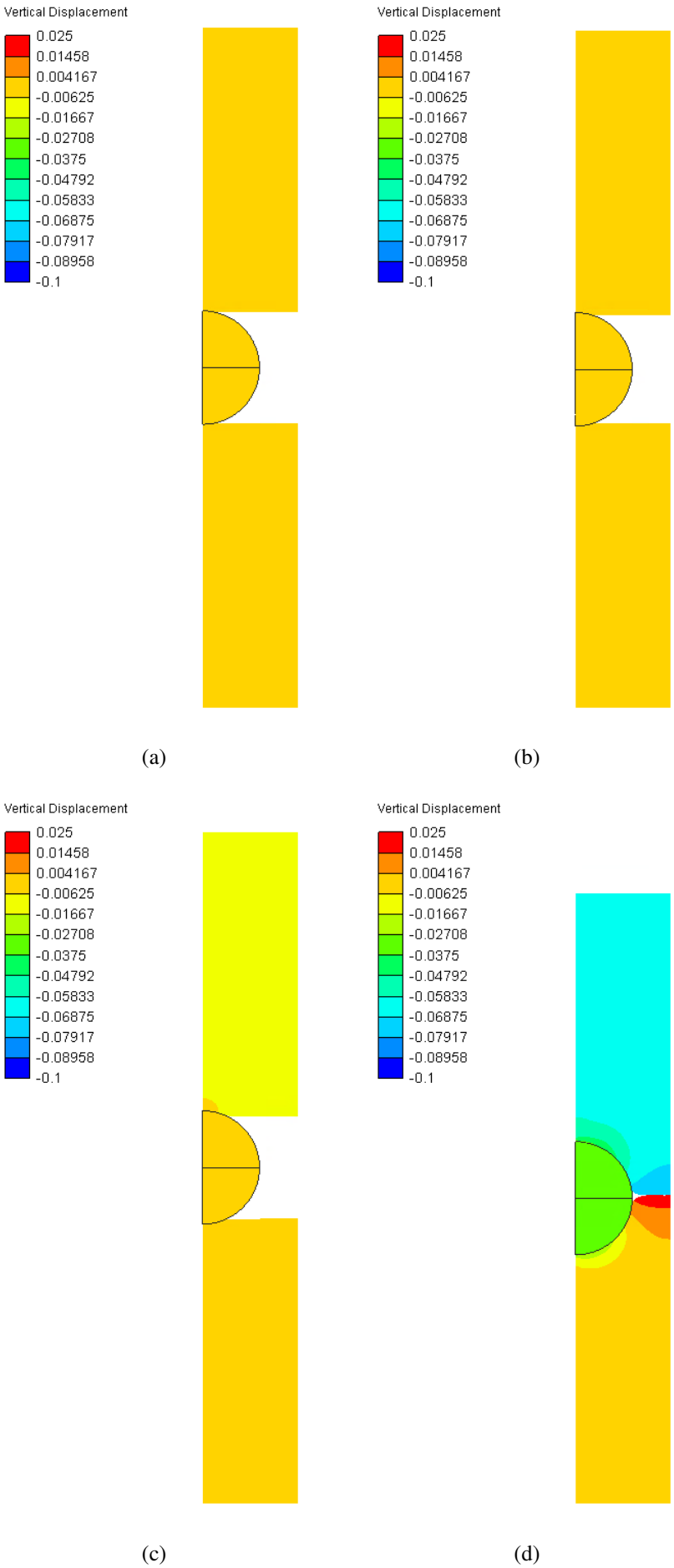

Figure 5.12: Contour plot of the vertical displacement in elastoplastic finite element mdoelling of proppant embedment for $\rho_p = 0.6$ under (a) $\sigma_d = 10^{-4}$ (b) $\sigma_d = 5 * 10^{-4}$ (c) $\sigma_d = 10^{-3}$ and (d) $\sigma_d = 10^{-2}$.

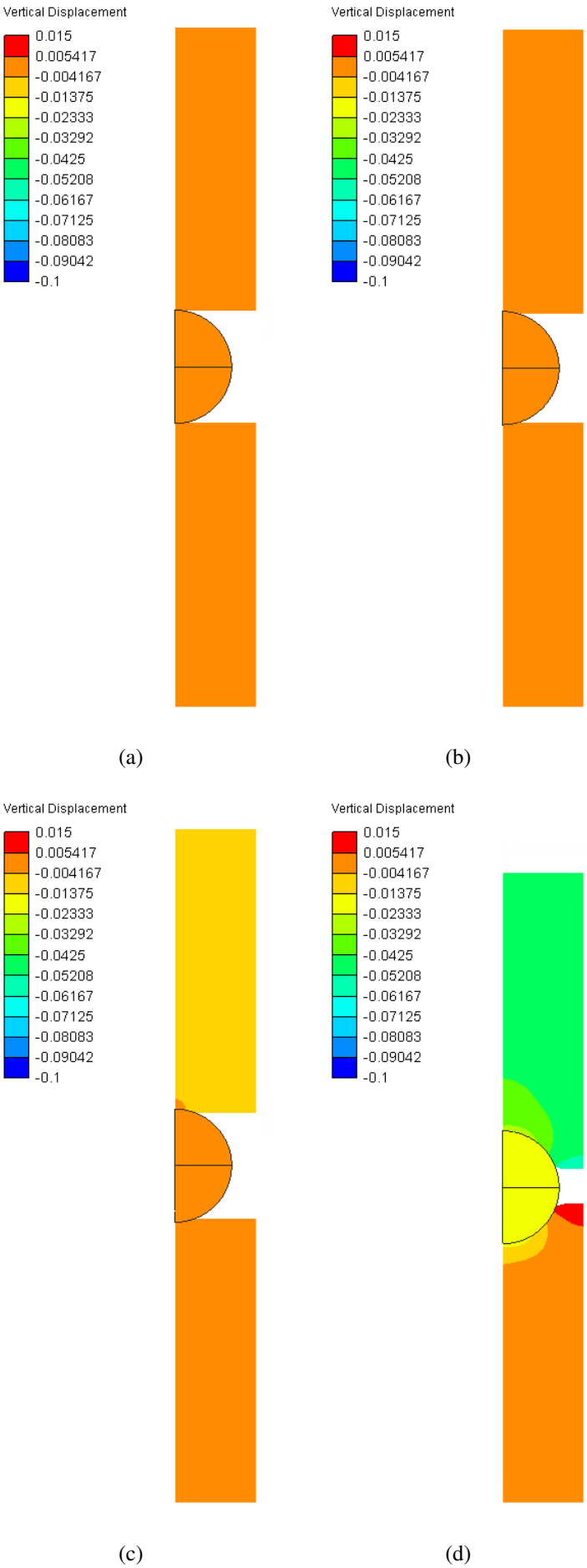

Figure 5.13: Contour plot of the vertical displacement in elastoplastic finite element mdoelling of proppant embedment for $\rho_p = 0.7$ under (a) $\sigma_d = 10^{-4}$ (b) $\sigma_d = 5 * 10^{-4}$ (c) $\sigma_d = 10^{-3}$ and (d) $\sigma_d = 10^{-2}$.

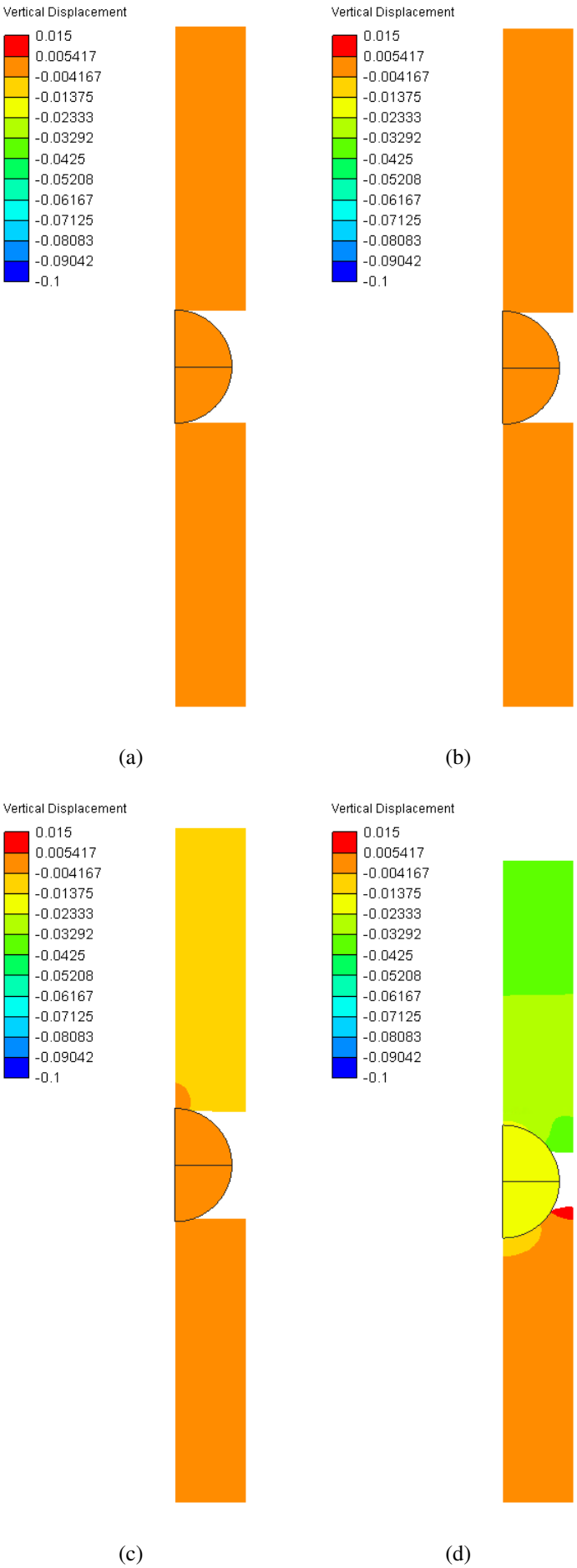

Figure 5.14: Contour plot of the vertical displacement in elastoplastic finite element mdoelling of proppant embedment for $\rho_p = 0.8$ under (a) $\sigma_d = 10^{-4}$ (b) $\sigma_d = 5 * 10^{-4}$ (c) $\sigma_d = 10^{-3}$ and (d) $\sigma_d = 10^{-2}$.

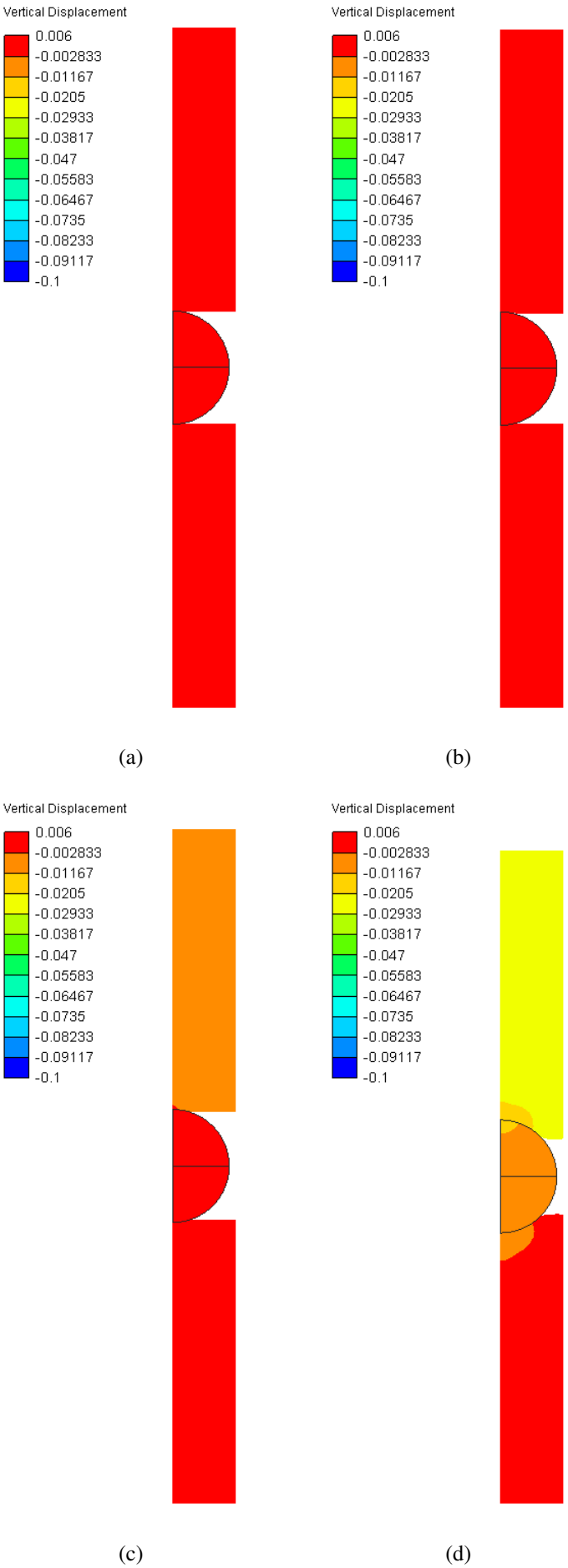

Figure 5.15: Contour plot of the vertical displacement in elastoplastic finite element mdoelling of proppant embedment for $\rho_p = 0.9$ under (a) $\sigma_d = 10^{-4}$ (b) $\sigma_d = 5 * 10^{-4}$ (c) $\sigma_d = 10^{-3}$ and (d) $\sigma_d = 10^{-2}$.

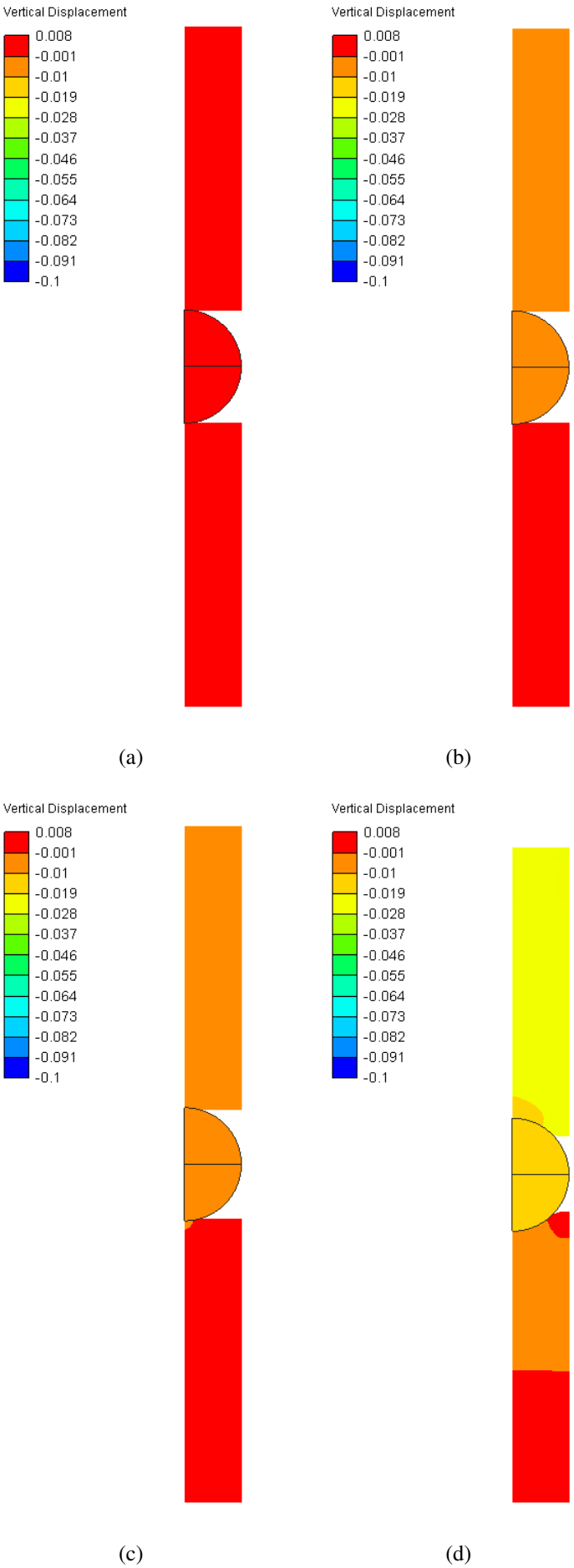

Figure 5.16: Contour plot of the vertical displacement in elastoplastic finite element mdoelling of proppant embedment for $\rho_p = 1.0$ under (a) $\sigma_d = 10^{-4}$ (b) $\sigma_d = 5 * 10^{-4}$ (c) $\sigma_d = 10^{-3}$ and (d) $\sigma_d = 10^{-2}$.

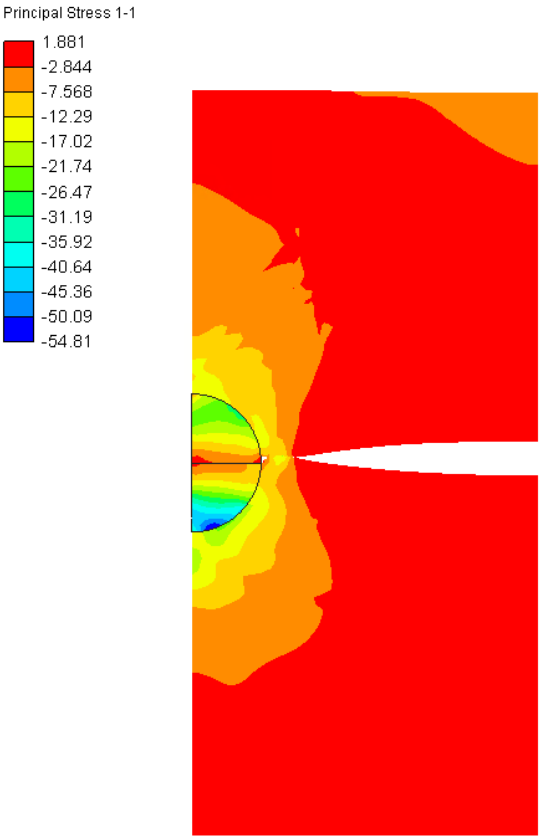

Figure 5.17: Contour plot of the maximum principal stress in elastoplastic finite element mdoelling of proppant embedment for $\rho_p = 0.2$ under $\sigma_d = 10^{-3}$.

resulted in a total of approximately $3.27e06$ nodes. The proppant embedment mechanism and fluid flow through the residual fracture aperture were well characterised by the use of such a relatively fine grid.

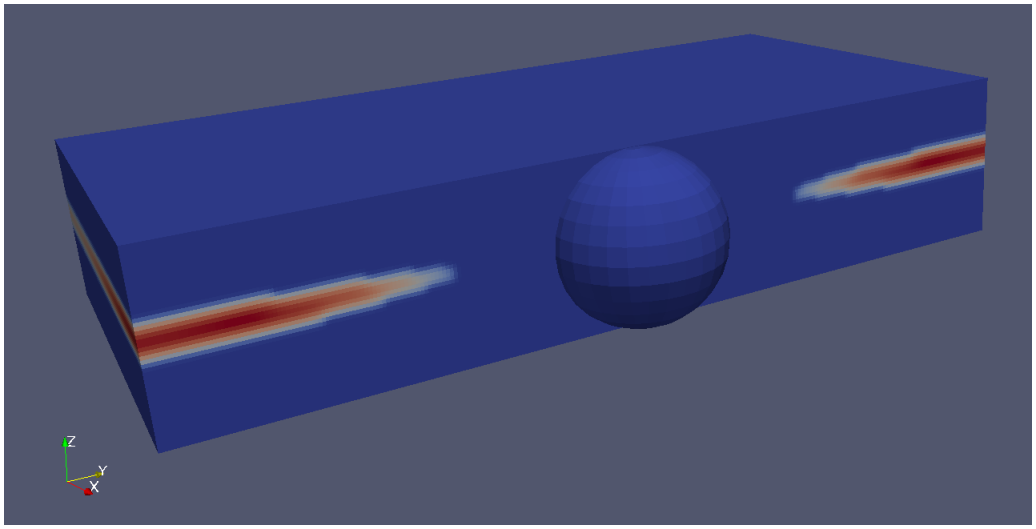

Figure 5.18: A cross-section view of the fluid velocity contour in a propped fracture of $\rho_p = 0.2$ and $\sigma_d = 10^{-3}$.

The results are plotted in the fracture permeability diagram, as shown in Fig. 5.19. The results are qualitatively consistent with the results of elastic modelling. The resultant optimal particle concentration increased with the increase of confining stress, and the permeability was more sensitive to the particle concentration

around the optimal concentration value than other values. Comparing the elastoplastic model with the elastic model, as shown in Fig. 5.20, more severe reduction in permeability was caused under the same dimensionless confining stress. The fracture permeability diagram also indicates that the major elastoplastic deformation of the fracture occurred when the dimensionless confining stress $10^{-4} < \sigma_d < 10^{-3}$, as there is a considerable gap between these two curves. To improve the understanding of the influence of proppant embedment on fracture permeability, more models under other dimensionless confining stress values were simulated to highlight the relationship between the optimal particle concentration and remote confining stress. For the given coal properties in this study, 10^{-2} was a critical dimensionless confining stress as more than 98% of the initial permeability was lost due to elastoplastic deformation and proppant embedment, which indicates fracture closure.

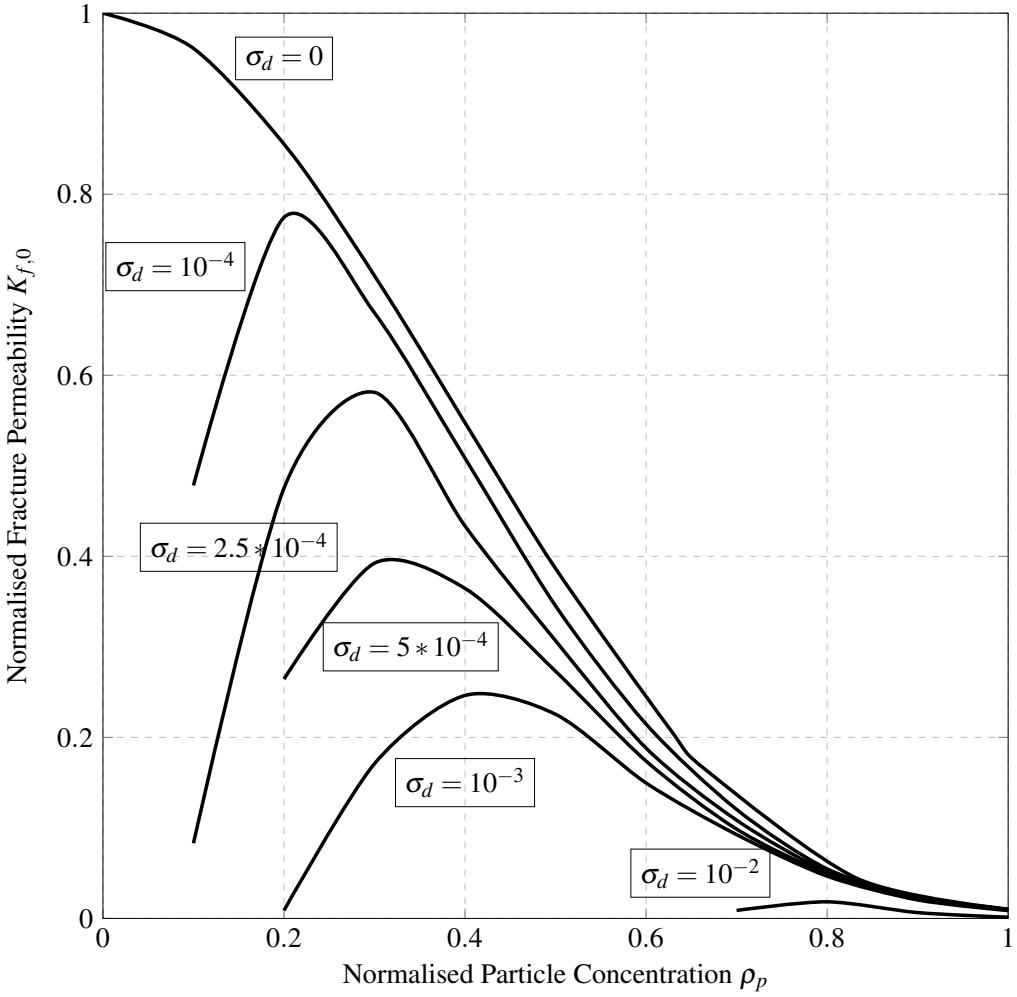

Figure 5.19: Fracture permeability diagram: the normalised fracture permeability against proppant concentration under varying dimensionless confining stress.

Under certain effective stress, a large value of ρ_p corresponds to a large distance between packed particles (or small particle concentration), which yields small fracture aperture due to surface deformation and, therefore, low value of fracture permeability. Conversely, a very small value of ρ_p indicates dense packing of particles in the fracture, and high resistance to the fluid flow, thus a small value of permeability. As a result, the permeability diagram is non-monotonic and there exists an optimal value of ρ_p yielding the maximum permeability for each effective stress condition.

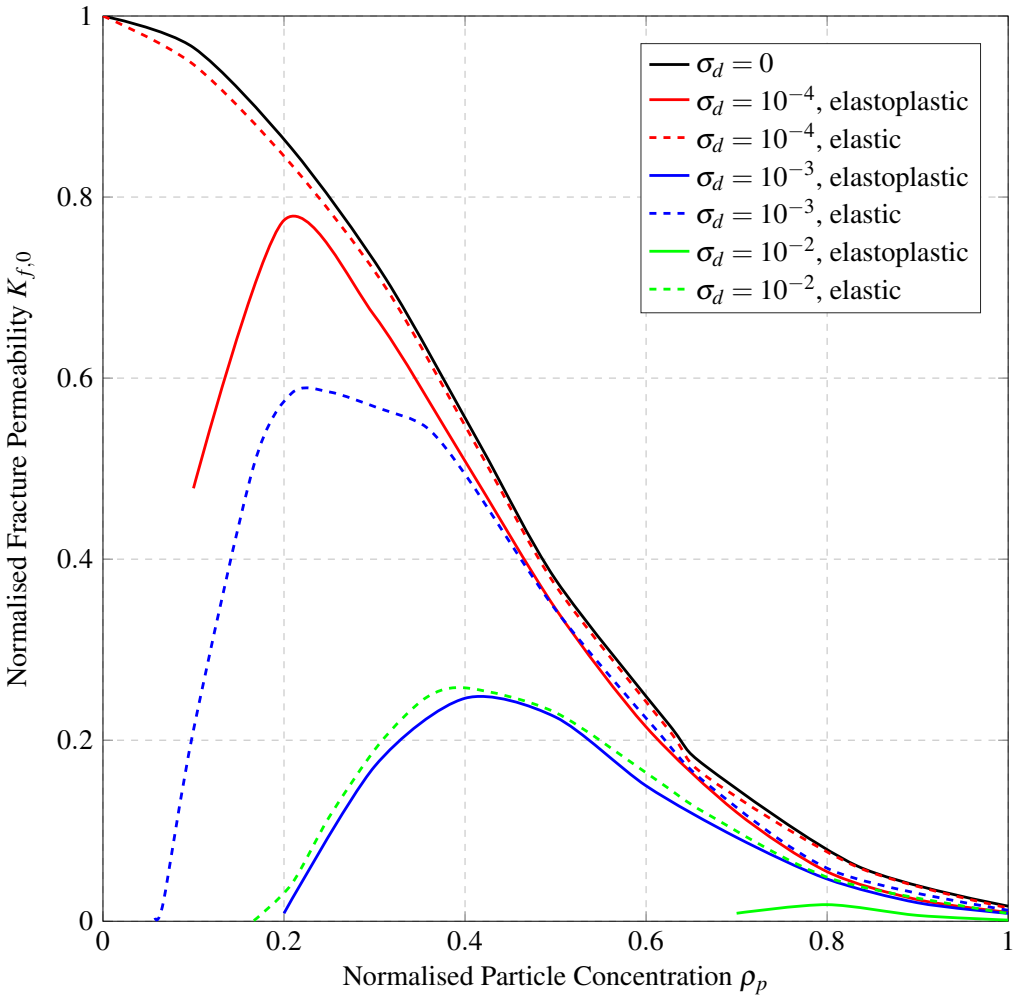

Figure 5.20: Comparison of the elastic and elastoplastic fracture permeability diagrams: the normalised fracture permeability against proppant concentration under varying dimensionless confining stress.

5.4 Case Study for Well Productivity Enhancement by Proppant Injection

The obtained fracture permeability diagrams were then applied to the prediction of well productivity enhancement by proppant injection. The coal seam gas reservoir in *Bowen Basin, Central Queensland, Australia* was selected for the present case study to investigate the influence of proppant injection and embedment on productivity. A mathematical model proposed by Keshavarz et al. [159] was applied to this study for quantitative investigation.

An axisymmetric flow in well-reservoir system is considered in this analytical model. Fracture permeability reduction due to particle straining is incorporated into the model. The main assumptions of the model include, (1) particles and carrying water are incompressible, (2) fracture permeability depends on effective stress as an exponential function, (3) velocities of particles and carrying water are equal, and (4) particle straining occurs if the fracture aperture is equal to the particle size. During the injection of fracking fluids into a fracture reservoir, the pressure-dependent permeability is calculated as,

$$K(p) = K_0 \exp\left[3C_f \alpha (p - p_{res})\right], \tag{5.18}$$

where the reference permeability K_0 corresponds to the reservoir pressure p_{res}. C_f and α are the fracture

compressibility and Biot's constant, respectively.

Based on Darcy's law, the relationship between the axisymmetric flow rate in the fracture and the pressure dependent permeability is then expressed as,

$$q = -\frac{2\pi r K(p)}{\mu}\frac{dp}{dr}. \tag{5.19}$$

Substituting Eq. (5.18) into Eq. (5.19), rearranging the variables and integrating the reservoir pressure at the drainage radius, the pressure profile of the fractured area during production can be obtained, which is written as,

$$p(r,q) = p_{res} + \frac{1}{3\alpha C_f}\ln\left[1 - \frac{3\alpha C_f \mu q}{2\pi K_0}\ln\frac{r}{r_e}\right]. \tag{5.20}$$

Consequently, combining Eq. (5.18) and Eq. (5.20) yields the permeability distribution within the fractured area during production, which is,

$$K(r,q) = K_0\left[1 - \frac{3\alpha C_f \mu q}{2\pi K_0}\ln\frac{r}{r_e}\right]. \tag{5.21}$$

Furthermore, the well productivity index is derived by substituting Eq. (5.21) into Eq. (5.19) and integrating pressure gradient from r_w to r_e. The productivity index before proppant injection is written as,

$$PI_0 = \frac{q_p}{p_{res} - p_w} = \frac{-3\alpha C_f q}{\ln\left[1 - \frac{3\alpha C_f \mu q}{2\pi K_0}\ln\frac{r_w}{r_e}\right]}, \tag{5.22}$$

and the productivity index after proppant injection is computed as,

$$PI = \frac{q_p}{(p_{res} - p_{st}) + (p_{st} - p_w)}. \tag{5.23}$$

In this study, the reference permeability was set as $K_0 = 5.8mD$ and the corresponding reservoir pressure was $p_{res} = 1000psi$. An area with a drainage radius of $r_e = 100m$ was selected for analysis.

Using Eq. (5.20), the resultant pressure distribution profiles during production process are plotted in Fig. 5.21, in which the black curve refers to the pressure distribution without hydraulic fracturing. The blue, red and green curves represent the pressure distribution for stimulated areas with the radii of $0.01r_e$, $0.03r_e$ and $0.05r_e$. The pressure profiles of the stimulated areas are above that without stimulation. Therefore, the proppant injection allowed for the same rate but at lower pressure drawdown, which contributes to the well productivity enhancement. Additionally, the elastoplastic model led to larger pressure drawdown than the elastic model, which was consistent with the results presented in the fracture permeability diagrams.

The permeability distribution profiles within the the stimulated area with a radius of $0.05r_e$ under varying injection pressure is shown in Fig. 5.22. The fracturing pressure was set as $p_{fr} = 2400psi$. The black curve characterises the initial permeability profile before stimulation and the blue, red and green curves correspond to the permeability distribution profiles under $0.7p_{fr}$, $0.8p_{fr}$ and $0.9p_{fr}$. The curves clearly indicate the influence of proppant injection on fracture permeability, with a maximum of approximately thirteen-times permeability enhancement achieved by the elastic model and a five-times enhancement by the elastoplastic model near the wellbore. Consequently, the higher the injection pressure, the greater the permeability enhancement. The permeability decreased with the distance away from the wellbore, and the decreasing rate reduced as the distance increased. Comparing the elastoplastic and elastic models, the latter led to greater permeability enhancement.

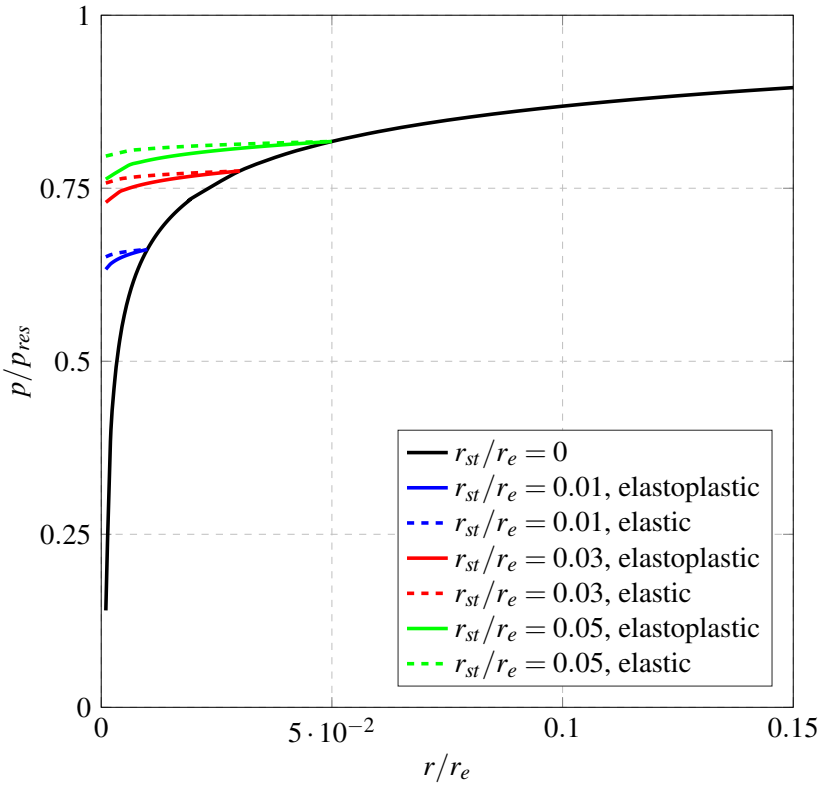

Figure 5.21: Pressure distribution profiles for varying stimulated radius during production.

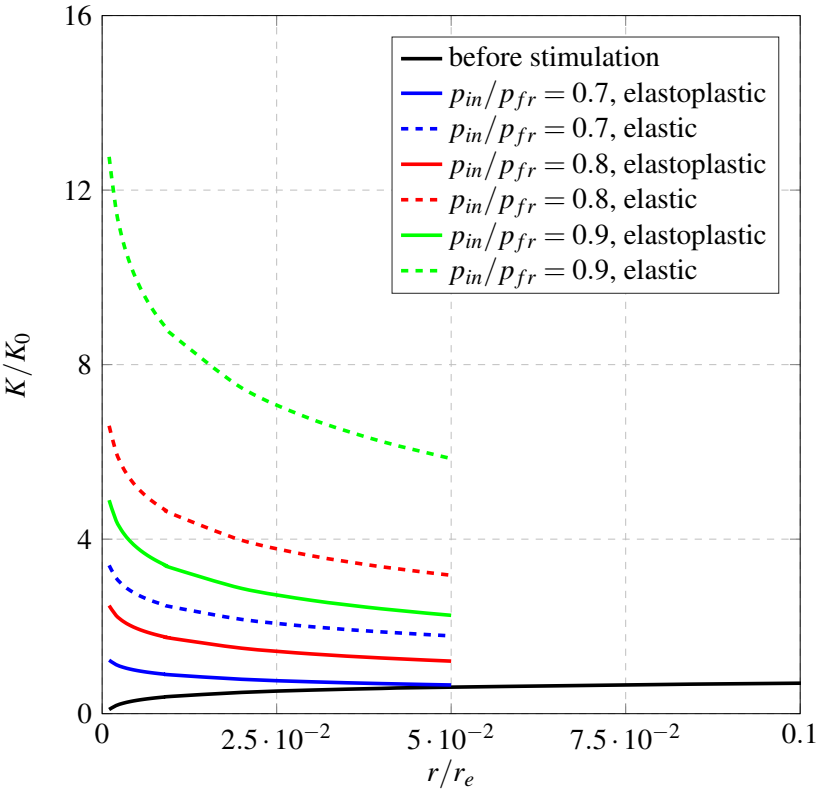

Figure 5.22: Permeability distribution profile for a stimulated radius of $r_{st} = 0.05 r_e$ under varying injection pressure.

The results for normalised well productivity index under varying injection pressure are plotted in Fig. 5.23 against stimulated radius. It can be observed that the productivity index increased with the stimulated area and with the injection pressure. Meanwhile, the elastoplastic model yielded smaller productivity index when comparing to the elastic model, which was a result of weaker permeability enhancement under the same stress conditions. Nevertheless, both models were able to ensure at least a two-time of the initial productivity index due to proppant injection.

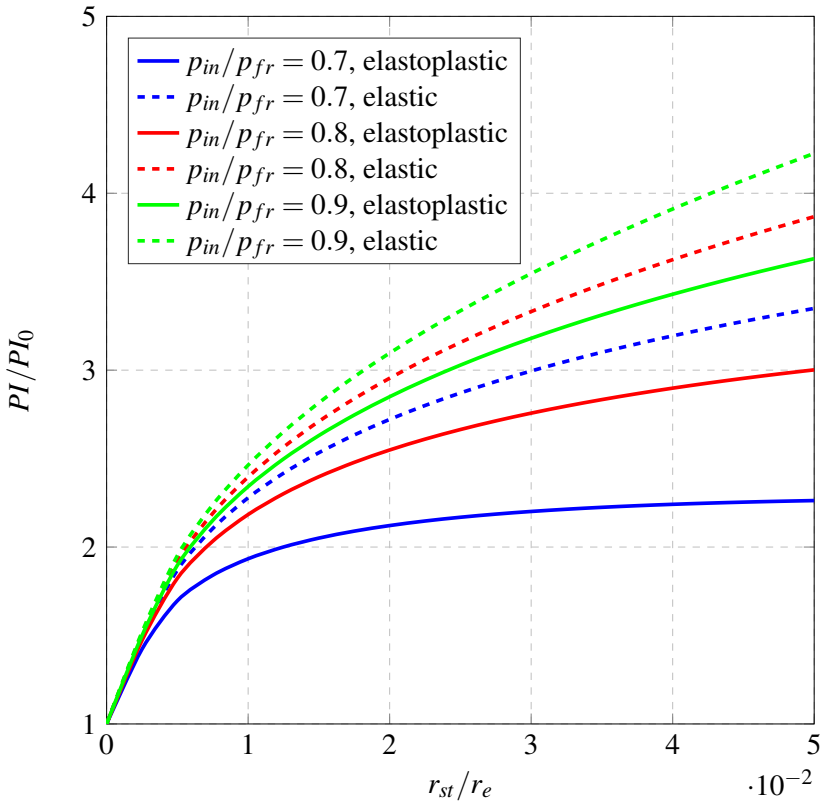

Figure 5.23: Normalised well productivity index against stimulated radius under varying injection pressure.

Finally, the influence of fracture compressibility on productivity index enhancement is presented in Fig. 5.24. Generally speaking, the higher the cleat compressibility, the larger the proppant that can be injected, and consequently the higher the productivity index after stimulation. At the same cleat compressibility, the elastoplastic model yielded smaller productivity index increase than the elastic model.

5.5 Summary

In the study presented in this chapter, elastoplastic finite element modelling of proppant embedment and lattice Boltzmann modelling of fracture permeability have been used to investigate the effect of proppant embedment on well production enhancement after proppant injection. Results of fracture permeability reduction factor due to particle embedment were then applied to the mathematical model for well productivity prediction. The LBM simulations for a range of particle embedment patterns revealed the nonlinear relationship between fracture permeability and particle aspect ratio, under different stress conditions. Proppant injection resulted in an increase in fracture permeability above the initial value, expanded the stimulated zone, and consequently

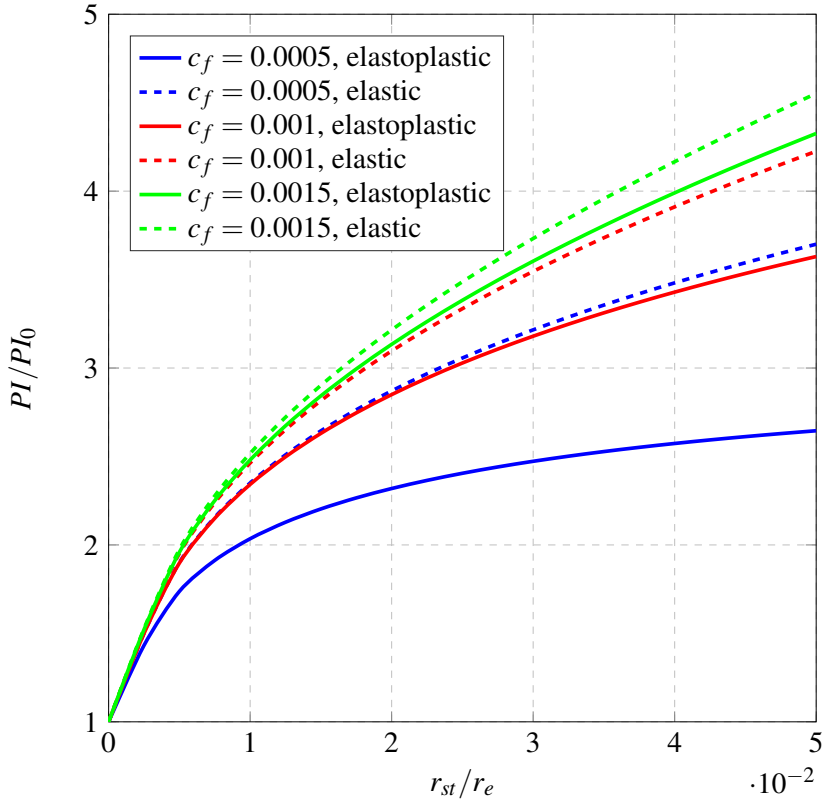

Figure 5.24: Normalised well productivity index against stimulated radius for varying fracture compressibility.

increased the productivity index. The impact of hydraulic fracturing on well productivity enhancement was substantial, highlighting the importance of a proper proppant injection. Modelling results also indicated that elastoplastic fracture deformation resulted in lower permeability and production enhancement, as compared to the linear elastic deformation applied in previous models. Neglecting formation failure tended to overestimate the production enhancement with proppant embedment. This represents an improvement to the analytical solution from the Hertz elastic contact theory previously used to characterise the deformation of fracture surfaces.

As a final remark, the developed workflow is applicable to the assessment of potential stimulation outcomes for a range of uncertain reservoir parameters. Better understanding and implementation of proppant injection and placement can improve post-fracturing results in low-permeability coal intervals substantially.

Chapter 6

Conclusions

This thesis has presented the implementation and application of an improved computational framework which couples the lattice Boltzmann method (LBM) and discrete element method (DEM) using the two-relaxation-time (TRT) collision operator along with the modified partially saturated method (PSM). The implementation of the TRT-PSM formulation successfully addressed several computational issues related to the LBM including viscosity-dependence and synchronisation with the DEM. The modified LBM-DEM framework was then applied in the investigation of numerical rheometry of dense particle suspensions, in which the behaviour of the suspensions was studied in detail. Separating the hydrodynamic and mechanical contributions to the suspension friction coefficient provided fundamental new insights on the suspension rheology. In Chapter 5, the TRT-PSM formulation was applied in fracture permeability modelling, in which a commercial finite element package, *Elfen*, was used as an assisting numerical tool to predict the elastoplastic fracture deformation under the influence of proppant embedment. Consequently, fracture permeability charts were generated for further evaluation of well productivity index in the case study.

6.1 Discussion of Results

Chapter 3 presented an improved framework for LBM-DEM modelling that uses the TRT collision operator and the PSM [56] boundary condition with a new solid weighting function. While previous studies [53, 56, 62, 115] have relied on the BGK collision operator, the TRT operator was used here as a means to address the issue of viscosity-dependence in drag and permeability calculations. This was further improved by the definition of a new, empirical function for weighting the PSM collision operator.

Results have shown that the TRT-PSM formulation exhibits significantly improved accuracy over the BGK-PSM formulation. The modified solid weighting function was also demonstrated to provide a range of computational viscosities, and therefore relaxation parameters, in which drag and permeability predictions are constant. Flow past a periodic array of spheres, both simple-cubic (SC) and body-centred-cubic (BCC) packs, were found to be suitable benchmark scenarios to test the different combinations of the PSM collision operator and weighting function combinations. At low computational viscosities, errors were kept below 2% at modest lattice resolutions. Further studies aimed at validating the hydrodynamic force calculation and the flow profile revealed that the TRT formulation yields improved accuracy over the BGK formulation while maintaining the

second-order convergence with the relative grid spacing.

Despite the improvements to the PSM boundary condition presented here, drag and permeability errors still increase rapidly at higher computational viscosities (i.e. $\nu > 0.2$). This may constrain some applications, however the range of viscosity-independence presented here will suffice for the majority of LBM-DEM simulations involving non-Brownian suspensions. The optimal value for the summation index, b, was found to be four for the simulations presented in this study. Limited improvement was made with the further increase of b. However, since the modified weighting function was proposed on an empirical basis, the choice of b may vary with the exact problem that is simulated. Consequently, this should be considered in any future applications. Furthermore, the simulations presented in this study are based on spherical obstacles. Non-spherical obstacles have not been tested with the improved LBM-DEM framework. This is an objective of future research, along with the extension to non-Newtonian fluids.

In Chapter 4, the implemented LBM-DEM framework was applied to numerical modelling of shear flow of particle suspensions across a range of solid volume fractions. These models were representative of a Couette rheometer, from which the platen velocity, shear stress and normal stress were measured at steady state. These were used in turn to compute effective friction coefficients and viscosity ratios which have been compared to empirically derived constitutive expressions.

Numerical results with a low contact friction coefficient were consistent with predictions made using the expression for friction coefficient proposed by Morris and Boulay [127]. Following this validation of the LBM-DEM computational model, the results were used to analyse the form of hydrodynamic and mechanical contributions to friction coefficient in the constitutive expressions. The prediction of hydrodynamic contributions from the constitutive equations of Morris and Boulay, and Boyer et al. [128], were in good agreement with the presented model results. For a solid volume fraction less than 0.5, reasonable agreement was found with the expression of Morris and Boulay for mechanical contribution. However, the constitutive equations of Boyer et al., and Lecampion and Garagash [124], differed significantly from the computational model.

The difference in results from the LBM-DEM model, and the predictions of Boyer et al., and Lecampion and Garagash, are expected to be the product of geometric differences between the computational model and the rheometer used in experimentation. The rough rheometer surface in the experiments of Boyer et al. was emulated by increasing the contact friction coefficient. On doing so, the computational model produced results in agreement with their constitutive expression. This improved agreement is found not just in the overall suspension viscosity, but also in the hydrodynamic and mechanical contributions to suspension friction coefficient.

Results of shear-dependent flow have indicated that the LBM-DEM model exhibited Newtonian behaviour for dilute suspensions for a solid volume fraction of 0.2. While for a dense suspension with a solid volume fraction of 0.55, shear-thickening was firstly observed from the suspension under low strain rate. With the increase of strain rate, the computational model exhibited a strong shear-thinning behaviour, which was consistent with many previous studies. Additionally, successful separation and evaluation of the hydrodynamic and mechanical contributions to suspension friction coefficient provided a new approach to analysing shear-dependent behaviour of the suspensions.

This validation work shows that the coupled LBM-DEM framework is able to accurately reproduce the physics of particle suspensions, with the significant advantage of separating hydrodynamic and mechanical phenomena. Such a model will be a powerful tool in designing novel suspension formulations to be used in industry.

Finally, Chapter 5 included the results of fracture permeability modelling along with further analysis of well

productivity, in which the significance of proppant injection was demonstrated. In this study, the work of Khanna et al. [174], in which the Hertz contact theory was used to characterise the interaction between the fracture surface and proppant, was firstly duplicated. The LBM results agreed well with the CFD results published by Khanna et al. For every given value of the dimensionless confining stress, there existed an optimal particle concentration which led to the maximum fracture permeability. The fracture permeability decreased with the confining stress while the optimal particle concentration increased with the confining stress.

However, the elastic model had strict limitations. Several critical factors were not taken into account in the model including the cracking and failure of coal, proppant embedment, and crushing. Nevertheless, it was an ideal benchmark problem which provided fundamental understanding of the influence of confining stress and particle concentration on fracture permeability. Meanwhile, the achieved agreement indicated that the implemented TRT-PSM formulation was able to mimic the fluid flow through deformed fractures as well as to evaluate pore-scale permeability.

The TRT-PSM scheme was then applied in the fracture permeability modelling using an elastoplastic model. The finite element modelling provided a general methodology for predicting the elastoplastic deformation of the fracture, thus generating the computational domain for the LBM modelling of fluids. The resultant fracture permeability diagram was quantitatively consistent with the elastic model, in which the optimal particle concentration increased with the dimensionless confining stress. However, significant quantitative difference was exhibited by the elastoplastic model from the elastic model. The resultant fracture permeability was notably smaller and the corresponding optimal particle concentration was higher than those of the elastic model under the same stress condition. In addition, a larger gap between the permeability curves indicated the failure of the coal in the plastic zone.

The fracture permeability results were then used for further evaluation of the well productivity index in a case study for the *Bowen Basin, Central Queensland, Australia*. By the use of the analytical solutions proposed by Keshavarz et al. [159], Fig. 5.21 to Fig. 5.24 clearly highlighted the influence of proppant injection and embedment on well productivity enhancement. To summarise, the following conclusions can be drawn.

- The proppant injection and embedment effectively protected the fracture from closure, thus contributing to the permeability enhancement of the stimulated area. The permeability enhancement decreased with the distance away from the wellbore.

- Compared to elastic deformation of the coal fracture surface, elastoplastic deformation was less significant outside the contact zone with the particle and the coal surface. However, the particle embedded more deeply into the coal. This resulted in reduced fracture width and a decrease in fracture permeability under certain closure stress conditions.

- Fracture permeability approached to zero at a very dense or a loose particle packing in coal fractures (i.e. very large or small particle aspect ratios). An optimal value of particle aspect ratio yielded the maximum permeability for each stress condition.

- The pressure profiles of the stimulation area were greater than that without stimulation, which allowed for the same rate at lower pressure drawdown. The larger the stimulated radius, the better the performance of the stimulation. Meanwhile, the proppant injection maintained a relatively stable pressure distribution within the stimulated area.

- The well productivity enhancement was sensitive to both the injection pressure and the physical property of the fracture. According to the case study presented in Section 5.4, proppant injection led to an approximately $2.3-4.5$ times productivity index enhancement of the fractured well. Such enhancement increased with the increase of the injection pressure and stimulated area and with the decrease of the fracture compressibility.

The results have been presented and discussed in three chapters. First, the proposed modified solid weighting function in the PSM allowed for an improve coupling of the LBM-DEM approach. Second, it was shown that the LBM-DEM computational model was able to capture the numerical rheometry of dense particle suspensions. The separation of hydrodynamic and mechanical contributions to suspension friction coefficient provided fundamental new insights into the shear-dependent rheology of the suspensions. Finally, the fracture permeability modelling and well productivity analysis have successfully demonstrated the potential of the implemented LBM-DEM framework for applications in the industry context.

6.2 Future Research Outlook

This thesis has demonstrated the capability of the improved LBM-DEM coupling approach to model dense particle suspensions and fluid flow through hydraulic fractures. However, during the validation and application of the numerical framework, some issues have been identified, many of which arise from the assumptions of the computational model. Therefore, opportunities for future research and development are outlined as follows.

6.2.1 Non-Newtonian Fluid Modelling

The characterisation of non-Newtonian fluids is of great interest in the oil and gas industry as granular suspensions exhibit non-Newtonian behaviour. Within the scope of LBM modelling, numerous studies [47, 52, 66, 68, 74, 76, 176] can be found in the literature regarding non-Newtonian fluid modelling, which is usually utilised by varying the relaxation parameter, τ, according to the characteristic rate of strain, $\dot{e}$. However, as shown in Eq. (2.9), the relationship between the involved parameters can make parameter selection difficult for non-Newtonian fluid modelling when using the BGK collision operator. The modified solid weighting function, which was originally designed for minimising the error fluctuation caused by parameter selection, offers a potential methodology for tuning related parameters for certain applications.

6.2.2 Upscaling of the LBM-DEM approach for Particle Suspension Modelling

Reducing computational cost without sacrificing accuracy has always been a challenge in the context of numerical modelling. Particularly for hydraulic fracturing where millions to billions of particles are involved, it is difficult to perform a detailed industry-scale analysis of the entire reservoir. Therefore, it is of great significance to develop an accurate upscaling law in the DEM for large-scale simulations. An appropriate upscaling law should enable the use of larger discrete elements to replace a group of small elements, while ensuring such replacement does not change the physical behaviour of the solid elements. On the other hand, a novel mapping technique of the discrete elements to the underlying LBM grid can be considered as an alternative approach to reduce computational cost.

6.2.3 Propped Fracture Modelling with Random Proppant Distribution

The analyses on fracture permeability and well productivity enhancement in this thesis were demonstrated based on several assumptions, one of which was the uniform distribution of particles in the fractures. However, the proppant distribution can be complex under the influence of the carrying fluids. To obtain a more accurate and reliable prediction, modelling of fractures with randomly distributed proppant or proppant clusters is worthwhile. In addition, multi-layer proppant embedment as shown in Fig. 5.1(b) is another meaningful model for fracture permeability analysis.

Bibliography

[1] D. Wang, C. R. Leonardi, and S. M. Aminossadati. Improved coupling of time integration and hydrodynamic interaction in particle suspensions using the lattice Boltzmann and discrete element methods. *Computers & Mathematics with Applications*, 75(7):2593–2606, 2018.

[2] C. R. Leonardi, W. Regulski, J. W. S. McCullough, D. Wang, T. R. Mitchell, B. D. Jones, and J. R. Williams. Characterising the behaviour of hydraulic fracturing fluids via direct numerical simulation. *Society of Petroleum Engineers*, 2016.

[3] C. R. Leaonardi. Development of a computational framework coupling the non-Newtonian lattice Boltzmann method and the discrete element method with application to block caving. 2009.

[4] C. Pan, L-S. Luo, and C. T. Miller. An evaluation of lattice Boltzmann schemes for porous medium flow simulation. *Computers & Fluids*, 35(8-9):898–909, 2006.

[5] K. D. Pangilinan, C. C. de Leon, and R. C. Advincula. Polymers for proppants used in hydraulic fracturing. *Journal of Petroleum Science and Engineering*, 145:154–160, 2016.

[6] F. Liang, M. Sayed, G. A. Al-Muntasheri, F. F. Chang, and L. Li. A comprehensive review on proppant technologies. *Petroleum*, 2(1):26–39, 2016.

[7] A. Khanna, A. Keshavarz, M. Mobbs, K.and Davis, and P. Bedrikovetsky. Stimulation of the natural fracture system by graded proppant injection. *Journal of Petroleum Science and Engineering*, 111:71–77, 2013.

[8] A. Keshavarz, A. Badalyan, T. Carageorgos, P. Bedrikovetsky, and R. Johnson. Stimulation of coal seam permeability by micro-sized graded proppant placement using selective fluid properties. *Fuel*, 144:228–236, 2015.

[9] M. J. Economides, D. N. Mikhailov, and V. N. Nikolaevskiy. On the problem of fluid leakoff during hydraulic fracturing. *Transport in Porous Media*, 67(3):487–499, Apr 2007.

[10] V. M. Yarushina, D. Bercovici, and M. L. Oristaglio. Rock deformation models and fluid leak-off in hydraulic fracturing. *Geophysical Journal International*, 194(3):1514–1526, 2013.

[11] J. I. Adachi, E. Siebrits, A. Peirce, and J. Desroches. Computer simulation of hydraulic fractures. *International Journal of Rock Mechanics and Mining Sciences*, 44(5):739–757, 2007.

[12] L. Zhou and Z. Hou. A new numerical 3d-model for simulation of hydraulic fracturing in consideration of hydro-mechanical coupling effects. *International Journal of Rock Mechanics and Mining Sciences*, 60:370–380, 2013.

[13] T. K. Perkins and L. R. Kern. Widths of hydraulic fractures. *Society of Petroleum Engineers*, 1961.

[14] R. P. Nordgren. Propagation of a vertical hydraulic fracture. *Society of Petroleum Engineers*, 1972.

[15] A. K. Zheltov. 3. formation of vertical fractures by means of highly viscous liquid. *World Petroleum Congress*, 1955.

[16] J. Geertsma and F. De Klerk. A rapid method of predicting width and extent of hydraulically induced fractures. *Society of Petroleum Engineers*, 1969.

[17] P. E. Clark and J. A. Quadir. Prop transport in hydraulic fractures: A critical review of particle settling velocity equations. *Society of Petroleum Engineers*, 1981.

[18] M. Asadi, S. N. Shah, and D. L. Lord. A rapid method of predicting width and extent of hydraulically induced fractures. *Society of Petroleum Engineers*, 1999.

[19] A. T. Mobbs and P. S. Hammond. Computer simulations of proppant tansport in a hydraulic fracture. *Society of Petroleum Engineers*, 2001.

[20] E. V. Dontsov and A. P. Peirce. Proppant transport in hydraulic fracturing: Crack tip screen-out in KGD and P3D models. *International Journal of Solids and Structures*, 63:206–218, 2015.

[21] R. D. Barree and M. W. Conway. Experimental and numerical modeling of convective proppant transport (includes associated papers 31036 and 31068). *Society of Petroleum Engineers*, 1995.

[22] P. B. Gadde, Y. Liu, J. Norman, R. Bonnecaze, and M. M. Sharma. Modeling proppant settling in water-facs. *Society of Petroleum Engineers*, 2004.

[23] Y. Liu and M. M. Sharma. Effect of fracture width and fluid rheology on proppant settling and retardation: an experimental study. *Society of Petroleum Engineers*, 2005.

[24] M. Khodaverdian and P. McElfresh. Hydraulic fracturing stimulation in poorly consolidated sand: Mechanisms and consequences. *Society of Petroleum Engineers*, 2000.

[25] K. Han, Y. T. Feng, and D. R. J. Owen. Coupled lattice Boltzmann and discrete element modelling of fluid-particle interaction problems. *Computers & Structures*, 85(11-14):1080–1088, 2007.

[26] J. I. Adachi and E. Detournay. Plane strain propagation of a hydraulic fracture in a permeable rock. *Engineering Fracture Mechanics*, 75(16):4666–4694, 2008.

[27] A. P. Bunger, E. Detournay, and D. I. Garagash. Toughness-dominated hydraulic fracture with leak-off. *International Journal of Fracture*, 134(2):175–190, 2005.

[28] J. R. A. Pearson and P. M. J. Tardy. Models for flow of non-Newtonian and complex fluids through porous media. *Journal of Non-Newtonian Fluid Mechanics*, 102(2):447–473, 2002. A Collection of Papers Dedicated to Professor ANDREAS ACRIVOS on the Occasion of his Retirement from the Benjamin Levich Institute for Physiochemical Hydrodynamics and the City College of the CUNY.

[29] Y. Li, J. Guo, and J. Zhao. A new model of fluid leakoff in naturally fractured gas fields and its effects on fracture geometry. *Petroleum Society of Canada*, 2005.

[30] G. C. Howard and C. R Fast. Optimum fluid characteristics for fracture extension. *American Petroleum Institute*, 1957.

[31] B. B. Williams. Fluid loss from hydraulically induced fractures. *Society of Petroleum Engineers*, 1970.

[32] A. Settari and H. S. Price. Simulation of hydraulic fracturing in low-permeability reservoirs. *Society of Petroleum Engineers*, 1984.

[33] A. Settari. New general model of fluid loss in hydraulic fracturing. *Society of Petroleum Engineers*, 1985.

[34] T. Yi and J. M. Peden. A comprehensive model of fluid loss in hydraulic fracturing. *Society of Petroleum Engineers*, 1994.

[35] D. B. Silin and T. W. Patzek. Water injection into a low-permeability rock - 2: Control model. *Transport in Porous Media*, 43(3):557–580, Jun 2001.

[36] B. Carrier and S. Granet. Numerical modeling of hydraulic fracture problem in permeable medium using cohesive zone model. *Engineering Fracture Mechanics*, 79:312–328, 2012.

[37] Y. Fan and M. J. Economides. Fracturing fluid leakoff and net pressure behavior in frac & pack stimulation. *Society of Petroleum Engineers*, 1995.

[38] R. D. Barree and H. Mukherjee. Determination of pressure dependent leakoff and its effect on fracture geometry. *Society of Petroleum Engineers*, 1996.

[39] M. Ramurthy and R. B. Hendrickson. Effects of high pressure dependent leakoff and high process zone stress in coal stimulation treatments. *Society of Petroleum Engineers*, 2007.

[40] J. Hagoort, B. D. Weatherill, and A. Settari. Modeling the propagation of waterflood-induced hydraulic fractures. *Society of Petroleum Engineers*, 1980.

[41] P. J. Van de Hoek. A simple and accurate description of non-linear fluid leak-off in high-permeability fracturing. *Society of Petroleum Engineers*, 2000.

[42] A. Ji, L. Settari and R. B. Sullivan. A novel hydraulic fracturing model fully coupled with geomechanics and reservoir simulation. *Society of Petroleum Engineers*, 2009.

[43] S. A. Mathias and M. van Reeuwijk. Hydraulic fracture propagation with 3-D leak-off. *Transport in Porous Media*, 80(3):499, Apr 2009.

[44] R. H. Dean and J. H. Schmidt. Hydraulic-fracture predictions with a fully coupled geomechanical reservoir simulator. *Society of Petroleum Engineers*, 2009.

[45] M. A. Biot, L. Masse, and W. L. Medlin. A two-dimensional theory of fracture propagation. *Society of Petroleum Engineers*, 1986.

[46] D. N. Mikhailov, M. J. Economides, and V. N. Nikolaevskiy. Fluid leakoff determines hydraulic fracture dimensions: Approximate solution for non-Newtonian fracturing fluid. *International Journal of Engineering Science*, 49(9):809–822, 2011.

[47] E. S. Boek, J. Chin, and P. V. Coveney. Lattice boltzmann simulation of the flow of non-Newtonian fluids in porous media. *International Journal of Modern Physics B*, 17(01n02):99–102, 2003.

[48] J. S. Torok and S.H. Advani. Non-Newtonian fluid flow in a reservoiran application to hydraulic fracturing. *Journal of Energy Resources Technology*, 109(1):6–10, 1987.

[49] G. R. McNamara and G. Zanetti. Use of the boltzmann equation to simulate lattice-gas automata. *Physical Review Letters*, 61(20):2332–2335, Nov 1988.

[50] H. Chen, S. Chen, and W. H. Matthaeus. Recovery of the Navier-Stokes equations using a lattice-gas Boltzmann method. *Physical Review A*, 45(8):R5339–R5342, 1992.

[51] P. Lallemand and L-S. Luo. Theory of the lattice Boltzmann method: Dispersion, dissipation, isotropy, Galilean invariance, and stability. *Physical Review E*, 61(6):6546–6562, 2000.

[52] C. R. Leonardi, D. R. J. Owen, and Y. T. Feng. Numerical rheometry of bulk materials using a power law fluid and the lattice Boltzmann method. *Journal of Non-Newtonian Fluid Mechanics*, 166(12-13):628–638, 2011.

[53] Y. T. Feng, K. Han, and D. R. J. Owen. Combined three-dimensional lattice Boltzmann method and discrete element method for modelling fluid-particle interactions with experimental assessment. *International Journal for Numerical Methods in Engineering*, 81(2):229–245, 2010.

[54] P. A. Cundall and O. D. L. Strack. A discrete numerical model for granular assemblies. *Geotechnique*, 29(1):47–65, 1979.

[55] B. K. Cook, J. R. Williams, D. R. Noble, and D. S. Preece. Direct simulation of particle-laden fluids. In *4th North American Rock Mechanics Symposium*. American Rock Mechanics Association, 2000.

[56] D. R. Noble and J. R. Torczynski. A lattice-Boltzmann method for partially saturated computational cells. *International Journal of Modern Physics C*, 09(08):1189–1201, 1998.

[57] B. K. Cook, D. R. Noble, and J. R. Williams. A direct simulation method for particle-fluid systems. *Engineering Computations*, 21(2/3/4):151–168, 2004.

[58] M. Wang, Y. T. Feng, and C. Y. Wang. Coupled bonded particle and lattice Boltzmann method for modelling fluid-solid interaction. *International Journal for Numerical and Analytical Methods in Geomechanics*, 40(10):1383–1401, 2016.

[59] M. Wang, Y. T. Feng, and C. Y. Wang. Numerical investigation of initiation and propagation of hydraulic fracture using the coupled bonded particle-lattice Boltzmann method. *Computers & Structures*, 181:32–40, 2017.

[60] H. Yu, S. S. Girimaji, and L-S. Luo. Lattice Boltzmann simulations of decaying homogeneous isotropic turbulence. *Physical Review E*, 71(1):016708–, 2005.

[61] J. Smagorinsky. General circulation experiments with the primitive equation I the basic experiment. *Monthly Weather Review*, 91(3):99–164, 1963.

[62] O. E. Strack and B. K. Cook. Three-dimensional immersed boundary conditions for moving solids in the lattice-Boltzmann method. *International Journal for Numerical Methods in Fluids*, 55(2):103–125, 2007.

[63] B. Sheikh and A. Pak. Numerical investigation of the effects of porosity and tortuosity on soil permeability using coupled three-dimensional discrete-element method and lattice Boltzmann method. *Physical Review E*, 91(5):053301–, 2015.

[64] M. Wang, Y. T. Feng, G. N. Pande, A. H. C. Chan, and W. X. Zuo. Numerical modelling of fluid-induced soil erosion in granular filters using a coupled bonded particle lattice Boltzmann method. *Computers and Geotechnics*, 82:134–143, 2017.

[65] M. Wang, Y. T. Feng, G. N. Pande, and T. T. Zhao. A coupled 3-dimensional bonded discrete element and lattice Boltzmann method for fluid-solid coupling in cohesive geomaterials. *International Journal of Numerical and Analytical Methods in Geomechanics*, 42(12):1405–1424, May 2018.

[66] E. Aharonov and D. H. Rothman. Non-Newtonian flow (through porous media): A lattice Boltzmann method. *Geophysical Research Letters*, 20(8):679–682, 1993.

[67] N. Rakotomalala, D. Salin, and P. Watzky. Simulations of viscous flows of complex fluids with a Bhatnagar, Gross, and Krook lattice gas. *Physics of Fluids*, 8(11):3200–3202, 1996.

[68] J. Boyd, J. Buick, and S. Green. A second-order accurate lattice Boltzmann non-Newtonian flow model. *Journal of Physics A: Mathematical and General*, 39(46):14241, 2006.

[69] A. Nejat, V. Abdollahi, and K. Vahidkhah. Lattice Boltzmann simulation of non-Newtonian flows past confined cylinders. *Journal of Non-Newtonian Fluid Mechanics*, 166(12):689–697, 2011.

[70] Y. Shi and G. H. Tang. Simulation of Newtonian and non-Newtonian rheology behavior of viscous fingering in channels by the lattice Boltzmann method. *Computers & Mathematics with Applications*, 68(10):1279–1291, 2014.

[71] S. P. Sullivan, L. F. Gladden, and M. L. Johns. Simulation of power-law fluid flow through porous media using lattice Boltzmann techniques. *Journal of Non-Newtonian Fluid Mechanics*, 133(2-3):91–98, 2006.

[72] J. G. Oldroyd. An approach to non-Newtonian fluid mechanics. *Journal of Non-Newtonian Fluid Mechanics*, 14:9–46, 1984.

[73] I. Ginzburg. A free-surface lattice Boltzmann method for modelling the filling of expanding cavities by Bingham fluids. *Philosophical Transactions of the Royal Society of London A: Mathematical, Physical and Engineering Sciences*, 360(1792):453–466, 2002.

[74] A. Vikhansky. Lattice- Boltzmann method for yield-stress liquids. *Journal of Non-Newtonian Fluid Mechanics*, 155(3):95–100, 2008.

[75] C-H. Wang and J-R Ho. Lattice Boltzmann modeling of Bingham plastics. *Physica A: Statistical Mechanics and its Applications*, 387(19):4740–4748, 2008.

[76] G. H. Tang, S. B. Wang, P. X. Ye, and W. Q. Tao. Bingham fluid simulation with the incompressible lattice Boltzmann model. *Journal of Non-Newtonian Fluid Mechanics*, 166(1):145–151, 2011.

[77] J. Hardy, Y. Pomeau, and O. de Pazzis. Time evolution of a two-dimensional model system. I. Invariant states and time correlation functions. *Journal of Mathematical Physics*, 14(12):1746–1759, Dec 1973.

[78] J. Hardy, O. de Pazzis, and Y. Pomeau. Molecular dynamics of a classical lattice gas: Transport properties and time correlation functions. *Phys. Rev. A*, 13(5):1949–1961, May 1976.

[79] U. Frisch, B. Hasslacher, and Y. Pomeau. Lattice-gas automata for the Navier-Stokes equation. *Physical Review Letters*, 56(14):1505–1508, Apr 1986.

[80] S. Chen and G. D. Doolen. Lattice Boltzmann method for fluid flows. *Annual Review of Fluid Mechanics*, 30(1):329–364, Jan 1998.

[81] Francesca Nannelli and Sauro Succi. The lattice Boltzmann equation on irregular lattices. *Journal of Statistical Physics*, 68(3):401–407, 1992.

[82] X. He, L-S. Luo, and M. Dembo. Some progress in lattice Boltzmann method. Part I. Nonuniform mesh grids. *Journal of Computational Physics*, 129(2):357–363, 1996.

[83] Xiaoyi He and Gary Doolen. Lattice Boltzmann method on curvilinear coordinates system: Flow around a circular cylinder. *Journal of Computational Physics*, 134(2):306–315, 1997.

[84] R.G.M. Van der Sman and M.H. Ernst. Convection-diffusion lattice Boltzmann scheme for irregular lattices. *Journal of Computational Physics*, 160(2):766–782, 2000.

[85] I. V. Karlin, S. Succi, and S. Orszag. Lattice Boltzmann method for irregular grids. *Physical Review Letters*, 82:5245–5248, Jun 1999.

[86] P. A. Skordos. Initial and boundary conditions for the lattice Boltzmann method. *Physical Review E*, 48(6):4823–4842, Dec 1993.

[87] P. L. Bhatnagar, E. P. Gross, and M. Krook. A model for collision processes in gases. I. Small amplitude processes in charged and neutral one-component systems. *Physical Review*, 94(3):511–525, 1954.

[88] B. Chun and A. J. C. Ladd. Interpolated boundary condition for lattice Boltzmann simulations of flows in narrow gaps. *Physical Review E*, 75(6):066705–, 2007.

[89] C. Rettinger and U. Rude. A comparative study of fluid-particle coupling methods for fully resolved lattice Boltzmann simulations. *Computers & Fluids*, 154:74–89, 2017.

[90] D. d'Humieres. Multiple-relaxation-time lattice Boltzmann models in three dimensions. *Philosophical Transactions of the Royal Society of London. Series A: Mathematical, Physical and Engineering Sciences*, 360(1792):437–451, 2002.

[91] I. Ginzburg, F. Verhaeghe, and D. d'Humieres. Two-relaxation-time lattice Boltzmann scheme: About parametrization, velocity, pressure and mixed boundary conditions. *Communications in Computational Physics*, 3(2):427–478, 2008.

[92] Z. Guo and C. Shu. *Lattice Boltzmann Method and Its Applications in Engineering*, volume Volume 3. World Scientific, Mar 2013.

[93] L. H. Holway. New statistical models for kinetic theory: Methods of construction. *The Physics of Fluids*, 9(9):1658–1673, Sep 1966.

[94] D. d'Humieres and I. Ginzburg. Viscosity independent numerical errors for lattice Boltzmann models: From recurrence equations to "magic" collision numbers. *Computers & Mathematics with Applications*, 58(5):823–840, 2009.

[95] S. Khirevich, I. Ginzburg, and U. Tallarek. Coarse- and fine-grid numerical behavior of MRT/TRT lattice-Boltzmann schemes in regular and random sphere packings. *Journal of Computational Physics*, 281:708–742, 2015.

[96] J. M. Buick and C. A. Greated. Gravity in a lattice Boltzmann model. *Physical Review E*, 61(5):5307–5320, May 2000.

[97] D. O. Martinez, W. H. Matthaeus, S. Chen, and D. C. Montgomery. Comparison of spectral method and lattice Boltzmann simulations of two-dimensional hydrodynamics. *Physics of Fluids*, 6(3):1285–1298, Mar 1994.

[98] Y. H. Qian, D. d'Humieres, and P. Lallemand. Lattice BGK models for Navier-Stokes equation. *EPL (Europhysics Letters)*, 17(6):479, 1992.

[99] T. R. Mitchell and C. R. Leonardi. Micromechanical investigation of fines liberation and transport during coal seam dewatering. *Journal of Natural Gas Science and Engineering*, 35:1101–1120, 2016.

[100] C. R. Leonardi, J. W. S. McCullough, B. D. Jones, and J. R. Williams. Electromagnetic excitation of particle suspensions in hydraulic fractures using a coupled lattice Boltzmann-discrete element model. *Computational Particle Mechanics*, 3(2):125–140, Apr 2016.

[101] R. Courant, K. Friedrichs, and H. Lewy. On the partial difference equations of mathematical physics. *IBM Journal of Research and Development*, 11(2):215–234, 1967.

[102] K. Han, D. Peric, A. J. L. Crook, and D. R. J. Owen. A combined finite/discrete element simulation of shot peening processes - Part I: studies on 2D interaction laws. *Engineering Computations*, 17(5):593–620, 2000.

[103] K. Han, D. Peric, A. J. L. Crook, and D. R. J. Owen. A combined finite/discrete element simulation of shot peening processes - Part II: 3D interaction laws. *Engineering Computations*, 17(6):680–702, 2000.

[104] I. Ginzbourg and P. M. Adler. Boundary flow condition analysis for the three-dimensional lattice Boltzmann model. *Journal of Physics II France*, 4(2):191–214, 1994.

[105] A. J. C. Ladd. Numerical simulations of particulate suspensions via a discretized Boltzmann equation. Part 2. Numerical results. *Journal of Fluid Mechanics*, 271:311–339, 1994.

[106] A. J. C. Ladd and R. Verberg. Lattice-Boltzmann simulations of particle-fluid suspensions. *Journal of Statistical Physics*, 104(5):1191–1251, 2001.

[107] Y. T. Feng, K. Han, and D. R. J. Owen. Coupled lattice Boltzmann method and discrete element modelling of particle transport in turbulent fluid flows: Computational issues. *International Journal for Numerical Methods in Engineering*, 72(9):1111–1134, 2007.

[108] M. Bouzidi, M. Firdaouss, and P. Lallemand. Momentum transfer of a Boltzmann-lattice fluid with boundaries. *Physics of Fluids*, 13(11):3452–3459, 2001.

[109] I. Ginzburg and D. d'Humieres. Multireflection boundary conditions for lattice Boltzmann models. *Physical Review E*, 68(6):066614–, 2003.

[110] Y. Peng and L-S. Luo. A comparative study of immersed-boundary and interpolated bounce-back methods in LBE. *Progress in Computational Fluid Dynamics, an International Journal*, 8(1-4):156–167, 2008.

[111] A. J. C. Ladd. Numerical simulations of particulate suspensions via a discretized Boltzmann equation. Part 1. Theoretical foundation. *Journal of Fluid Mechanics*, 271:285–309, 1994.

[112] D. J. Holdych. Lattice Boltzmann methods for diffuse and mobile interfaces. 2003.

[113] C. R. Leonardi, B. D. Jones, D. W. Holmes, and J. R. Williams. Simulation of complex particle suspensions using coupled lattice boltzmann-discrete element methods. In Graham Mustoe, editor, *DEM6: 6th Internatioal Conference on Discrete Element Methods*, Proceedings of the 6th International Conference on Discrete Element Methods, pages 1–8. Colorado School of Mines, 2013.

[114] Q. Zou and X. He. On pressure and velocity boundary conditions for the lattice Boltzmann BGK model. *Physics of Fluids*, 9(6):1591–1598, 1997.

[115] D. R. J. Owen, C. R. Leonardi, and Y. T. Feng. An efficient framework for fluid-structure interaction using the lattice Boltzmann method and immersed moving boundaries. *International Journal for Numerical Methods in Engineering*, 87(1-5):66–95, 2011.

[116] P. Prestininzi, A. Montessori, M. La Rocca, and S. Succi. Reassessing the single relaxation time lattice Boltzmann method for the simulation of Darcy's flows. *International Journal of Modern Physics C*, 27(04):1650037, 2016.

[117] X. He, Q. Zou, L-S. Luo, and M. Dembo. Analytic solutions of simple flows and analysis of nonslip boundary conditions for the lattice Boltzmann BGK model. *Journal of Statistical Physics*, 87(1):115–136, 1997.

[118] A. A. Zick and G. M. Homsy. Stokes flow through periodic arrays of spheres. *Journal of Fluid Mechanics*, 115:13–26, 1982.

[119] R. S. Maier, R. S. Bernard, and D. W. Grunau. Boundary conditions for the lattice Boltzmann method. *Physics of Fluids*, 8(7):1788–1801, 1996.

[120] M. B. Reider and J. D. Sterling. Accuracy of discrete-velocity BGK models for the simulation of the incompressible Navier-Stokes equations. *Computers & Fluids*, 24(4):459–467, 1995.

[121] Z-G. Feng and E. E. Michaelides. Hydrodynamic force on spheres in cylindrical and prismatic enclosures. *International Journal of Multiphase Flow*, 28(3):479–496, 2002.

[122] M. K. Lyon and L. G. Leal. An experimental study of the motion of concentrated suspensions in two-dimensional channel flow. part 2. bidisperse systems. *Journal of F;uid mechanics*, 363:57–77, 1998.

[123] A. Singh and P. R. Nott. Experimental measurements of the normal stresses in sheared Stokesian suspensions. *Journal of Fluid Mechanics*, 490:293–320, 2003.

[124] B. Lecampion and D. I. Garagash. Confined flow of suspensions modelled by a frictional rheology. *Journal of Fluid Mechanics*, 759:197–235, October 2014.

[125] C. Cassar, M. Nicolas, and O. Pouliquen. Submarine granular flows down inclined planes. *Physics of Fluids*, 17(10):103301, 2005.

[126] R. J. Phillips, R. C. Armstrong, R. A. Brown, A. L. Graham, and J. R. Abbott. A constitutive equation for concentrated suspensions that accounts for shear-induced particle migration. *Physics of Fluids A: Fluid Dynamics*, 4(1):30–40, Jan 1992.

[127] J. F. Morris and F. Boulay. Curvilinear flows of noncolloidal suspensions: The role of normal stresses. *Journal of Rheology*, 43(5):1213, 1999.

[128] F. Boyer, E. Guazzelli, and O. Pouliquen. Unifying suspension and granular rheology. *Physical Review Letters*, 107(18):188301–, Oct 2011.

[129] J. Brady and G. Bossis. Stokesian dynamics. *Annual Review of Fluid Mechanics*, 20(1):111–157, 1988.

[130] A. Sierou and J. F. Brady. Accelerated Stokesian dynamics simulations. *Journal of Fluid Mechanics*, 448:115–146, Nov 2001.

[131] A. Sierou and J. F. Brady. Rheology and microstructure in concentrated noncolloidal suspensions. *Journal of Rheology*, 46(5):1031–1056, Aug 2002.

[132] J. W. Swan and J. F. Brady. Particle motion between parallel walls: Hydrodynamics and simulation. *Physics of Fluids*, 22(10):103301, 2010.

[133] J. W. Swan and J. F. Brady. The hydrodynamics of confined dispersions. *Journal of Fluid Mechanics*, 687:254–299, 2011.

[134] A. Kumar and J. J. L. Higton. Particle mesh Ewald Stokesian dynamics simulations for suspensions of non-spherical particles. *Journal of Fluid Mechanics*, 675:297–335, 2011.

[135] X. Bian, S. Litvinov, M. Ellero, and N. J. Wagner. Hydrodynamic shear thickening of particulate suspension under confinement. *Journal of Non-Newtonian Fluid Mechanics*, 213:39–49, Nov 2014.

[136] X. Bian and M. Ellero. A splitting integration scheme for the SPH simulation of concentrated particle suspensions. *Computer Physics Communications*, 185(1):53–62, 2014.

[137] T. Iwashita and R. Yamamoto. Direct numerical simulations for non-Newtonian rheology of concentrated particle dispersions. *Physical Review E*, 80(6):061402–, Dec 2009.

[138] A. Vazquez-Quesada, X. Bian, and M. Ellero. Three-dimensional simulations of dilute and concentrated suspensions using smoothed particle hydrodynamics. *Computational Particle Mechanics*, 3(2):167–178, 2016.

[139] A. Vazquez-Quesada and M. Ellero. Rheology and microstructure of non-colloidal suspensions under shear studied with smoothed particle hydrodynamics. *Journal of Non-Newtonian Fluid Mechanics*, 233:37–47, 2016. Papers presented at the Rheology Symposium in honor of Prof. R. I. Tanner on the occasion of his 82nd birthday, in Vathi, Samos, Greece.

[140] A. Vazquez-Quesada, R. I. Tanner, and M. Ellero. *Shear Thinning of Noncolloidal Suspensions*, volume 117. August 2016.

[141] A. Vazquez-Quesada and M. Ellero. SPH modeling and simulation of spherical particles interacting in a viscoelastic matrix. *Physics of Fluids*, 29(12):121609–, Nov 2017.

[142] T. J. R. Hughes, W. K. Liu, and T. K. Zimmermann. Lagrangian-Eulerian finite element formulation for incompressible viscous flows. *Computer Methods in Applied Mechanics and Engineering*, 29(3):329–349, 1981.

[143] H. H. Hu, N. A. Patankar, and M. Y. Zhu. Direct numerical simulations of fluid-solid systems using the arbitrary Lagrangian-Eulerian technique. *Journal of Computational Physics*, 169(2):427–462, 2001.

[144] K. Thogersen and M. Dabrowski. Mixing of the fluid phase in slowly sheared particle suspensions of cylinders. *Journal of Fluid Mechanics*, 818:807–837, 2017.

[145] J. Walter, A.-V. Salsac, D. Barthes-Biesel, and P. Le Tallec. Coupling of finite element and boundary integral methods for a capsule in a Stokes flow. *International Journal for Numerical Methods in Engineering*, 83(7):829–850, 2010.

[146] D. Matsunaga, Y. Imai, T. Yamaguchi, and T. Ishikawa. Rheology of a dense suspension of spherical capsules under simple shear flow. *Journal of Fluid Mechanics*, 786:110–127, 2016.

[147] A. Z. Zinchenko and R. H. Davis. A multipole-accelerated algorithm for close interaction of slightly deformable drops. *Journal of Computational Physics*, 207(2):695 – 735, 2005.

[148] X. Chateau, G. Ovarlez, and K. L. Trung. Homogenization approach to the behavior of suspensions of noncolloidal particles in yield stress fluids. *Journal of Rheology*, 52(2):489–506, Mar 2008.

[149] R. Avazmohammadi and P. P. Castaneda. Macroscopic rheological behavior of suspensions of soft solid particles in yield stress fluids. *Journal of Non-Newtonian Fluid Mechanics*, 234(Supplement C):139–161, 2016.

[150] H. Haddadi and J.F. Morris. Microstructure and rheology of finite inertia neutrally buoyant suspensions. *Journal of Fluid Mechanics*, 749:431–459, 2014.

[151] W-P. Breugem. A second-order accurate immersed boundary method for fully resolved simulations of particle-laden flows. *Journal of Computational Physics*, 231(13):4469–4498, 2012.

[152] Q. Zhou and L-S. Fan. A second-order accurate immersed boundary-lattice Boltzmann method for particle-laden flows. *Journal of Computational Physics*, 268:269–301, 2014.

[153] J. R. Clausen and C. K. Aidun. Galilean invariance in the lattice-Boltzmann method and its effect on the calculation of rheological properties in suspensions. *International Journal of Multiphase Flow*, 35(4):307–311, 2009.

[154] B. Wen, C. Zhang, Y. Tu, C. Wang, and H. Fang. Galilean invariant fluid-solid interfacial dynamics in lattice Boltzmann simulations. *Journal of Computational Physics*, 266:161–170, 2014.

[155] C. Peng, Y. Teng, B. Hwang, Z. Guo, and L. Wang. Implementation issues and benchmarking of lattice Boltzmann method for moving rigid particle simulations in a viscous flow. *Computers & Mathematics with Applications*, 72(2):349–374, 2016.

[156] T. Shi, J. Hu, and Z. Guo. An investigation on momentum exchange methods and refilling algorithms for lattice Boltzmann simulation of particulate flows. *Computers & Fluids*, 133:1–14, 2016.

[157] D. H. Johnson, F. Vahedifard, B. Jelinek, and J. F. Peters. Micromechanical modeling of discontinuous shear thickening in granular media-fluid suspension. *Journal of Rheology*, 61(2):265–277, 2017.

[158] L. L. Lacy, A. R. Rickards, and D. M. Bilden. Fracture width and embedment testing in soft reservoir sandstone. 1998.

[159] A. Keshavarz, Y. Yang, A. Badalyan, R. Johnson, and P. Bedrikovetsky. Laboratory-based mathematical modelling of graded proppant injection in CBM reservoirs. *International Journal of Coal Geology*, 136:1–16, 2014.

[160] S. R. Darin and J. L. Huitt. Effect of a partial monolayer of propping agent on fracture flow capacity, 1960.

[161] L. J. Volk, C. J. Raible, H. B. Carroll, and J. S. Spears. Embedment of high strength proppant into low-permeability reservoir rock, 1981.

[162] B. Alramahi and M.I. Sundberg. Proppant embedment and conductivity of hydraulic fractures in shales, 2012.

[163] K. Li, Y. Gao, Y. Lyu, and M. Wang. New mathematical models for calculating proppant embedment and fracture conductivity. *Society of Petroleum Engineers*, 2015.

[164] T. Hou, S. Zhang, X. Ma, J. Shao, Y. He, X. Lv, and J. Han. Experimental and theoretical study of fracture conductivity with heterogeneous proppant placement. *Journal of Natural Gas Science and Engineering*, 37:449–461, 2017.

[165] J. Zhang, L. Ouyang, D. Zhu, and A. D. Hill. Experimental and numerical studies of reduced fracture conductivity due to proppant embedment in the shale reservoir. *Journal of Petroleum Science and Engineering*, 130:37–45, 2015.

[166] F. Zhang, H. Zhu, H. Zhou, J. Guo, and B. Huang. Discrete-element-method/computational-fluid-dynamics coupling simulation of proppant embedment and fracture conductivity after hydraulic fracturing. *Society of Petroleum Engineers*, 2017.

[167] X. Zheng, M. Chen, B. Hou, Z. Ye, W. Wang, C. Yin, and X. Chen. Effect of proppant distribution pattern on fracture conductivity and permeability in channel fracturing. *Journal of Petroleum Science and Engineering*, 149:98–106, 2017.

[168] D. Chen, Z. Ye, Z. Pan, Y. Zhou, and J. Zhang. A permeability model for the hydraulic fracture filled with proppant packs under combined effect of compaction and embedment. *Journal of Petroleum Science and Engineering*, 149:428–435, 2017.

[169] M. Mueller and M. Amro. Indentaion hardness for improved proppant embedment prediction in shale formations, 2015.

[170] J. Zhang. Theoretical conductivity analysis of surface modification agent treated proppant. *Fuel*, 134:166–170, 2014.

[171] J. Zhang and J. Hou. Theoretical conductivity analysis of surface modification agent treated proppant II - channel fracturing application. *Fuel*, 165:28–32, 2016.

[172] Y. Tang, P. G. Ranjinth, M. S. A. Perera, and T. D. Rathanaweera. Influences of proppant concentration and fracturing fluids on proppant-embedment behavior for inhomogeneous rock medium: An experimental and numerical study. *Society of Petroleum Engineers*, 2018.

[173] S. A. Fraser and R. L. Jr. Johnson. Impact of laboratory testing variability in fracture conductivity for stimulation effectiveness in permian deep coal source rocks, Cooper Basin, South Australia. *Society of Petroleum Engineers*, SPE Asia Pacific Oil and Gas Conference and Exhibition, 2018.

[174] A. Khanna, A. Kotousov, J. Sobey, and P. Weller. Conductivity of narrow fractures filled with a proppant monolayer. *Journal of Petroleum Science and Engineering*, 100:9–13, 2012.

[175] A. C. Fischer-Cripps. *Introduction to Contact Mechanics, Second Edition*. Springer US, 2007.

[176] A. Vikhansky. Construction of lattice-Boltzmann schemes for non-Newtonian and two-phase flows. *The Canadian Journal of Chemical Engineering*, 90(5):1081–1091, 2012.